Packaging and Characterization of NbN Superconducting Nanowire Single Photon Detectors

by

Jean-Luc FX. Orgiazzi

A thesis
presented to the University of Waterloo
in fulfillment of the
thesis requirement for the degree of
Master of Applied Science
in
Electrical and Computer Engineering

Waterloo, Ontario, Canada, 2009

AUTHOR'S DECLARATION

I hereby declare that I am the sole author of this thesis. This is a true copy of the thesis, including any required final revisions, as accepted by my examiners.

I understand that my thesis may be made electronically available to the public.

Jean-Luc Orgiazzi

Abstract

Superconducting nanowire single-photon detectors (SNSPDs) are nanodevices usually made from thin niobium nitride (NbN) films. Operated at liquid helium temperature, they can exhibit high detection efficiency with low dark-counts associated with a fast response time and a low timing jitter. Covering a broad detection range from ultraviolet to mid-infrared, SNSPDs are a very attractive alternative to silicon or gallium arsenide based semiconductor detectors for fiber based telecommunication when single-photon sensitivity and high counting rates are necessary.

Efficient packaging and fiber coupling of a SNSPD is in itself a real challenge and is often a limiting factor in reaching high system quantum efficiency. Our approach makes use of a controlled expansion alloy which has been adequately heat treated to enhance its characteristics for cryogenic operation. This insures the integrity of the optical coupling at cryogenic temperatures while done at room temperature. It also provides a good attenuation for electromagnetic interference due to the high relative permeability of the nickel-iron alloy. The small form factor of this pigtailed optical fiber package makes it versatile and could be easily integrated with a commercial cryogen-free system or simply dipped into a standard helium transport Dewar. We report on our theoretical and experimental methodology to evaluate the optical coupling quality and present the optoelectronic characterization of two devices packaged in this way. Electrical simulation is studied to understand the speed limitation factor inherent to these devices and preliminary speed and jitter measurements are reported.

Acknowledgements

First and foremost I would like to express my sincere gratitude to my supervisor Professor A. Hamed Majedi for offering me the chance to work on this project, his support and patience throughout this research.

I have been very lucky to be part of IQOL and IQC with their remarkable members and for the good working environment. It is through the interactions with my colleagues that I have learned the most.

I would like to thank among many who have contributed and helped in this work in some ways, Professor Gregor Weihs and Christophe Couteau for the use of their optomechanical equipments, Professor Raafat Mansour and Bill Jolley, director and lab manager respectively of the Center for Integrated RF Engineering for letting me gold plate my packages prototypes, Kwai Chan and John Potzold from the engineering machine shop for their great advices.

I would also like to thank my readers, Professor Hany Aziz and Professor Simarjeet Saini for taking the time to review this report and their evaluation.

I would like to thank the financial supports for my research project and living stipend from the Ontario Center of Excellence (OCE), the Canadian Institute for Photonic Innovations (CIPI-Student), the Quantum Information Network Canada (QuamtumWorks), the Institute for Quantum Computing (IQC) and its sponsors, the University of Waterloo, my parents and the taxpayers of Canada of course. Thank you.

Table of Contents

List of Figures

List of Tables

Chapter 1
Introduction

1.1 On the needs for superconducting single-photon detectors

There exist various technologies to detect single quanta of electromagnetic energy. Those detectors absorb the incoming photon and through various direct or indirect detection mechanisms eventually fire a counting electrical pulse. Some of the single-photon detectors available are: photomultiplier tubes (PMT), semiconductor avalanche photo-diodes (APD), superconductor tunnel-junction detectors (STJ), transition-edge sensors (TES), superconducting kinetic inductance detectors (KID), superconducting traveling waveguide detectors (STWD) and superconducting nanowire single photon detector (SNSPD), the subject of this work.

SNSPDs have been used for the characterization of single photon source [1] [2] [3], quantum dots [4], and non-invasive VLSI chip testing [5] [6] [7]. This family of nano-sensors represents a potential candidate for application in fiber based Quantum Key Distribution (QKD) [8] [9] [10] [11] [12] [13] [14] and ultra high speed communication [15] due to their high speed performance, low dark-count rate and low timing jitter compared to other families of devices listed above. Even if their sensitivity can be pushed to the single photon level they still possess a high dynamic range [16] [17] and these devices seem to show the greatest potential for large scale integration and detection efficiency.

We present in this section an overview of the defining parameters of single photon detectors of various families .The following properties are the most commonly used to describe and compare the various technologies of photodetectors and are the most relevant in the field of quantum information system and optical communication in general. These are quantum efficiency (QE), dark-count, timing jitter, maximum count rate (speed), photon number resolving and photon energy resolving capabilities.

Quantum efficiency (QE) is defined as the probability that a single photon incident on the device will generate excess photocarriers that contributes to the detector current [18]. The quantum efficiency can be intrinsic to the device or external (system). The system quantum efficiency will be highly dependent on the loss of the channel and the coupling factor of the light in the device active area. Knowing that single mode optical fibers used in optical communication networks show a minimum attenuation at a wavelength of around 1.55μm it would be highly desirable to have a high QE and fast detector performing in that range. However, in this near infrared range, the energy of the

photons is below 1eV and detectors with the appropriate energy bandgap to detect those wavelengths suffers from the thermal noise if operated at room temperature meaning high dark-count as can be seen in the table 1 for even the best avalanche photodiodes. [19]

Dark-count probability is defined as the probability that a count event is registered while no photon from the source to be measured is incident on the detector's active area. The occurrence of these false counts can greatly affect the efficiency and reliability of the communication system. It can be noted already that superconducting single photon detectors have a net advantage on their semiconductor counterparts on this matter due to their usual operating temperature ranging from 0.1 to 4 Kelvin. Indeed, the random thermal activation of carriers is greatly reduced at those temperatures. However, due to their large spectral bandwidth and high sensitivity, superconducting detectors' dark-counts can also be triggered by high energy particles and background radiations and therefore require appropriate shielding.

Timing jitter (called time resolution in Table 1) defines how accurately one knows the arrival time of the photon and this parameter takes all its importance in photons coincidence measurements usually encountered in quantum optics experiments. Typically, NbN Nanowire superconducting single photon detectors can have a timing jitter as low as 18 ps.

Maximum count rate: assuming that the surrounding readout electronic and other computer systems do not represent a bottleneck and can handle the incoming pulse rate, the maximum counting rate is usually estimated as the inverse of the deadtime which is defined as the time during which the detection mechanism is inhibited just after the detection of one photon. Indeed, due to the device geometry, detection mechanism and readout electronic, two detection events cannot occur instantaneously one after the other as the device needs to recover to a state where it is ready to detect the next quanta of electromagnetic energy.

Photon number resolving capabilities: most commercially available APDs and photomultiplier tubes cannot distinguish between a single photon event and a more than one photon event. However, some research groups have designed specific detectors and electronics to achieve that purpose [20] [21]. In the field of NbN SNSPD, the photon resolving capabilities are currently under investigation and from a theoretical point of view, nothing prevents this behavior

Photon energy resolving capabilities: this information can usually be extracted from the recorded flow of data after a statistical analysis has been performed. The photon counting means is compared

to the known calibrated wavelength response of a particular sensor. Photon energy resolving capability would be especially interesting in the field of astronomy where the study of the incoming light coming from distant stars gives a lot of information on their chemical composition. In the field of quantum communication or quantum cryptography, such capability would enable the encoding of the information, not only on the polarization state of the photon for example but also on its wavelength.

The superconducting family has different candidates that possess one or more of the desired characteristics. Superconducting tunnel junctions (STJ), are detectors where the generated quasiparticles are drained by the electric field of the junction, collected and amplified. This structure permits photon number resolving [22] and recent developments by the European Space Agency led to the integration of an array of 120 STJ's. [23] [24] [25]. Resonant circuit detectors are devices where the quasiparticles generated by the photon absorption modify the transient damping of a high Q resonator attached to the detection active area. The quality factor of the resonator is momentarily modified and this variation can be the base of the detection mechanism. This approach is very well suited for large scale integration due to the relatively practical readout approach and good pixel filling factor [26].The other class of superconducting photon detectors are based on bolometric detection of single photon. This detection mechanism is based on the change in resistance of the device when a small amount of energy is absorbed in the superconducting active layer. There exist two main sub families of devices, one of which, the NbN SNSP belongs to:

-Transition edge sensors (TES) based on Tungsten filament possess the best photon number resolving capabilities for near infra red photons, but requires extremely low operational temperature (around 0.1K) and are very slow to recover and ready to accept another incoming photon pulse [27].

-Hot electron bolometers (HEB) are based on a photon induced imbalance of the thermal equilibrium in a superconducting micro-bridge or meander line. A photon absorbed in a very thin film of superconducting material locally heats the material that loses its superconducting properties thus creating a voltage pulse if under a current bias and then recover to its original state. Chapter 2 describes this phenomenon in more details.

From Table 1, we see that NbN SNSPDs are well suited when high speed, low jitter and especially low dark-counts are the most important. They have also shown to have their best figures of merit for detecting single visible optical photons [28] [29]. The quantum efficiency of SNSPD which might seem low compared to TES for example will depend on the filling factor of the meander structure, the

photo-absorption coefficient on the thin film of NbN and the electrical signal to noise ratio of those detectors. [30] [31].

Table 1 Comparison of semiconducting and superconducting SPDs [32] (SSPD: superconducting single photon detector, TES: transition edge sensor, STJ: superconducting tunneling junction)

	Semiconducting APDs		Superconducting SPDs		
Detectors	Si [33]	InGaAs [34]	SSPD [30] [35]	TES [36] [37]	STJ [22] [38]
Temperature (K)	300	200	2-4.2	0.1	0.4
Wavelength (μm)	0.4-1.1	0.9-1.7	0.4-5.6	0.1-5	0.2-1
Time resolution	300 ps	300 ps	18 ps	300 ns	< 2ns
Quantum Efficiency	70% @ 630 nm	25% @ 1.55μm	10% @ 1.55 μm	92% @ 1.55 μm	50% @ 500 nm
Dark-count rate (Hz)	< 25	$< 10^4$	<0.01	<0.001	N/A
Maximum count rate	10 MHz	1 MHz	250 MHz	20 kHz	50 kHz
Photon number resolution	Very limited	No	Study in progress	Yes	Yes

1.2 Objectives

Indeed, superconducting single photon detectors have recently been demonstrated to have intrinsic quantum efficiencies (QE) as high as 57 % [39] at near-infrared wavelengths for niobium nitride (NbN) nanowire based devices and 95 % [40] for photon counting transition-edge sensors (TESs). These recent advancements in the optimization of the quantum efficiencies of these detectors has been made possible by the design of appropriate optical cavities to increase the interactions of the single photon pulses with the active area and the design of precise anti-reflection coating for the desired wavelength of operation [39] . While the yield of good devices might still be low, improvements in the thin film quality [41], patterning techniques [42], size or type of wafer used [43] will lead towards the fabrication of devices with quantum efficiencies reaching their theoretical limit in the coming years and at a lower cost.

However, efficient coupling of light to the small active areas of those devices operating in a cryogenic environment is a real challenge and limits the overall potential of those detectors in a practical setup like the implementation of a quantum key distribution (QKD) system [44] over distances larger than 200 km. Measured system quantum efficiencies (SQE) of 0.33 % and coupling efficiencies of about 30 % have been reported [45] and the implementations of optical fiber coupling using cryogenic epoxy have a good potential [46] but can be sensitive to thermal cycles and material stress. The optical coupling between the device active area and the optical fiber must be optimized in

order to use the full potential of those detectors. This coupling must be resilient to vibrations, high vacuum, high temperature gradients, easy to reproduce and stable over time. The good performance of superconducting nanowire single photon detectors (SNSPD) in harsh environments would permit their usage in satellites and inter-celestial communication links in the future.

The main objective of this work is to propose an approach that makes use of a controlled expansion alloy and other readily available components for the realization of the robust packaging and optical coupling of SNSPD detectors to address the issues presented with current setups and reach the goals mentioned above. We also verify through theoretical modeling some of the attributes of the device which can be used to design better performing detectors in the future.

Emphasis is put on providing an efficient and reliable test setup to characterize present and future superconducting optoelectronic nano-devices.

1.3 Organization of this thesis

Chapter 2 presents the detection mechanism associated with thin superconducting film single photon detectors and the geometry of the device. A review of the commonly used fabrication steps reported by other groups to make the detectors used in this project is then presented. An electrical model is derived in order to simulate the single photon detection and its associated voltage pulse. Chapter 3 describes the technicalities related to the fabrication and the details of the assembly of an individual device. The various steps of the design methodology take into considerations the objectives of low cost, adaptability to manufacturing and ease of use for the user. An optical coupling model between a single mode fiber and the device active area is introduced. The possible misalignment due to material contraction at low temperature is taken into account. We then present the optical alignment procedure and experimental setup using a custom made and low profile dipper probe configuration in a liquid helium Dewar. Device operation at low temperature is confirmed with some initial cool down at a stable temperature and with some I-V measurements. Finally, chapter 4 reports on the experimental results using two devices packaged in this way. We investigate some initial issues with the optical setup and propose a solution which led to the proper characterization of the devices. Optoelectronic characterization is performed at two telecommunication wavelengths. We report on some initial speed and jitter tests before conclusion.

Chapter 2
Detection mechanism, fabrication and modeling

2.1 Detection mechanism

2.1.1 Superconductivity: a brief reminder

Superconductors are often defined as elements, inter-metallic alloys, or compounds that conduct electricity without resistance below a certain temperature. Once set in motion, electrical current will flow forever in a closed loop of superconducting material, making it the closest thing to perpetual motion in nature. Scientists refer to superconductivity as a macroscopic quantum phenomenon. The effective zero resistivity is also associated with the exclusion of the interior magnetic field, an effect called the Meissner effect (also called Meissner-Ochsenfeld).

Under a particular temperature called critical temperature or T_c, a superconducting material will transit from its normal state to the superconducting state. This transition is usually abrupt. The value of T_c and the transition width can vary for the same material as a function of crystal structure, substrate, film thickness, impurities and other parameters that can affect the growth of the film.

If the superconductor is subjected to a magnetic field, a current will flow in its surface due to the Meissner effect, until the screening current exceeds a specific value named critical current (I_c) related to the critical current density (J_c) for a given geometry.

Given a temperature well below T_c, if a device is DC biased at its critical current I_c, it will revert back to its induced normal state. In the following sections, we will see how this abrupt transition can be exploited for the benefit of an efficient detection mechanism for photon detectors.

In a superconductor, electrons behave differently as they bind in pairs to form the so called Cooper pair, named after Leon Cooper. In most low-temperature superconductors this pairing can be associated with a small attraction due to the electron phonon interaction. This pair of electrons has a lower energy than the Fermi energy. The BCS theory of superconductivity, for which John Bardeen, John Schrieffer and Leon Cooper received the 1972 Nobel Prize, provides a microscopic theory of this phenomenon.

2.1.2 Single-photon detection mechanism in superconducting nanowire

As the energy of the pairing interaction of a Cooper pair Δ is of the order of the milli-electron volt, thermal energy can easily break up those pairs. A photon, even in the near infrared range with energy hν below 1 eV can therefore break one or more Cooper pairs (if $h\nu > 2\Delta$), producing "hot" electrons (also referred to as quasiparticles) which can themselves lead to the breaking of more Cooper pairs. This phenomenon is the base of the underlying detection mechanism of SNPDs.

The device is made of a thin, typically 4-5 nm thick, NbN mono crystalline film patterned in a meander-like structure. The width of a line is typically in the 100-120 nm range. When a photon is absorbed in a section of that line, it creates a "hotspot", region inside which the superconductivity is locally destroyed. If this meander line is biased with a constant current slightly lower than its critical current (in the range of 80 % to 99 % of I_c), this resistive hotspot will 'push' the flowing current towards the sidewalls of the line as shown in Figure 2-1, since electrons will try to use the lowest resistance path, thus increasing the local current density on the side of the line.

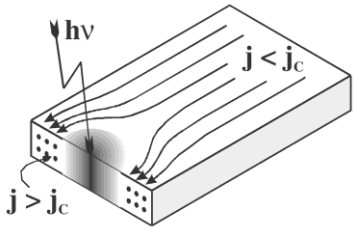

Figure 2-1 Drawing representation of the photon-generated 'hotspot' in a thin film superconductor illustrating the redistribution of supercurrent in the superconducting film - the basis of quantum detection. [28]

Since the thickness is very small, only a few nm, the flow of current and the growth of the hotspot can be considered two-dimensional. If the current bias is high enough, the local current density on the side will be high enough to lead to the self heating of this section of the superconductor due to Joule heating, once the critical current density J_c, associated with I_c, is reached. The original hotspot induced by the photon absorption will grow and expand, until completely blocking the flow of super-current [47]. The generation of resistive barriers has also been explained by the principles of phase-slip-center formation [28] [48] [49] and the detection mechanism has been shown to be related to the interactions of magnetic vortices with radiation quanta [50] [51] [52]. This DC biased resistive barrier will create a small voltage pulse (less than 1 mV) that can be measured by the readout electronic and registered as a photon counting event after appropriate amplification. The thickness of the film was optimized to promote the creation of those hotspots upon absorption of a photon despite the adverse

effect on the reduced absorption coefficient of the film. Indeed, the photon induced hotspot is estimated to be in the range of 80 nm^2 [53] and thicker film would not provide this confinement leading to the creation of a resistive barrier across the entire width and thickness of the 125 nm wide by 4 nm thick stripe.

As the device is kept well below its critical temperature Tc, the hotspot will initially grow and quickly dissipate as it expands along the line. This electro-thermodynamic process occurs in the picoseconds to nanosecond range and depends on the electron-electron and electron-phonon interactions, as well as on the characteristic relaxation time which is itself dependent on the quasiparticles and phonon heat diffusivity to the substrate [54]. Once the excited quasiparticles have recombined into Cooper pairs, the voltage across the device falls back to zero and the device is ready for a new detection event. The dynamic of this process will be presented in section 2.3 by the use of an equivalent electrical model highlighting the presence of the kinetic inductance associated with the Cooper pairs.

2.2 Device geometry and review of fabrication methods

2.2.1 Device geometry

The topology of the devices used in this project is presented in Figure 2-2. A 20 µm by 30 µm NbN patch sputtered on a diced sapphire substrate is patterned as a meander structure, and a gold coplanar waveguide allows its electrical and microwave interconnections.

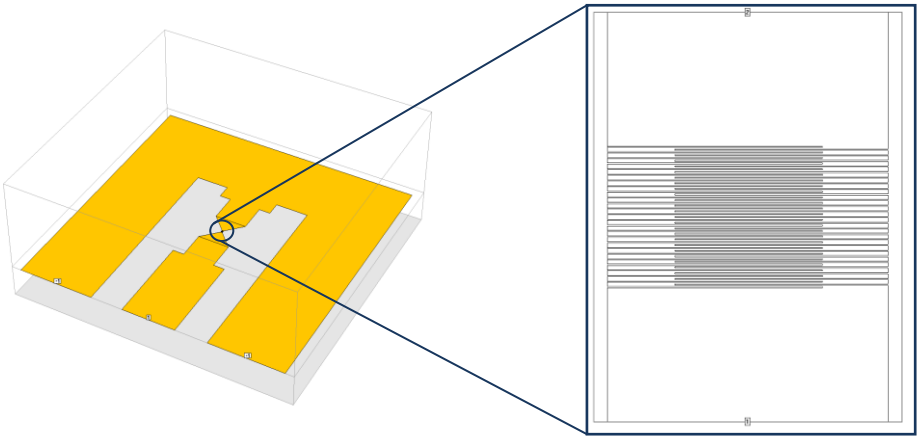

Figure 2-2 Sonnet ® schematic representation of an SNSPD and its surrounding tapered gold coplanar waveguide with three pads (G-S-G). The overall device is about 3 mm by 3 mm. The insert shows a magnification of the meandered structure.

We use devices designed and fabricated at the Moscow State Pedagogical University (Scontel). The scanning electron microscopy of the active area of a device reveals its patterned structure and allows inspection for some possible defects. This particular sample presented in Figure 2-3 will be called device 2 throughout the rest of this work. The active area is segmented in 50 stripes.

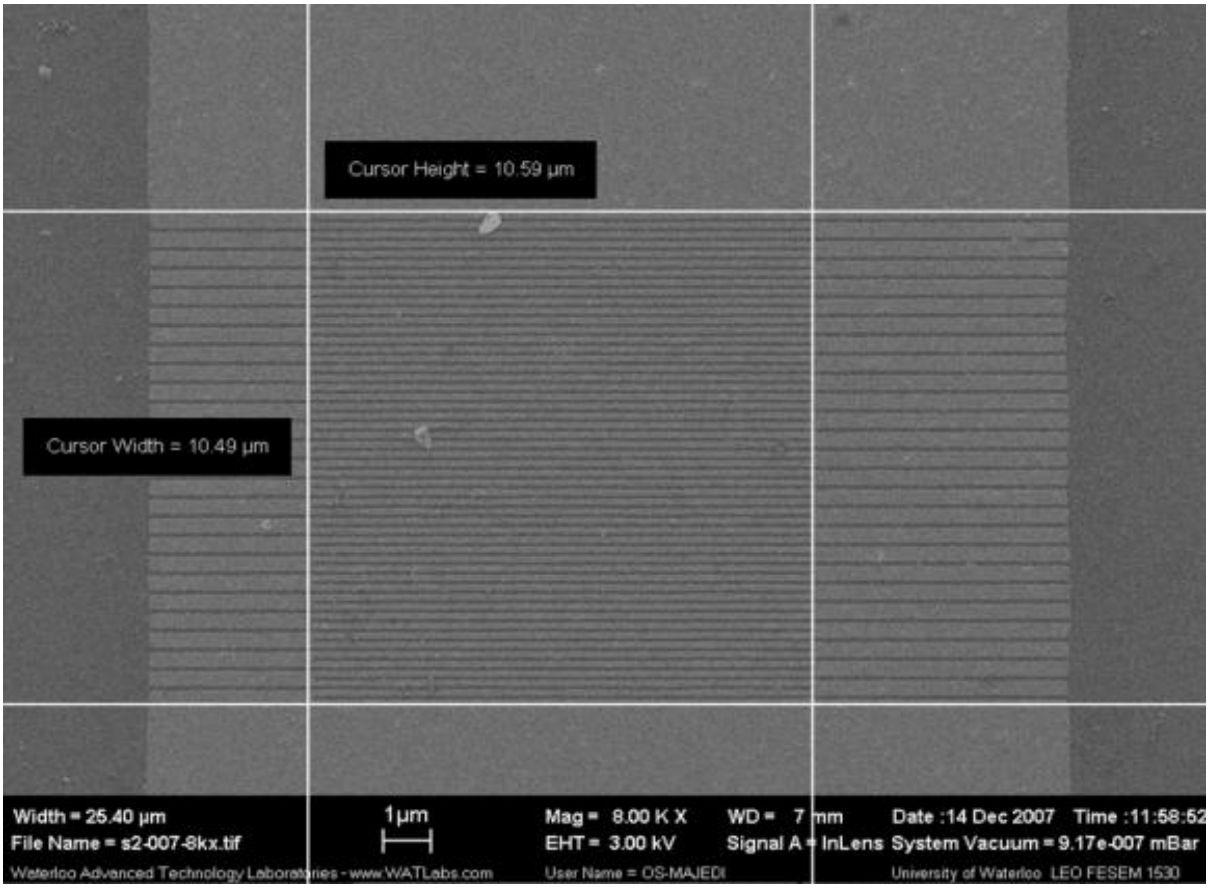

Figure 2-3 SEM of a SNSPD. The active area of the device is delineated with markers which indicate 10.49 µm x 10.59 µm (magnification is 8000x, Watlab, University of Waterloo).

The filling factor of a device is defined as the ratio of the area of a region filled with a film of NbN to the overall active area of the device. The closer to 1 the filling factor is, the more NbN surface can potentially be exposed to the incoming photons and possibly generate a hotspot leading to a photon detection event. From Figure 2-4, the filling factor of the devices used can be estimated to be about:

$$filling\ factor\ \approx \frac{125}{(125+90)} \approx 0.6 \tag{2.1}$$

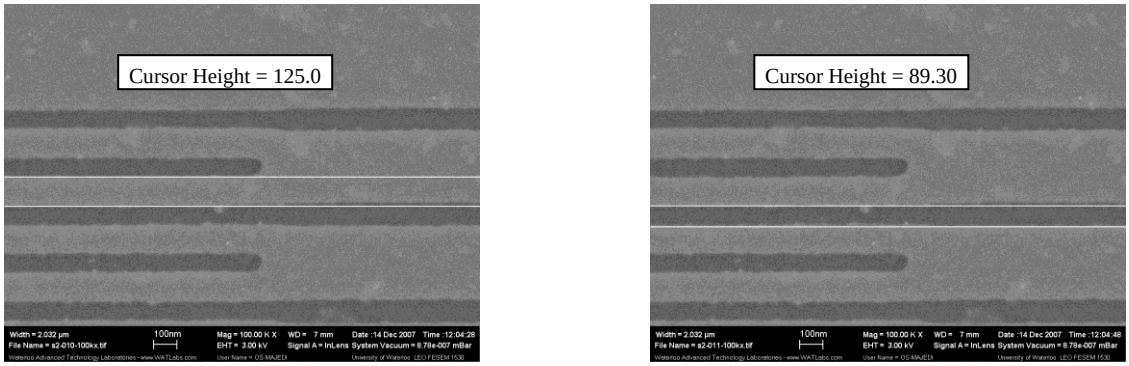

Figure 2-4 Zoomed SEM images of device 2. The width of a NbN line is about 125 nm and the pitch is about 90 nm (magnification is 100000x, Watlab, University of Waterloo).

However the quantum efficiency of SNSPD will depend not only on the filling factor of the meander like structure, but as well on the photo-absorption coefficient and reflectivity of the thin film of NbN. The quality of the film, its uniform crystal structure and purity affect the QE of the device as well as they modify the critical temperature and the critical current density of the 4 nm thick film.

2.2.2 Review of fabrication steps

2.2.2.1 Choice of substrate

The two most frequently used substrates to grow thin film NbN layers to fabricate SNSPD are R-plane sapphire (1102) and MgO (100) orientated. They both have a large energy gap and are chemically stable. Their optical properties (high transparency for visible and infrared wavelengths) are well suited for the application of photon detection given a particular light coupling scheme where the light had to go through the thickness of the substrate for example. As they show a low loss tangent, they are also very well suited for embedding high frequency components and low loss transmission lines.

Certainly, the most important parameter related to the epitaxial growth of very thin films of NbN is the crystalline lattice match with this substrate. In its cubic – B1 phase, NbN behaves as a superconductor below T_c. The other crystal phases are metallic and are not superconducting in their pure form. Although sapphire and MgO are the most widely used substrates for SNSPD implementation, recent developments by F. Marsili showed the successful deposition of high-quality NbN thin films at low temperature on GaAs substrate, permitting the monolithic integration with microcavities and waveguides [55]. Indeed, GaAs cannot withstand the high temperature commonly used to deposit NbN on sapphire for example (500 to 900 $^{\circ}$C) as the arsenic outgases in those range of

temperatures. Aiming towards the lowest deposition temperature of the substrate possible during deposition, while still maintaining a high quality film (characterized by a high current density and good uniformity), is of prime importance and one of the areas of research in this community. High quality films on silicon substrates would also allow the integration with other superconductive structures or waveguides.

2.2.2.2 NbN growth conditions by DC magnetron sputtering and film characterization

DC magnetron sputtering is the usual epitaxial technique used to deposit thin films of NbN. A high purity niobium target is sputtered in the presence of a mix of argon and nitrogen as presented in Figure 2-5. The target voltage, vacuum level, partial pressure of the gases and substrate temperature are used to regulate the growth and the final quality of the deposited film.

In order to achieve a film with a critical temperature comprised between 9.2 K (T_c of Nb) and 16 K (T_c of bulk NbN), the proper cubic phase needs to be grown and this depends on the previously mentioned control parameters for this process.

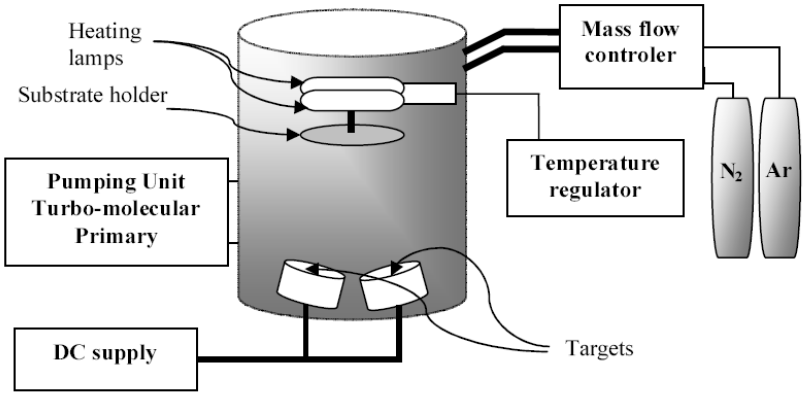

Figure 2-5 DC magnetron sputtering apparatus used to deposit NbN thin film [56]

The film uniformity across the wafer is highly dependent on the absolute pressure controlling the mean free path of the ionized particles and the niobium source size (the bigger, the more uniform the film across the substrate is). The use of precisely calibrated mass-flow controllers or residual gas analyzers and a gas mixer is highly recommended, as the nature of the film deposited varies greatly with small variation of the composition and flow of those gazes in the proximity of the substrate.

In addition, a precise control of the shutter is important for reproducible deposition. Indeed, with the commonly used process parameters, the growth speed can be close to 1 nm per second, and obtaining a 4 nm thick film every time requires a high level of reproducibly.

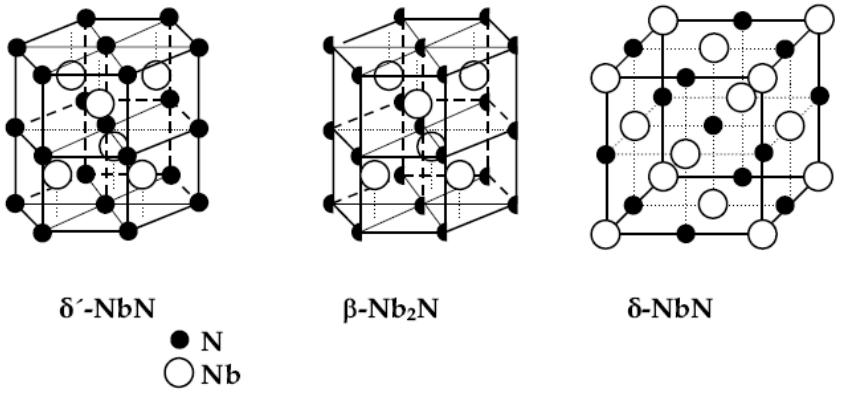

Figure 2-6 Elementary cell of the crystalline structure of the three deposited Nb-N phases. Hexagonal δ´-NbN, β-Nb2N and cubic δ-NbN. For β-Nb2N, only half of the nitrogen sites are occupied [56].

Figure 2-6 presents 3 of the possible crystal structures that can be commonly obtained. However, only the cubic phase is desirable and the lattice constant is usually measured with X-ray diffraction to be a_0 = 4.45 Angstrom. Figure 2-7 shows the various NbN crystal phases obtained depending on the partial pressure of nitrogen in the vacuum chamber as well as the temperature of the substrate.

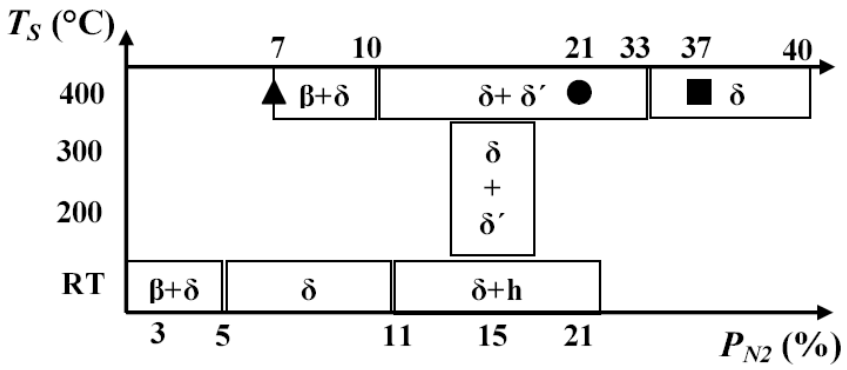

Figure 2-7 Phase composition of NbN film system as a function of the nitrogen partial pressure PN2 and substrate temperature Ts. ▲,● and ■ represent positions of single β, δ´ and δ (used for the study of single phases), respectively. The boundaries are approximate. [56]

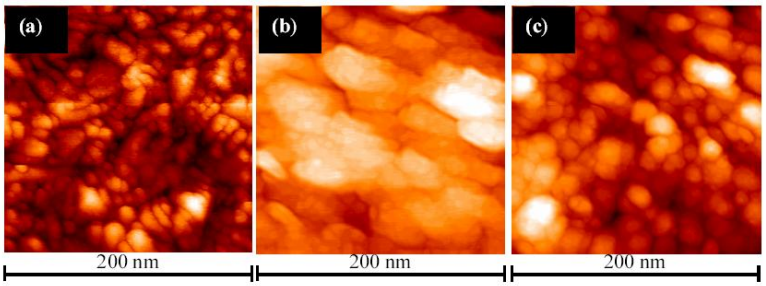

Figure 2-8 STM images of hexagonal β-Nb2N (a), hexagonal δ´-NbN (b) and cubic δ -NbN (c) films. [56]

In the above colored STM images, we can clearly see the difference in grain size between the different crystal phases of Nb and NbN. The size of those grains will affect the electron transport and the overall superconducting properties of the film. It is possible to modify the film in order to optimize its characteristic and uniformity by annealing it after the deposition. However this will not affect its intrinsic composition. The critical temperature of a superconductor is usually given while referencing to the bulk properties of the material. However, when depositing films only a few nm thick, the critical temperature can vary due to the grain boundaries and the possible mismatch to the lattice of the substrate used. Figure 2-9 shows an example of those variations recently reported.

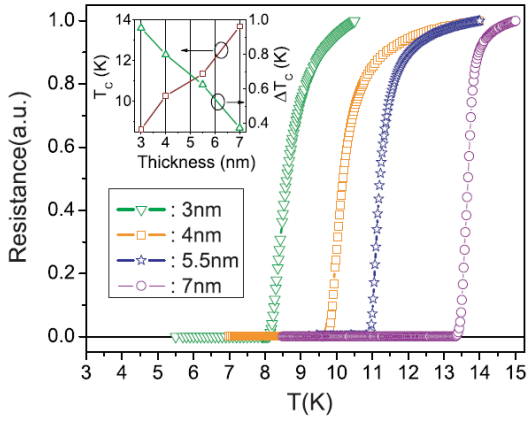

Figure 2-9 Resistance versus temperature dependence of NbN films for four thicknesses: 7 nm (circles), 5.5 nm (stars), 4 nm (squares) and 3 nm (triangles). The deposition conditions were: Ts = 400 ˚C, Ip = 250 mA, Ptot = 2.5 mtorr, 33 % N2, R = 3 A° /s. Inset: T_c and Δ T_c vs. thickness (t). T_c vary from 13.7 K (ΔT_c = 0.4 K) for t = 7 nm to 8.6 K (Δ T_c = 0.9 K) for t = 3 nm. [43]

2.2.2.3 Nano-patterning

In order to reach the needed high filling factor of the meander line structure, only electron beam lithography associated with reactive ion etching have shown to perform well for this type of devices.

It could be envisioned that in the future other lithographic technique based on nano-instrumentation like AFM probe [57] or immersion lens and deep UV could be used to refine the nano-metric pattern.

After superconducting film deposition, the substrate is then spin coated with a direct e-beam resist of a few nanometer thickness, usually in the range of 0.08 µm-thick PMMA 650 K 2 % electron resist layer. The uniformity of the deposited resist is critical to the proper delineation of the stripes of NbN film during etching. Villegier and Poizat group reports the use of the following process parameters for their e-beam writer: U=30kV, I = 15 pa, dose = 230 $C.cm^{-2}$ [19].

Various combinations of resist and energy of electron beam are possible and process dependent. One parameter to consider is the 'reflectivity' of the NbN film to the stream of high energy electron and the backscattered flux that can constructively or destructively interfere and affect the line edge quality during etching. Figure 2-10 shows a device that was exposed in a non optimum fashion as we can see some ghosting effect on the side, and non uniform spots on the entire device.

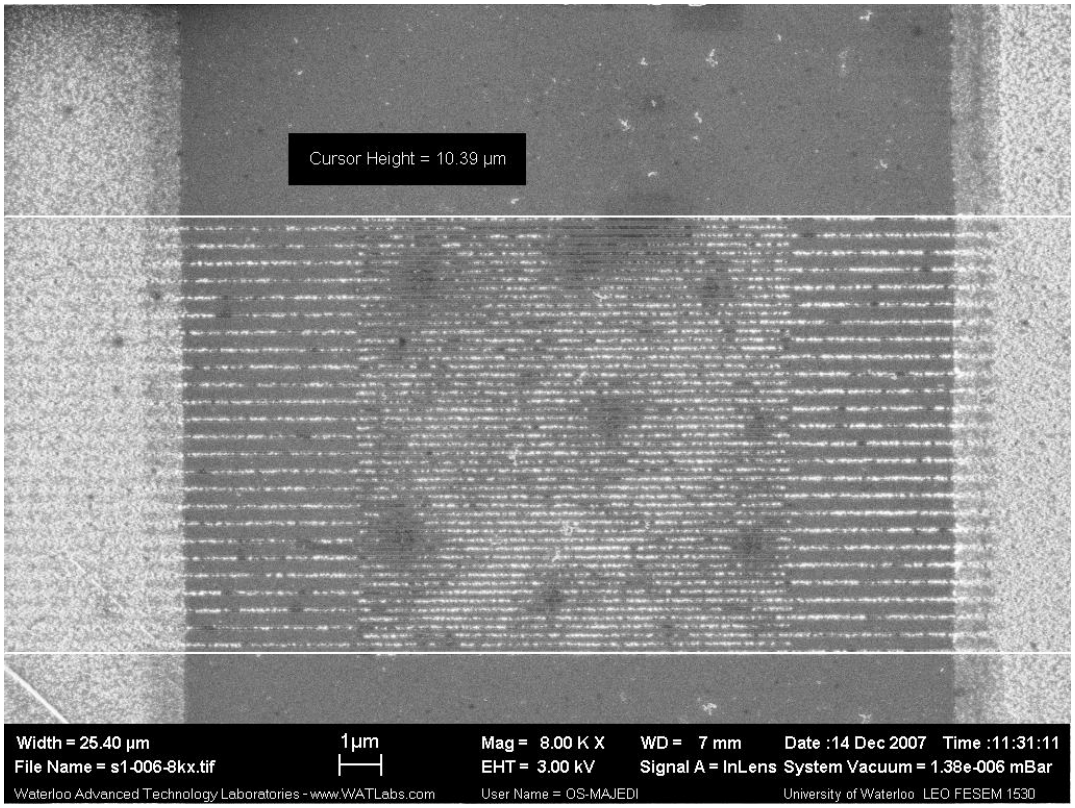

Figure 2-10 Sample of a NbN SNSPD (device 1) showing the issues associated with the e-beam patterning and the reactive ion etching when the dosage are not optimum. The device is still performing but has low quantum efficiency. (Magnification is 8000x, Watlab, University of Waterloo).

This sample will be called device 1 throughout the rest of this work. As the optoelectronic characterization will show in chapter 4, it is still functioning but the QE is greatly reduced compared to the device shown in Figure 2-3 . A closer examination at device 1 showed that some possible leftovers of resist or chemical component remained in the gaps separating two consecutive stripes of NbN after etching, and that the edges were not as uniform as and properly defined as for device 2.

Figure 2-11presents the different steps involved in the fabrication of NbN SNSPD. Only two layers of metal are required: the superconducting material and a gold coplanar waveguide (or Ti/Au). It is a fairly simple fabrication process since the number of steps is quite low compared to processes used in semiconductor industries. After the electron beam patterning, the exposed resist is removed and the NbN is etched using reactive ion etching with SF6 gas and oxygen.

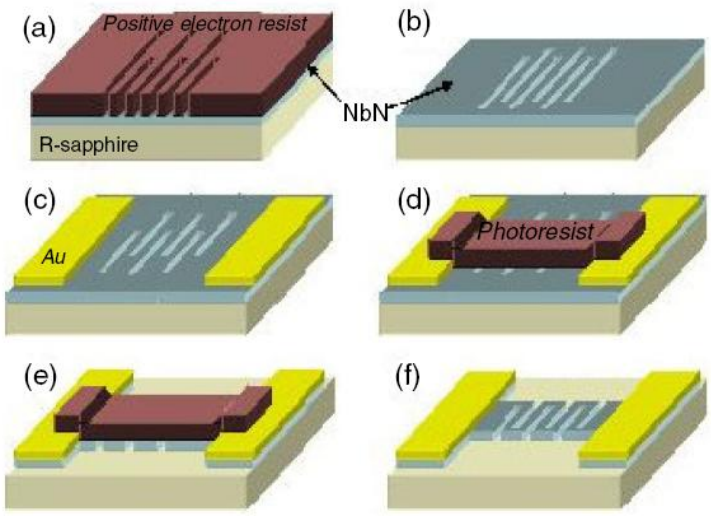

Figure 2-11 Detector fabrication process: (a) Patterning of 200 nm wide stripes using direct electron beam lithography with PMMA electron resist on the thin NbN film. (b) RIE of the NbN film with SF6 and removal of the resist layer in oxygen plasma. (c) Ti/Au lift-off of the contact pads. (d) Optical lithography with AZ1512 photoresist to protect the pixel area then (e) RIE in SF6 + O2 of unprotected NbN and removal of the photoresist. The NbN meander structure appears in (f). [19]

The gold microwave structure is then deposited while the active area is protected with resist and the extra gold removed using a lift-off technique. The final steps involve removing the excess of NbN and define the active area shape by protecting the sensor area with resist and proceeding to a second RIE etch. The resist is then removed and the device fabrication is complete.

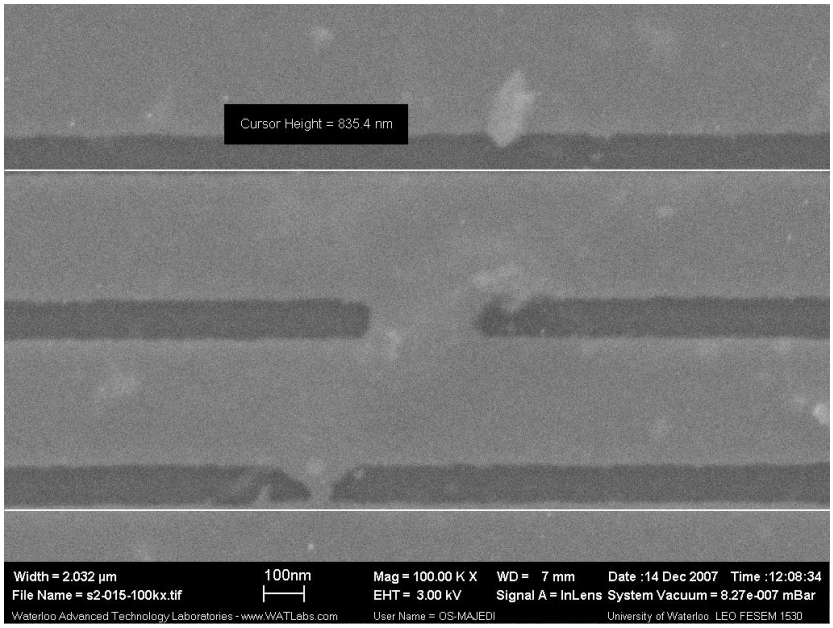

Figure 2-12 High magnification of a portion of the detection area showing only 4 rows of the NbN patterned film which have some shortcuts in between two successive rows due to improper etching or patterning. Those defects do not prevent the proper behavior of the device but affect its effective active area, as the current has now more than one path to follow. (Magnification is 100000x, Watlab, University of Waterloo).

As shown in Figure 2-12, the patterning and etching steps can lead to degradations in the film which can affect its proper behavior or simply reduce its photo-detection properties. In this figure we observe nano-sized bridges between rows of the meander structure, shortcutting the flow of current and therefore reducing the active area of the detector by 3 rows.

It is therefore of prime importance to refine the fabrication steps until a good uniformity of the pattern edges is obtained. A roughness of even a few nanometers can greatly affect the maximum current density of a single row which is itself a few nanometers wide. The non uniformity of the thickness, which is usually 4 to 5 nm, will constrict the flow of current and will limit the maximum critical current of that row effectively reducing the QE of the entire device. [58]

2.3 Electrical device modeling

2.3.1 Simple electrical model for SNSPD

In order to understand the shape and amplitude of the voltage generated upon detecting a photon, it is interesting to look into a commonly used simple electrical model of the superconducting device. Once the superconducting device is under a steady state DC bias, the Cooper pairs have acquired a certain

momentum. Trying to change the direction or the flow of a steady supercurrent requires a certain force F to be applied to those Cooper pairs in order to change their momentum. This gives rise to an inductance called kinetic inductance which expression can be derived from the force acting on the pairs. [59] [60]

$$F = \frac{d}{dt}(m^*.v) \tag{2.2}$$

Multiplying by $\frac{n^*.q^*}{n^*.q^*}$, we obtain:

$$q^*\vec{E} = \frac{d}{dt}\left(\left(\frac{m^*}{n^*.q^*}\right)(n^*.q^*.v)\right) \tag{2.3}$$

Dividing both sides by q^*, we obtain:

$$\vec{E} = \frac{d}{dt}\left(\left(\frac{2m_e}{n^*.q^{*2}}\right).\vec{j}\right) \tag{2.4}$$

Where

$m_e = electron\ mass = 9.10938215(45) \times 10^{-31}\ [kg]$

$m^* = Cooper\ pair\ effective\ mass\ [kg] = 2m_e$

$v = Cooper\ pair\ drift\ velocity\ [m.s^{-1}]$

$\vec{E} = electric\ field\ [V.m^{-1}]$

$q^* = charge\ of\ a\ cooper\ pair\ [C] = 2e$

$n^* = Cooper\ pair\ density\ [\#.m^{-3}]$

$\vec{j} = current\ density\ [A.m^{-2}]$

The voltage across a structure with length l and cross sectional area A is obtained by integrating the obtained expression for the electric field with respect to the length of the structure, assuming a uniform current distribution in the nanowire:

$$V = \frac{d}{dt}\left(\left(\frac{m^*l}{A.n^*.q^{*2}}\right).\vec{j}A\right) \tag{2.5}$$

$$V = \frac{d}{dt}(L_k I)\ [V] \tag{2.6}$$

Where $L_k = \left(\frac{m^* l}{A.n^*.q^{*2}}\right)$ [H].

Figure 2-13 represents a simple model for an SNSPD where the kinetic inductance is in series with a resistor representing the hot spot occurring during a photo-detection event. The magnetic inductance associated with the physical nanostructure can be neglected compared to the magnitude of the kinetic inductance. When the device is not optically excited, the switch is closed and the SNSPD shows no resistance to the DC current applied to it. The 50 Ω resistor in parallel represents the typical input impedance of a microwave cable and instrumentations used to measure the voltage pulses across the device. This resistor is shorted when the switch is closed. The photon absorption and hotspot formation is modeled by opening the switch for a few picoseconds before closing it again. The energy stored in the kinetic inductor will dissipate through this 50 Ω impedance.

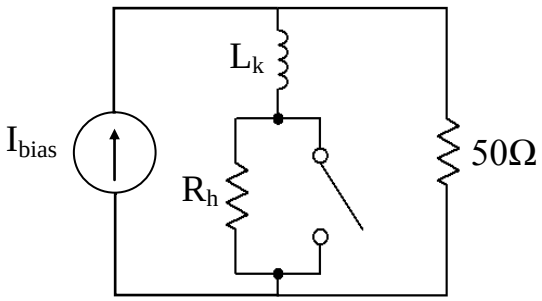

Figure 2-13 Simple electrical model representation of an SNSPD connected to a 50 Ω load in parallel.

Circuit analysis of this electrical model reveals that the voltage pulse will have a rise time τ_{rise} and a fall time τ_{fall} related as follow:

$$\tau_{rise} = \frac{L_k}{R_h + 50} \tag{2.7}$$

$$\tau_{fall} = \frac{L_k}{50} \tag{2.8}$$

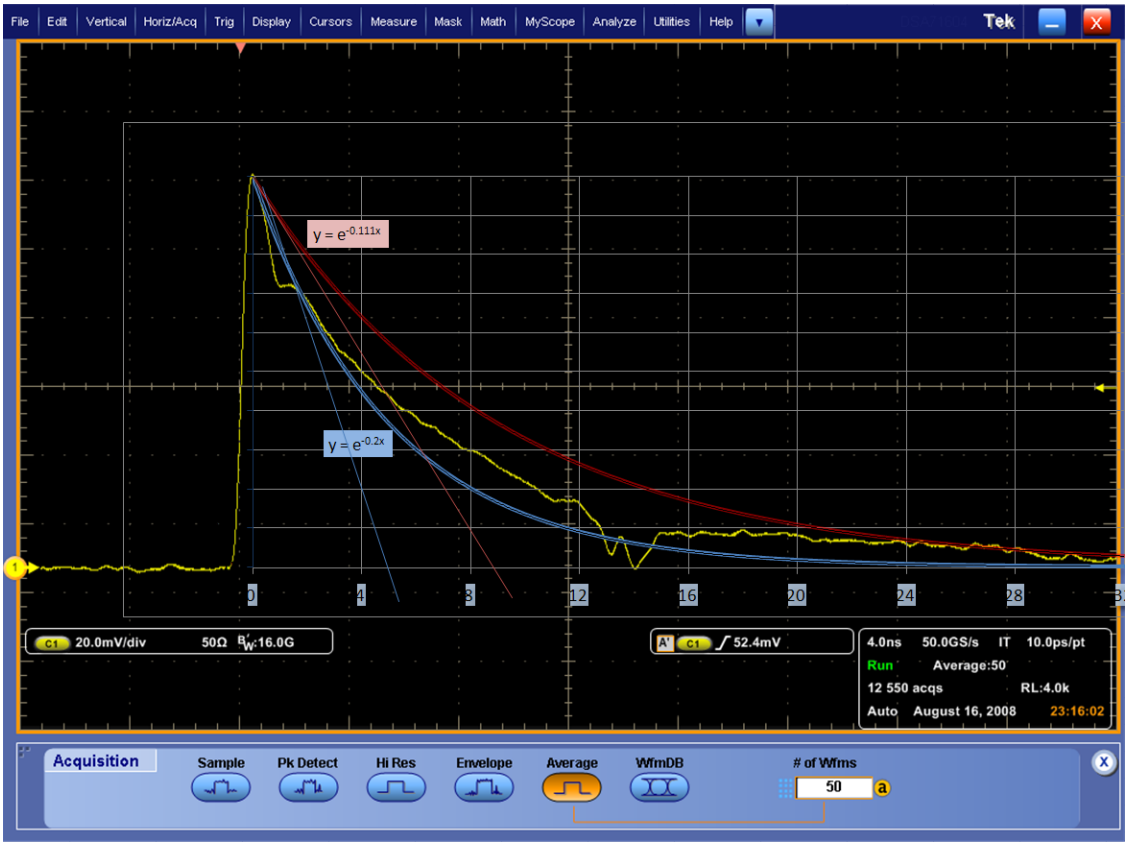

Figure 2-14 50 SNSPD voltage responses averaged obtained for device 2 with two overlaid curves $e^{-\frac{t}{\tau_{fall}}}$ for $L_k = 250\ nH\ (blue)\ and\ 400\ nH\ (red)$.

Figure 2-14 shows in yellow the filtered analog voltage pulse resulting from photo counting events with two overlaid curves expressing the exponential decay time of the voltage obtained from the simple electrical model. The value of the kinetic inductance is estimated to be between 250 nH (blue) and 450 nH (red). The rise time between 10 % and 90 % of the pulse peak voltage is found to be on average 360 ps. However the rise time of the Philips Scientific 6954 amplifier is specified as being 220 ps and precise estimation of the hot spot resistance cannot be inferred directly (estimated to be between 500 Ω and 1.5 KΩ).

2.3.2 Electrical system SPICE model

In order to refine the initial model presented in 2.3.1 and take into account the various effect of the measurement apparatus itself a more detailed SPICE model was incrementally constructed and is shown in Figure 2-15.

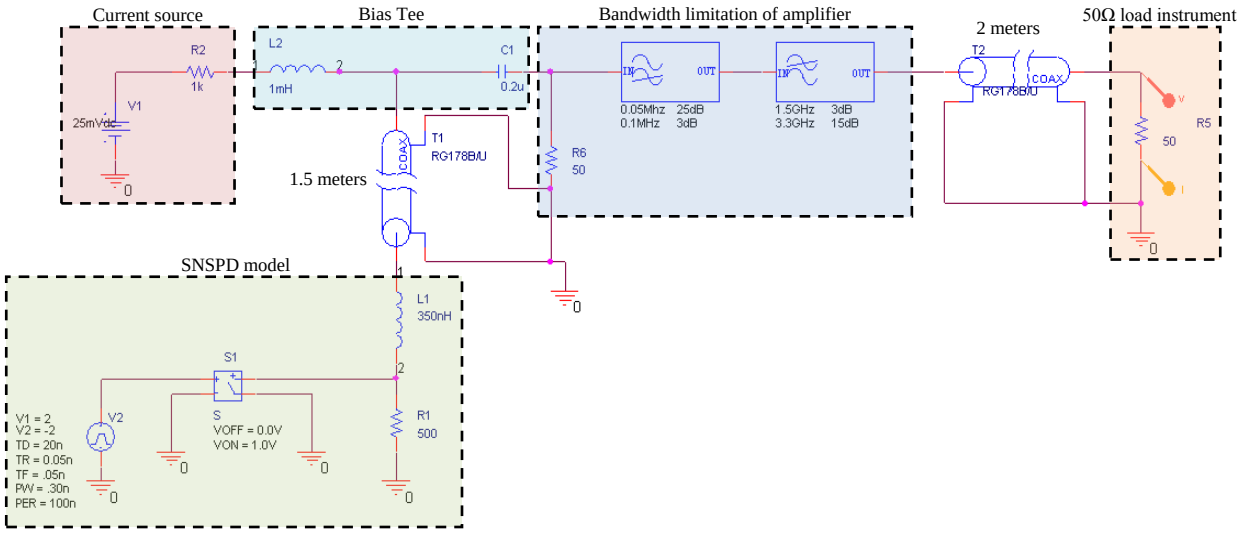

Figure 2-15 Pspice Schematic used to model the SNSPD response. The various functionalities are highlighted : current source, bias Tee, SNSPD electrical model, limitation bandwidth of the amplifier used (the gain is omitted), the correct length of RF coax cables used in the setup and an ideal 50 Ω load to represent the measurement apparatus used to detect the pulses.

A current source modeled as a voltage source in series with a resistor is fed into a microwave bias tee for which the value of the capacitor C1 was carefully measured from the one used for those experiments. The SPICE microwave cable model takes into account its impedance, relative speed and geometry affecting the inductance per meters and the capacitance per meter of the cable. The proper length of the cable was entered to reflect as close as possible the effective length of the cables used in the system presented in chapter 3. Note that the gain of the amplifier is not taken into account as only its bandwidth limitation was relevant for this analysis. It is modeled as a low pass filter in series with a high pass filter with 50 Ω input impedance. The current path through the resistor R1 is determined by a pulse controlled switch that will replicate the lifetime of a hot post to a few picoseconds. The value of the inductor and R1 were adjusted based on estimation of those values for the devices tested until a good match between the simulation and the acquired curve was obtained as shown in Figure 2-16.

Comparing Figure 2-14 and Figure 2-16 it is interesting to note that the SPICE simulation correctly calculated the small dip present after the fast rise time voltage peak is reached (at time = 37.5 ns in Figure 2-16). It was observed that this dip is created by the limited bandwidth of the amplifier (around 1.5 GHz) for which the set of S parameters is shown in Figure 2-17. The voltage standing wave ratio VSWR is only less than 2 below 900 MHz which means part of the high frequency

components of the pulse will be reflected back to the device after propagating twice the distance of the 1.5 meters cable (which translates approximately into twice 7.1 ns with a relative speed of 70 % of c_0 in the RG cable).

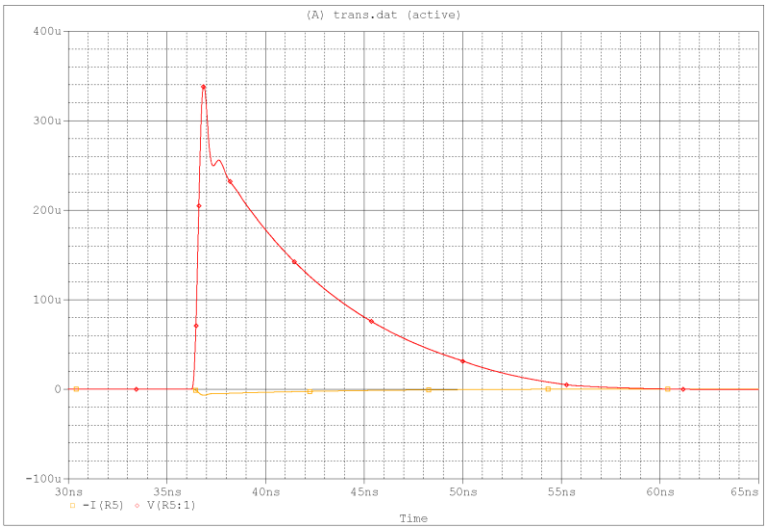

Figure 2-16 Spice simulation results for the electrical schematic of the measurement setup. The value of the kinetic inductance (L1 in the schematic) is adjusted until a good match with the measured SNSPD response is obtained for the fall time.

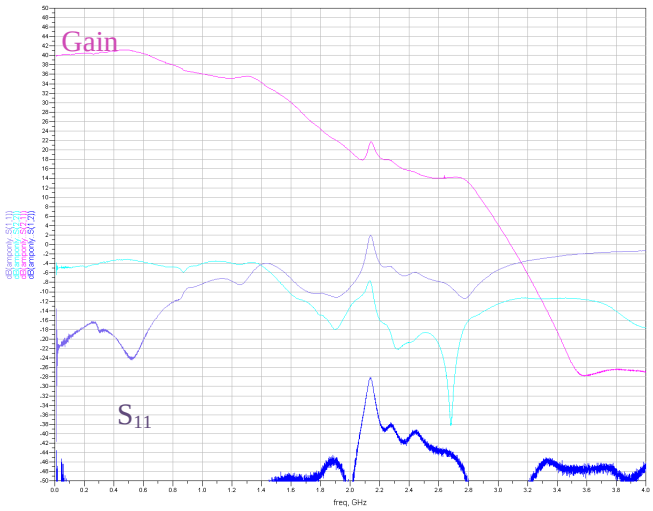

Figure 2-17 S-parameters set measured for the Philips Scientific fast pulse preamplifier model 6954 used in the following experiments. (Amplifier biased with a 12 V lead acid battery).

This non ideal input impedance of the amplifier was simulated by modifying its input impedance in the SPICE model by setting R6 to 40 Ω. A dip in the voltage curve occurred as shown in Figure 2-18 at 14 ns after the pulse rose to its peak exactly as in Figure 2-14.

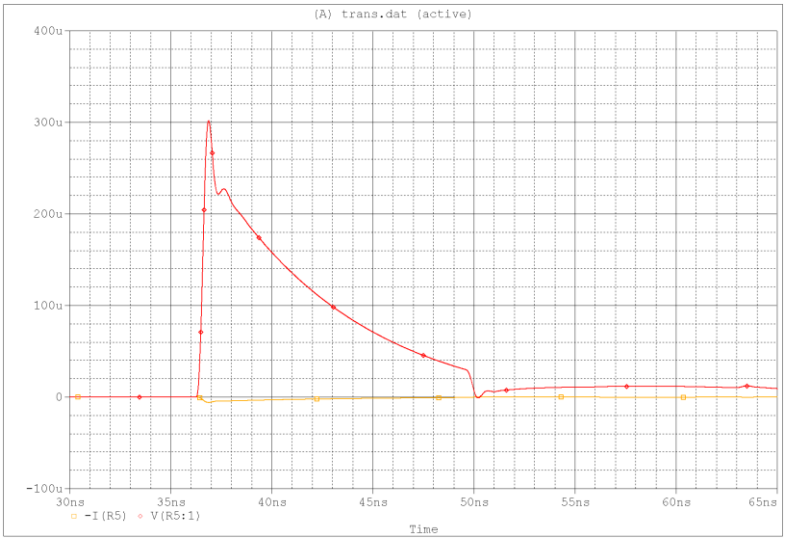

Figure 2-18 Spice simulation results obtained for the electrical schematic of the measurement setup after R6, the input impedance of the amplifier model was set to 40 Ω. (Red curve is the voltage across the 50 Ω load, yellow curve is the current variation across the load.)

This SPICE model analysis and comparison give insights into the behavior of the device and its physical parameters as well as how the measurement apparatus modify the nature of the pulse in the time domain and help refining better measurement techniques. Modeling the kinetic inductance is important for understanding the speed limitation of the devices [61] as its magnitude is directly proportional to the length of the superconducting nanowire and increases as the wire width and thickness decreases.

Having a large device with high filling factor and very thin film will lead to a slow device with the current setup (50 Ω load). Indeed, we measure from Figure 2-14 that the device needs about 30 ns to fully recover to its non excited state where it is ready to accept a new photo event with the same likelihood to generate a voltage pulse upon absorbing the photon.

The formula for the fall time shows that a possible strategy to decrease the recovery time of the SNSPD would be to add a matching network (series resistor for example) to increase the impedance "seen" by the device.

Chapter 3
Experimental setups preparations and verifications

Packaging of optoelectronic devices often corresponds to a large portion of the cost of manufacturing and in the case of laser diodes for example, the costs involved in the precision handling and alignment for the packaging often represent many times the cost of the bare diode. In order to characterize efficiently and accurately SNSPDs, the packaging, cryogenic, optical and measurements setups should provide:

- Good thermal anchoring of the device and stable temperature around 4.2 K
- Efficient shielding against electromagnetic radiation from DC to hundreds of terahertz (electrical noise to stray light from environment)
- Structural stability, as any contraction or expansion of the material will affect the optical alignment made at room temperature (almost 300 degrees gradient)
- Long and stable operation for low-cost operation (minimize liquid helium consumption)
- The experimental characterization setup should allow the acquisition of reproducible results and be automated for efficient characterization.

The following sections present the strategies implemented in order to achieve these requirements, namely the cryogenic packaging and dipper probe setup, the optical setup, optical coupling and electrical setup.

3.1 Cryogenic setup

3.1.1 Packaging requirements, design and fabrication

While copper is the commonly used metal to fabricate parts and device holders to operate in a cryogenic environment due to its excellent thermal (630 W/(m.K) at 4 K [62]) and electrical conductivities, it does not provide the rigidity and resilience to thermal contraction required for the optical alignment of a single mode fiber to a photo detector active area when the latter has almost the same area as the mode field diameter of the laser pulse confined in the core of this fiber. Our approach makes use of a controlled expansion alloy made of iron and nickel, namely Carpenter Invar 36 ®. Indeed the precise amount of nickel in this alloy, 36 %, gives this material a total thermal linear expansion coefficient between room temperature, 294 K, and 4 K of : $\Delta L/L_{294K\text{-}4K} \approx 0.037$ % (for

ETP copper, $\Delta L/L_{294K\text{-}4K} \approx 0.324$ %) [62]. Choosing a material that matches or is as close as the coefficient of thermal expansion of the substrate of the device used is an important consideration.

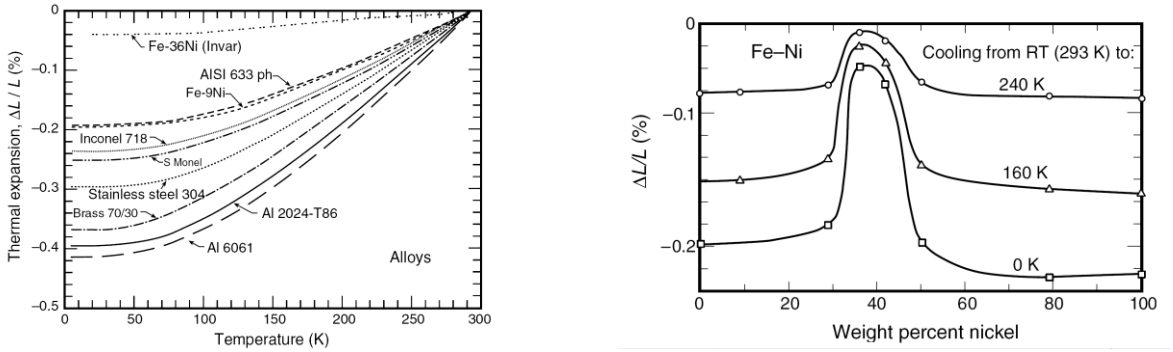

Figure 3-1 (Left) Thermal linear expansion ΔL/L = (Lτ-L293)/L293 of common alloys [62]. (Right) Thermal expansion on cooling from room temperature for the Fe–Ni alloy system at different compositions, showing the "Invar" region near 36% Ni composition (from Clark 1968). [62]

A suitable material for cryogenic operation for such a package is not only one that has a low coefficient of thermal expansion between room temperature and 4 K but is also one that experiences low magnitude fluctuations and a slow rate of change of expansion while cooling down. Invar 36 ® exhibits such properties. Although it has a low thermal conductivity at liquid helium temperature (0.24 W/(m.K)) [62], this characteristic provides the advantage of enhanced thermal stability for the operation of SNSPD as cryogen free refrigerators often suffers from temperature fluctuation over time [1]. The iron and nickel content give this material a relatively high permeability compared to copper, which can further be optimized by different hydrogen annealing techniques if necessary.

Before machining the different parts of the SNSPD packaging, the hot forged and descaled raw blocks were stressed relieved at 80 ºC in an oven for 2 days which included a slow cool down of about 8 hours. While machining the parts, it is important to maintain a constant feed rate to avoid self hardening and changes in the crystal composition of the alloy at the interface with the carbide tools. Parts are then cleaned in an industrial degreaser solution and in an ultrasonic bath before being heat treated in a nitrogen saturated clean room oven programmed with various sequences of temperature ramps, plateaus, and cool down periods, above and around the Curie temperature of this alloy (277 ºC) in order to demagnetize it and release any stress accumulated after the machining operations. The overall procedure took about 8 hours after which the parts were left to cool down overnight in the closed oven. The different parts where then finely polished, lapped with alumina slurry, and cleaned again in the same way before the electroplating step. The packaging and the SNSPD mounting plate

were plated with 1µm of nickel to promote the adhesion of an electroplated gold layer of about 15 µm of 99.99 % purity. Accuracy and flatness of the parts were asserted at various steps of the fabrication and the tolerances of those prototypes were within our stringent expectations.

Figure 3-2 presents a cutaway view of the design drawing. The main body, the cover and the device mounting plate are all made of invar. Only the cover is left non-electroplated as it has been observed that two mating gold plated surfaces under the pressure of the screws could cold weld and would cause the gold plating to peel off when the surfaces are separated. For this reason, a 25 µm thick indium foil was placed under the device mount at the bottom of the packaging in order to easily remove the mounting plate from the body of the package if ever needed.

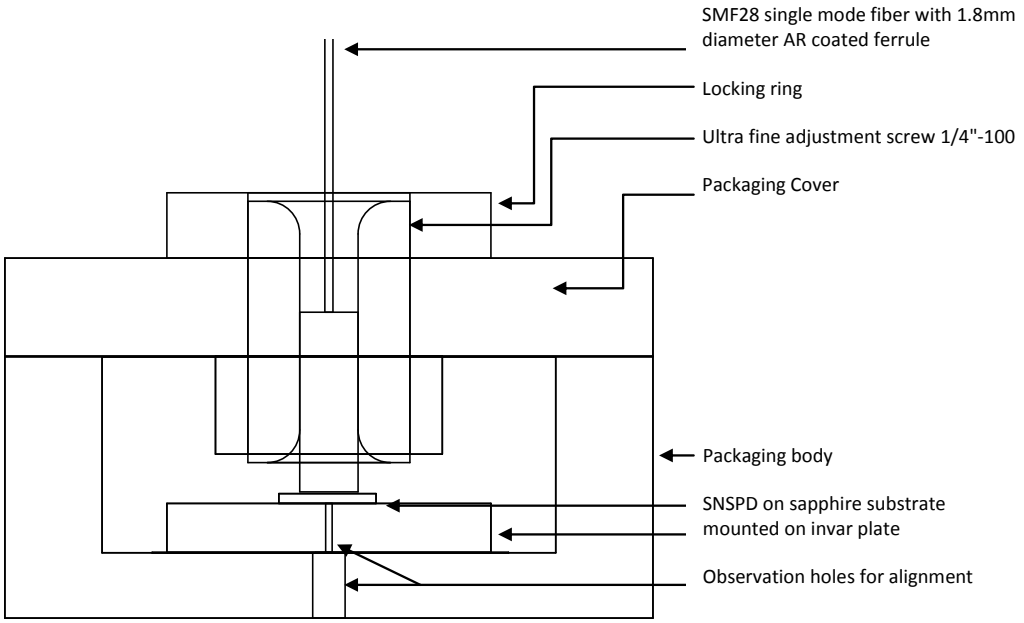

Figure 3-2 Front cutaway view of the CAD drawing of the package assembly.

The dimensions of the body of the package are 20 mm x 20 mm x 8 mm and the cover plate has the same profile but is 3 mm thick. The SMF28 single mode optical fiber is terminated by a 5.5 mm long, 1.8 mm diameter anti-reflection coated ferrule (Thorlabs part number: SMPF0113) held in a modified ultra-fine hex adjuster screws (Thorlabs part number: F25US050). The ball at the tip of the original part was removed and a 1.8 mm hole was bored in the 100 thread per inch screw in order to fit the ferrule which was fixed in place with STYCAST ® 2850 FT epoxy. We tried two approaches for the cover which was either threaded directly to receive the fine pitch screw or drilled to accept the

corresponding Thorlabs bushing. In both cases, a locking ring was screwed at the top which permits fixing in place the optical probe once the height has been finely set (254 µm displacements per revolution).

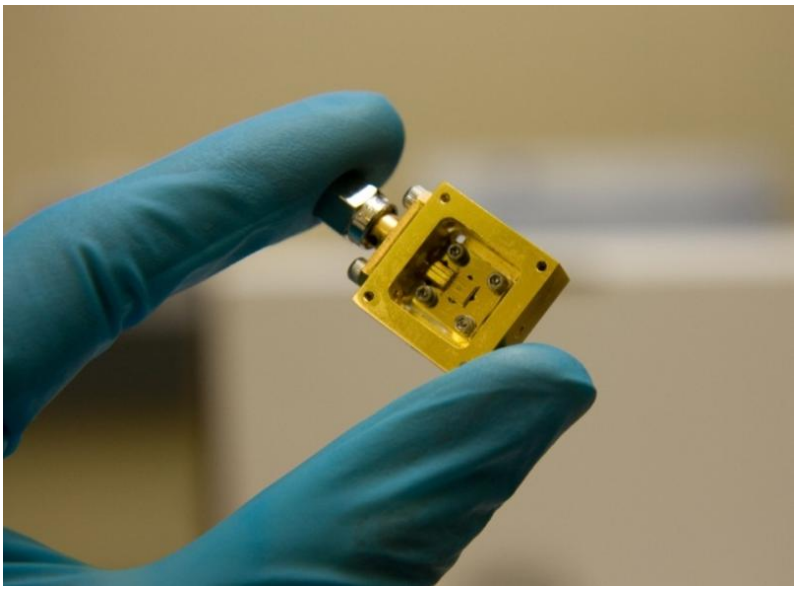

Figure 3-3 Picture of the finished packaging with the SNSPD wire bounded to a 3 mm long FR-4 coplanar waveguide to thermally anchor the center lead of the SMA connector. (Due to adherence issue of the gold wire on the gold surface of the device, cryogenic compatible silver epoxy was used as in [63]).

The device itself is mounted on the plate which has been locally coated with Apiezon ® N cryogenic grease and the active area is aligned on top of the 200 µm observation hole and set in place using the smallest amount of UV curing adhesive. The device's location is then secured using STYCAST ® 2850 FT anchor points in a symmetric way to ensure no movement of the sapphire substrate during a cool down. The device's mounting plate is then tightly fixed in the packaging with four non-magnetic stainless steel screws and spring washers. The center pin of the SMA connector is then spot welded to the coplanar waveguide with a gold ribbon.

Figure 3-3 shows the relatively compact packaging once assembled but without the optical fiber pigtailed lid on.

3.1.2 Dipper probe design and performance

Using a commercial liquid helium Dewar as a cryostat is the least expensive approach to implement an effective cryostat to operate single-photon detectors. A simple dipper probe with a device attached on one side and optical and electrical connectors on the room temperature side provide an economic

way to characterize SNSPDs. One constraint in using this technique is that the opening of the mouth of the Dewar is limited to about 35 mm diameter. Some calculations of the helium consumption are presented as well as the assembly and its testing.

3.1.2.1 Helium budget estimation, heat link

Stainless steel tube dimensions:

- 0.5 inch outer diameter
- 0.038 inch wall thickness
- about 1.5 meters long (1.2 m inside the Dewar)

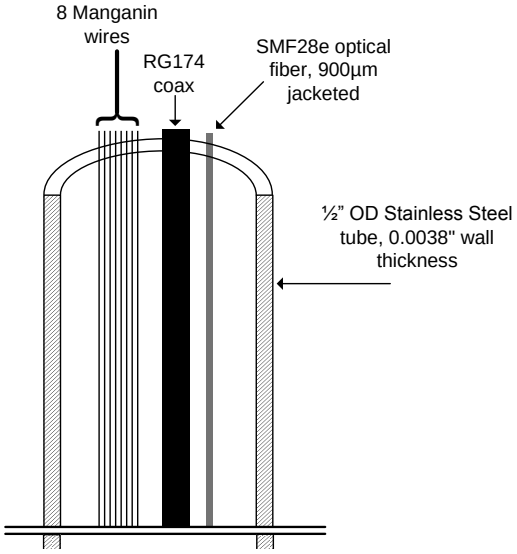

Figure 3-4 Cutaway representation of the stainless steel body of the dipper probe with the various wires and cables running through it that experience a gradient from room temperature to liquid helium temperature.

Heat transferred into the Dewar by the dipper probe is equivalent to:

$$\dot{q}_{in} = \dot{q}_{SS\_tube} + \dot{q}_{Manganin} + \dot{q}_{coax} + \dot{q}_{fiber} \tag{3.1}$$

We can safely neglect the heat input through the optical fiber in this system. Also, the radiation heat inflow into the Dewar through the top flange and the rest of the insulated surface cannot be estimated but the natural boil-off rate of a 60 L liquid helium Dewar is in the range of 1-3 % per day. The rate of liquid helium consumption is known to be about 1.4 L/Wh. Therefore the goal of this heat inflow estimation is to quantify the consumption of liquid helium added to the natural boil-off rate.

Heat transferred through the stainless steel tube:

$$\dot{q}_{ss} = \frac{A}{L}\int_{4K}^{300K} \lambda(T)dT \tag{3.2}$$

We know from reference table A2.1 in [62] that for stainless steel:

$$\int_{4K}^{300K} \lambda(T)dT = 3.06\ kW.m^{-1} \tag{3.3}$$

Therefore

$$\dot{q}_{ss} = \pi.(0.0127).(0.0009652).(1.2\ m^{-1}).(3.06\ kW.m^{-1}) \tag{3.4}$$

$$\dot{q}_{ss} \approx 98.2\ mW \tag{3.5}$$

Heat transferred through eight 250µm diameter Manganin wires for the cryogenic temperature diodes:

$$\dot{q}_{Mang} = 8.\frac{A}{L}\int_{4K}^{300K} \lambda(T)dT \tag{3.6}$$

The parameter of the alloy Constantan is a good approximation for the thermal conductivity integral from 4-300 K for Manganin, namely 5.16kW/m. [62].:

$$\int_{4K}^{300K} \lambda(T)dT = 5.16\ kW.m^{-1} \tag{3.7}$$

Therefore

$$\dot{q}_{Mang} = 8.\pi.(0.000125)^2.(1.2\ m^{-1}).(5.16\ kW.m^{-1}) \tag{3.8}$$

$$\dot{q}_{Mang} \approx 1.69\ mW \tag{3.9}$$

Heat transferred through one RG174 coax cable:

$$\dot{q}_{Coax} = \dot{q}_{Shield} + \dot{q}_{Core} + \dot{q}_{Dielectric} \tag{3.10}$$

A section of the coax cable used was dissected into its various constituent and the following constitution was obtained: The core is made of seven 150µm diameter copper wires. The shield is made of fifty 100µm diameter copper wire braided together and the dielectric is about 2mm diameter. We neglect the heat transferred through the thin plastic coating of the cable.

Using the same method as above we find the following values:

$$\dot{q}_{Coax} \approx 53\ mW + 16.7\ mW + 1.3\ mW \tag{3.11}$$

$$\dot{q}_{Coax} \approx 71\ mW \tag{3.12}$$

Therefore the total heat transferred into the Dewar by the dipper probe is:

$$\dot{q}_{in} \approx 98.2\ mW + 1.69\ mW + 71\ mW \tag{3.13}$$

$$\dot{q}_{in} \approx 171\ mW \tag{3.14}$$

The boil-off gas lowers the amount of heat input through the stainless steel tube by convective cooling of the section of the tube inside the Dewar [62]. Assuming the boil-off gas cooled the tubing with 100 % efficiency, in other words, the enthalpy of the cold helium gas would reduce the heat leak by an estimated factor of 32 when the other extremity is held at room temperature [62]. The latent heat of evaporation of helium is 2.6 kJ/L whereas the enthalpy change of helium gas between 4.2 K and 300 K is about 200 kJ/L. [64]. An efficient design will optimize the use of the cold gas before it escapes the Dewar. Indeed the use of metallic radiation shields is commonly used along the path of the ascending helium gas but for simplicity of realization was not included in this design.

$$\dot{q}_{in} \approx 75.76\ mW\ (with\ cooling\ by\ boil-off\ helium\ gas) \tag{3.15}$$

Therefore the consumption of liquid helium with such a system can be estimated to be about:

$$Consumption\ rate \approx 0.106\ Liters\ per\ hour \tag{3.16}$$

Or

$$Consumption\ rate \approx 2.5\ Liters\ per\ day \tag{3.17}$$

Replacing the copper based coax cable by a less thermally conductive one would further reduce this consumption. The actual consumption showed to be even lower than this estimate (section 3.1.2.3).

3.1.2.2 Dipper probe assembly

The dipper probe system built is comprised of an upper module for the room temperature optical and RF interconnects as presented in Figure 3-5. It provides the ability to test two devices at once and its modular concept makes it versatile, as the top cover can easily be replaced to suit the current needs.

The RF coax cable, optical fiber and thermal sensor leads are running inside a stainless steel tube which can slide within a customized liquid helium transport Dewar top flange by adjusting an Ultra-

Torr ® o-ring fitting. The height of the sub-module containing the device can easily be adjusted and a slow cool down process can be well controlled.

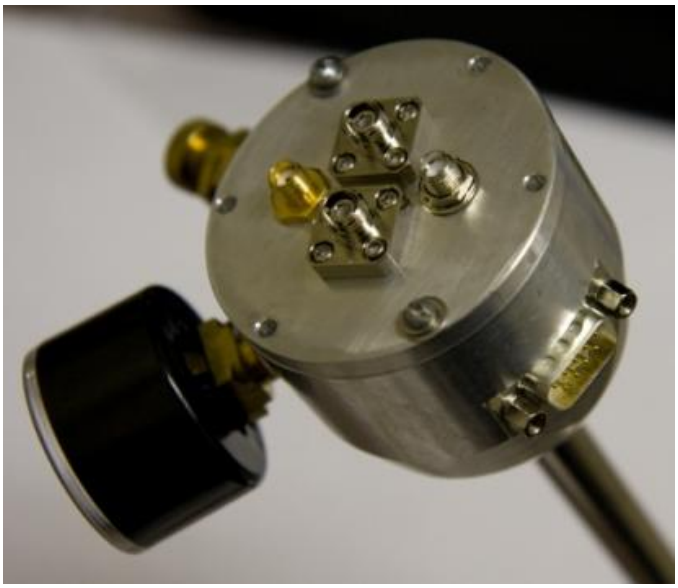

Figure 3-5 Picture of the top of the dipper probe presenting the various inputs and outputs of the system. It has on the top plate, two optical fiber FC/PC mating connectors, two SMA feedthrough connectors, one D-SUB 9 connector for two calibrated thermal sensors (±10 mK error) on the side, a pressure relief valve and a pressure indicator, in case of a leak of the immersed sub-module.

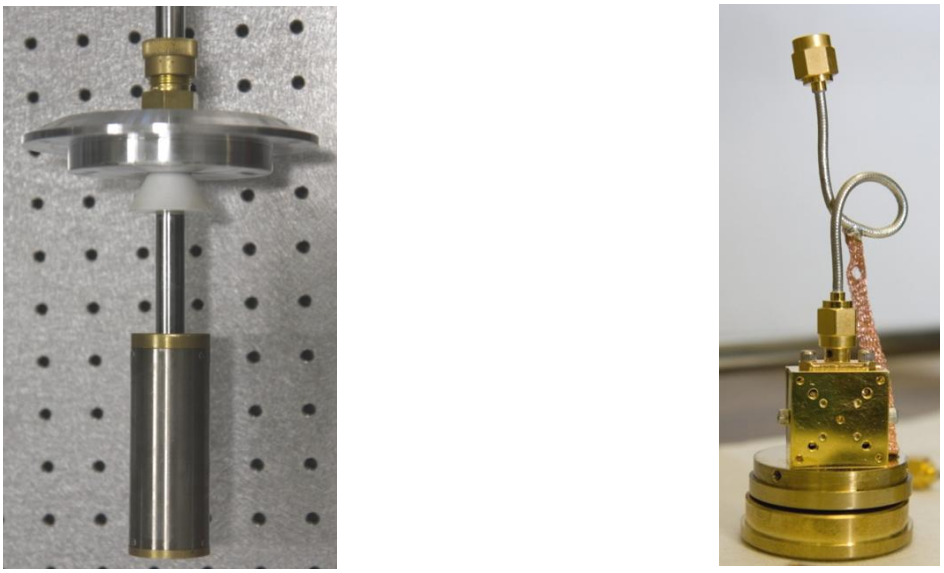

Figure 3-6 (Left) the closed sub-module is shown before installing it in the helium Dewar. (Right) The opened sub-module with the SNSPD package and the thermally anchored semi-rigid coax cable.

The cylindrical parts of this sub-module are made of brass for the top and bottom flange and nickel plated copper tube for the main body. A sheet of mu-metal also covers the inside walls of this structure for increased electromagnetic isolation of the device. A custom made 1.5 V lithium battery powered DC current supply is used with which we can precisely adjust the current within tens of nanoamps and other equipments as presented in our experimental setup in [63].

Figure 3-7 Overall view of the dipper probe structure.

3.1.2.3 Results, temperature plateau, stability

Figure 3-8 is a resistance versus temperature curve of a NbN SNSPD, showing the highly resistive nature of niobium nitride thin film at room temperature, a few mega ohms, and the abrupt change occurring between 9 and 10 Kelvin. It is interesting to note that the resistivity of the material actually increases while cooling down from its room temperature state before abruptly transiting to its superconducting state.

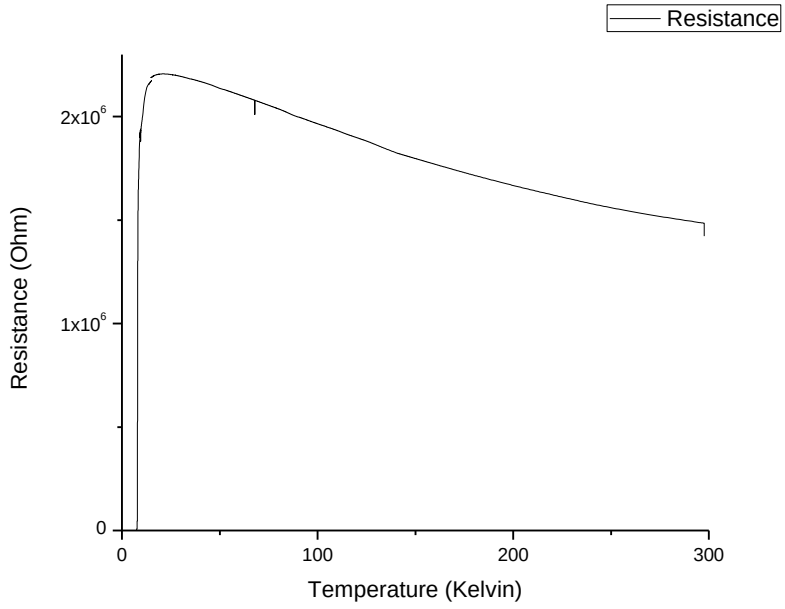

Figure 3-8 Resistance versus Temperature of a 4.5 nm thin NbN film meander structure with 500 µm length.

When the enclosure was immersed in the liquid helium, the temperature remained stable within 20mK for days. The low helium consumption of the setup provided a hold time of 5 weeks of experiments with 60L.

3.2 Optical setups

3.2.1 Laser characterization

A short pulse distributed feedback laser (DFB) source from the company IdQuantique is used to perform the optoelectronic characterization of the SNSPDs (models id300-1310-DFB-TTL 50 Ω) [65]. The datasheet specifies a typical peak power of about 1 mW and pulse duration at FWHM of about 300ps.With an average power of -35 dBm at 1 MHz we can find the pulse energy and the mean number of photons per pulse. Knowing the spot size and the overlap area with device active region, one can estimate the attenuation required to enter a quantum regime.

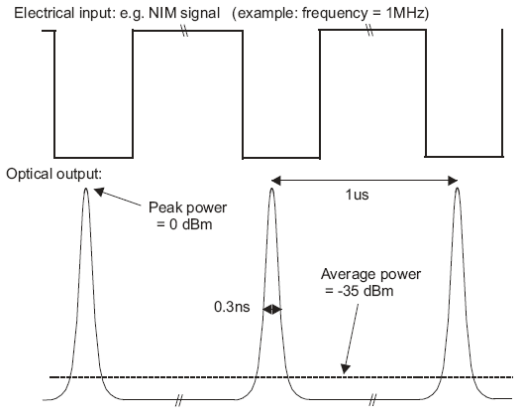

Figure 3-9 Characteristic of the pulsed laser id300 when triggered at a repetition rate R = 1 MHz [65]

$$Output\ Power = -35\ dBm = 10^{-3.5}\ mW \Rightarrow 10^{6}.E_{pulse} \tag{3.18}$$

$$\therefore\ E_{pulse} = \frac{10^{-3.5}}{10^{6}} = 10^{-9.5}\ mJ \tag{3.19}$$

We know that:

$$E_{photon} = \frac{h.c}{\lambda} \tag{3.20}$$

We use the Tektronix source generator , output A, square wave signal, 50 % duty cycle, 5 $V_{pk\text{-}pk}$, set to output to a 50 Ω load, the ID300-1310 nm (SN: 060019C020) and the EXFO power meter set on

1310 calibration to obtain the average power over a range of frequencies of interests as shown in Figure 3-10

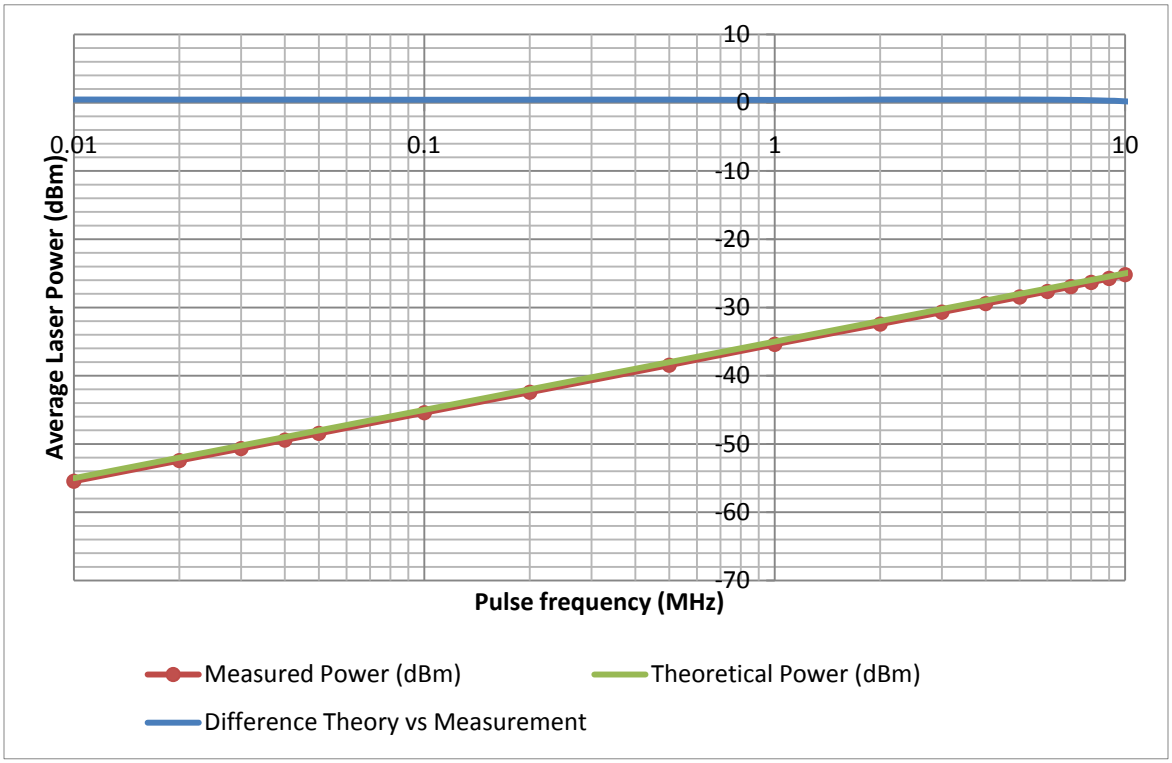

Figure 3-10 Measured and Theoretical power (dBm) of a 1310 nm pulsed laser are compared to insure proper agreement of the setup with theory and accuracy of the calibration procedures used in later experiments.

An almost constant difference of 0.45 dB is found between measurements and theory. This offset is principally due to loss at the connectors and due to the fact that the average output power is specified with a +/- 1 dB precision by the manufacturer.

Using a similar optical model as M.K. Akhlaghi in [66] presented in Figure 3-11, the average number of photons per pulse exciting the laser source can be expresses as:

$$\overline{N_1} = \frac{E_{pulse}}{E_{photon}} \tag{3.21}$$

For a wavelength of 1310 nm:

$$\overline{N_1} = \overline{N_1} \approx \frac{3.16227766.10^{-13}[\,J\,].1310.10^{-9}[\,m\,]}{6.62606896.10^{-34}\,[\,J.s\,].299792458[m.s^{-1}]} \tag{3.22}$$

$$\overline{N_1} \approx 2085425\ photons\ per\ pulse\ at\ \lambda = 1310\ nm \tag{3.23}$$

Similarly with the id300-1550@1MHz:

$$\overline{N_1} \approx 24467488\ photons\ per\ pulse\ \ at\ \lambda = 1550\ nm \tag{3.24}$$

The spectral width (FWHM) of those two modulated DFB lasers is specified as being typically 0.6 nm and we will therefore consider them as quasi-monochromatic coherent sources with central frequency $\overline{\upsilon}$ and all photons have approximately the same energy $h\overline{\upsilon}$ .The lasers are always operated after a warm-up period of 30 minutes or more throughout the rest of the experiments. Since temperature in the laboratory varies slightly during day and night operation, calibration of the average power was done before each experiment given a particular arrangement of optical fibers components.

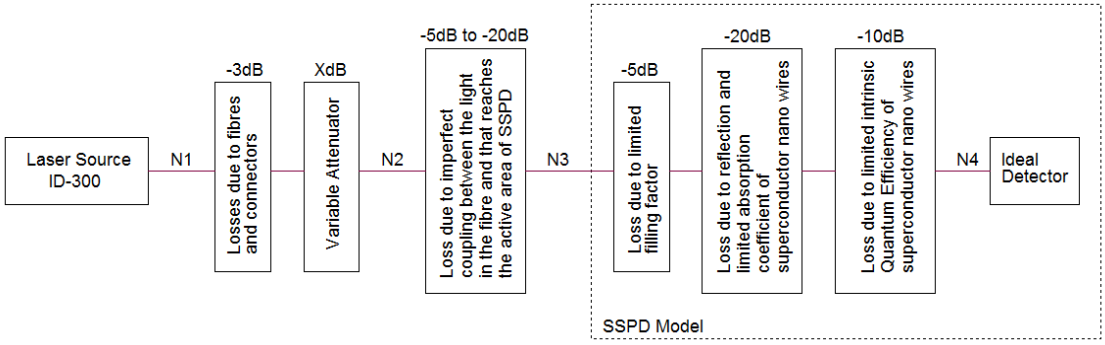

Figure 3-11 Conceptual optical model from M.K. Akhlaghi used in this work. The attenuation values indicated for the SNSPD model are only estimates and this aspect is not the object of the work presented in this report. The optical fiber polarization controller is not explicitly represented in this model but the loss inferred by its optical interconnects and fiber length is taken into account by the first block diagram for loss. [66]

Based on this model, two different measurable quantities can be defined.

$$System\ Quantum\ Efficiency:\ \ SQE = \frac{\overline{N_4}}{\overline{N_2}} \tag{3.25}$$

$$Quantum\ Efficiency:\ QE = \frac{\overline{N_4}}{\overline{N_3}} \tag{3.26}$$

In this report, the emphasis is placed on the system quantum efficiency measurements that benefits from a high coupling efficiency and a robust packaging approach, one of the objectives of this work. The QE curves were provided by the manufacturer for the devices tested.

3.2.2 Single-Photon generation and detection

As presented above, the mean number of photons per pulse is the only parameter one can control at the source, apart from the repetition rate. It is important to understand that the actual number of photons emitted will fluctuate from pulse to pulse and cannot be predicted. The statistical distribution of the number of photons is usually be described using the quantum theory of light and depends on the nature of the light source. In the case of coherent light, which is the assumption made in these experiments to approximate the pulsed laser, the arrival of photons can be regarded as the independent occurrences of a sequence of random events at a rate equal to the photon flux, which is proportional to the optical power. [18]

Considering the registration of photons to be statistically independent, the expression for the probability distribution $p(n)$ is derived below from the binomial distribution where $p(0)$ is the probability to detect zero photon, $p(1)$ the probability to detect one photon only, etc.

Let's consider a time interval T partitioned into a large number N of subintervals of duration $\frac{T}{N}$ so that each one of them carries one photon with probability $p = \frac{\overline{n}}{N}$, $\overline{n}$ the mean number of photon, and zero photon with probability $1 - p$.

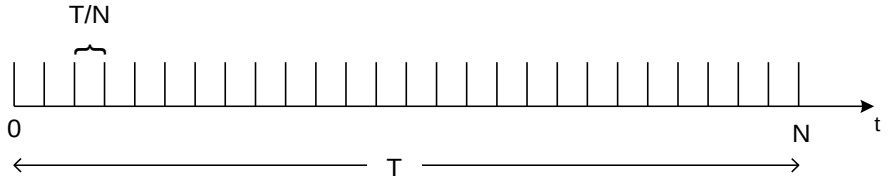

Figure 3-12 Representation of the partitioned time interval T used to derive the Poisson distribution.

The probability of finding n independant photons in the N subintervals is expressed as follow

$$p(n) = \frac{N!}{n!\,(N-n)!}\, p^n (1-p)^{N-n} \tag{3.27}$$

$$p(n) = \frac{N!}{n!\,(N-n)!} \left(\frac{\overline{n}}{N}\right)^n \left(1 - \frac{\overline{n}}{N}\right)^{N-n} \tag{3.28}$$

$$p(n) = \frac{N!}{N^n (N-n)!}\, \frac{\overline{n}^{\,n}}{n!} \left(1 - \frac{\overline{n}}{N}\right)^{N-n} \tag{3.29}$$

$$\lim_{N\to\infty} \frac{N!}{N^n(N-n)!} = 1 \tag{3.30}$$

$$\lim_{N\to\infty} \left(1 - \frac{\overline{n}}{N}\right)^{N-n} = e^{-\overline{n}} \tag{3.31}$$

$$\therefore\ p(n) = \frac{\overline{n}^n . e^{-\overline{n}}}{n!}, \qquad n = 0, 1, 2, 3, \ldots.. \tag{3.32}$$

which is the expression for the Poisson distribution, the probability of getting n successes when the average number of successes is $\overline{n}$.

When the laser power is attenuated to a level where there is less than one photon per pulse on average ($N < 1$), the degree of certainty that the SNSPD response was due to a single photon is high since the probability of a detection event due to a single photon is much higher than the probability of a detection event due to a pulse containing two photons as exemplified below [59]:

Considering $\overline{n}$ being small,

$$p(1) = \frac{\overline{n}^1 . e^{-\overline{n}}}{1!} \approx Np \tag{3.33}$$

$$p(2) = \frac{\overline{n}^2 . e^{-\overline{n}}}{2!} \approx \frac{(Np)^2}{2!} \tag{3.34}$$

$$p(3) = \frac{\overline{n}^2 . e^{-\overline{n}}}{2!} \approx \frac{(Np)^3}{3!} \tag{3.35}$$

$$\therefore p(1) \gg p(2) \gg p(3) \gg \cdots \tag{3.36}$$

If the average number of photon per pulse is set to be N = 1 and the detection efficiency of the device p = 1 % for example:

$$p(1) = 0.01 \gg p(2) = 0.00005 \gg p(3) = 0.00000016666\overline{6} \tag{3.37}$$

Section 4.2 of this report further exemplify this quantum regime of detection with experimental data.

3.2.3 Optical coupling

3.2.3.1 Theoretical model

Modeling the optical coupling of the light coming from a single mode optical fiber launched on top of the SNSPD's active area is important in order to understand the criticality of the alignment accuracy and estimate the misalignment tolerances that a system can accept while still maintaining a particular coupling factor. Full wave simulation has been performed by Z. Yan in [67] in order to simulate the absorption of a perfectly aligned Gaussian beam on the active area. Figure 3-13 shows a schematic model of an ideal Gaussian single mode laser shone onto the active area of an SNSPD. For this analysis we place a reference coordinate at the center of the active area and assume no tilt misalignment of the laser beam itself and adopt a model similar to W. Slysz [68].

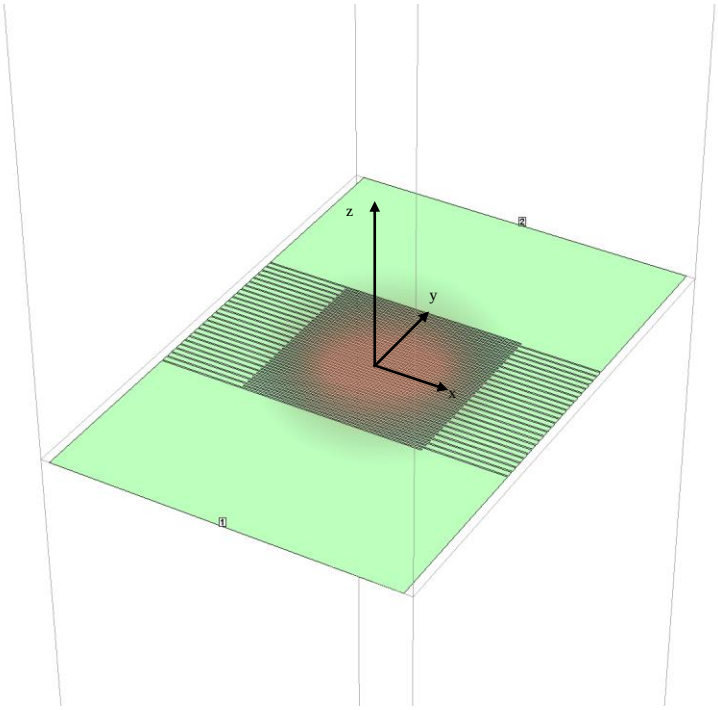

Figure 3-13 SNSPD schematic showing an ideal Gaussian mode laser shown onto the active area.

The optical fiber used is this setup is a Corning SMF28 with the following parameters extracted from the datasheet:

- Fiber core diameter = 8.3 µm
- Numerical Aperture (NA) = 0.13
- Mode Field Diameter (MFD) at λ = 1310 nm = 9.3 µm

- Mode Field Diameter (MFD) at λ = 1550 nm = 10.5 µm

Assuming an ideal Gaussian mode profile for this fiber we obtain:

$$P(r) = \frac{2}{\pi . \omega_0} . e^{\frac{-2(x^2+y^2)}{\omega_0}} \tag{3.38}$$

with ω_0 the beam radius at the beam waist.

Beam radius at distance z is given by:

$$\omega(z) = \omega_0 \sqrt{1 + \left(\frac{\lambda . z}{\pi . \omega_{0.}}\right)^2} \tag{3.39}$$

$$\omega(z)^2 = {\omega_0}^2 . \left(1 + \left(\frac{\lambda . z}{\pi . \omega_{0.}}\right)^2\right) \tag{3.40}$$

Mode profile at distance z from the fiber is given by:

$$P(r,z) = \frac{2}{\pi . \omega(z)^2} . e^{\frac{-2(x^2+y^2)}{\omega(z)^2}} \tag{3.41}$$

Let K be the fraction of power incident on the SNSPD with a square active area of side length a=10µm with perfect lateral alignment:

$$K = \frac{2}{\pi . \omega(z)^2} \iint_{-\frac{a}{2}}^{\frac{a}{2}} e^{\frac{-2(x^2+y^2)}{\omega(z)^2}} dx\, dy \tag{3.42}$$

Further simplifications lead to the following expression for the coupling factor plotted in Figure 3-14:

$$K = \frac{2}{\pi . {\omega_0}^2 . \left(1 + \left(\frac{\lambda . z}{\pi . \omega_{0.}}\right)^2\right)} \iint_{-\frac{a}{2}}^{\frac{a}{2}} e^{\frac{-2(x^2+y^2)}{{\omega_0}^2 . \left(1+\left(\frac{\lambda . z}{\pi . \omega_{0.}}\right)^2\right)}} dx\, dy \tag{3.43}$$

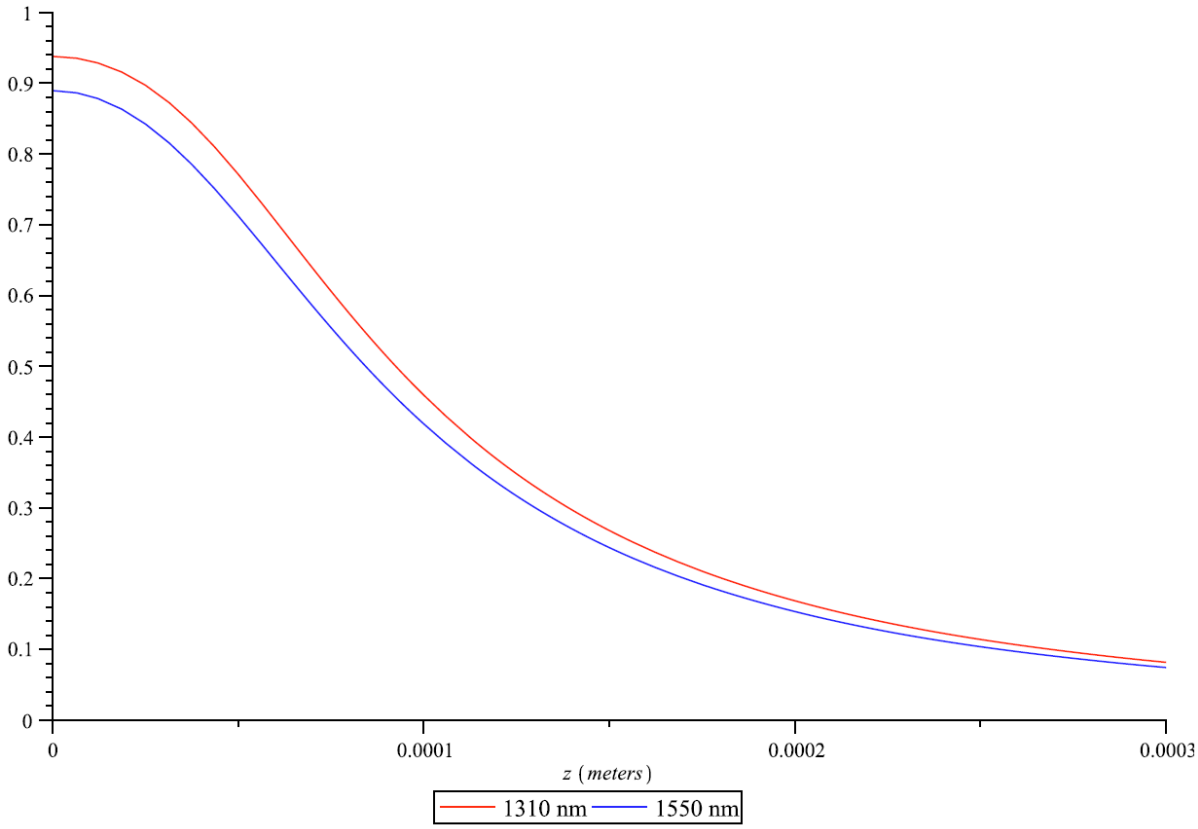

Figure 3-14 Coupling ratio (A.U) of incident power in a 10 µm x 10 µm area versus distance (meters) of fiber for λ = 1310 nm (red) and for λ = 1550 nm (blue) for a perfect alignment.

With the given geometry of the SNSPD, even contacting the face of the fiber to the active area will lead at best to a 0.9 coupling factor at 1550 nm. This model can help sizing the geometry of future SNSPD to be optimized for a particular wavelength.

If a lateral alignment is now considered the expression for the coupling factor can be written as follow:

$$K = \frac{2}{\pi.{\omega_0}^2.\left(1+\left(\frac{\lambda.z}{\pi.\omega_0.}\right)^2\right)} \iint_{-\frac{a}{2}}^{\frac{a}{2}} e^{\frac{-2\left((x-\delta_x)^2+\left(y-\delta_y\right)^2\right)}{{\omega_0}^2.\left(1+\left(\frac{\lambda.z}{\pi.\omega_0.}\right)^2\right)}} dx\,dy \qquad (3.44)$$

Figure 3-15 plots the coupling factor K for a wavelength of 1310 nm for various lateral misalignments. A 4 µm lateral offset on either x or y axis leads to a greatly reduced coupling factor.

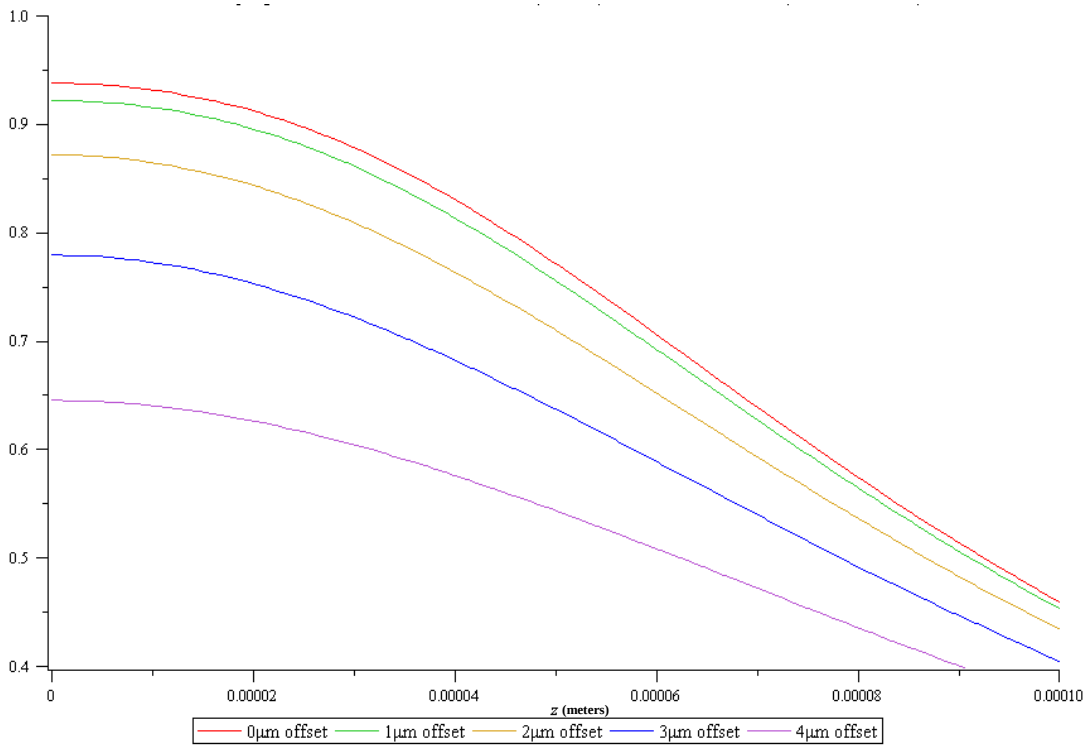

Figure 3-15 Coupling ratio (A.U) of incident power in a 10 µm x 10 µm area versus distance (meters) of fiber for λ = 1310 nm with lateral offset.

If misalignment occurs on both x and y axis the overlap of the Gaussian and the square active area will be further reduced and will lead to a poor performance of the whole system, namely a reduced SQE. Figure 3-16 present in another form how the coupling ratio suffers from lateral misalignment at 1310 nm.

This analysis presents one of the most challenging factors affecting the operation of SNSPD in an embedded system, out of a laboratory, in the field. Optical coupling stability and vibration resistance are some of the challenges that need to be addressed. Being able to embed an optical waveguide around the SNSPD and use common industrial methods used for butterfly laser packages would be a real advantage. However, those modules are rarely meant to operate in such a wide temperature range and always come with their embedded temperature controller and heat sink for coupling stability. Another more costly alternative is to use actively controlled nanopositioners to adjust the position of

the optical fiber. Feedback is provided by the device as the count rate would be maximum when properly aligned.

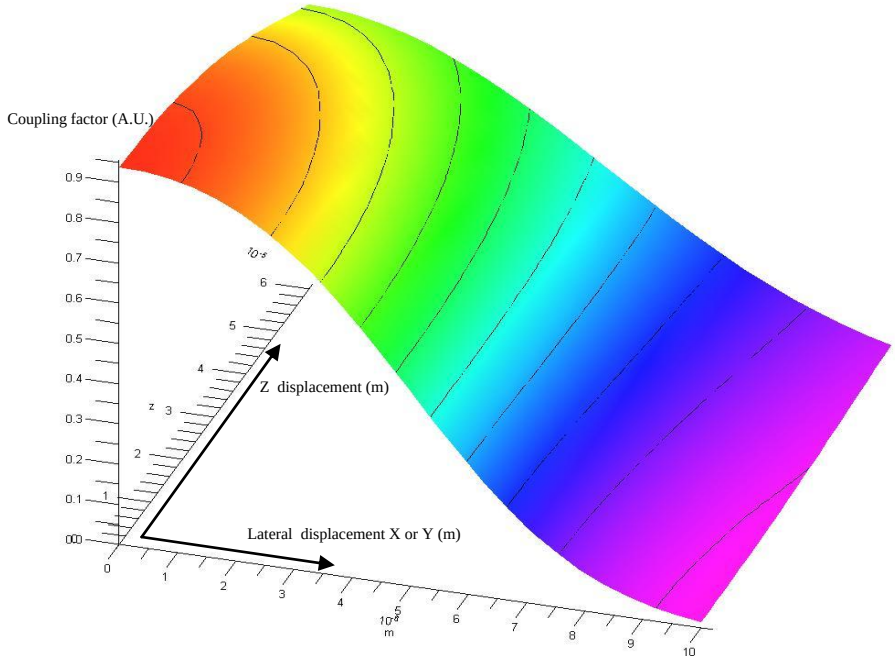

Figure 3-16 Contour plot of the coupling ratios (A.U) of incident power in a 10 µm x 10 µm area versus distance of fiber for λ = 1310 nm (red) with lateral offset.

The use of invar and the proper design of a symmetric structure to minimize the effects of thermal contraction allowed operation of SNSPDs for multiple weeks with no measurable variations after various thermal cycles.

3.2.3.2 Optical fiber alignment setup and procedure

The packaging is attached to a X-Y-Z manual stage with fine micrometers and the bottom of the SNSPD is observed through the alignment hole with an optical setup (Figure 3-17) composed of an infrared coated 10x microscope objective and a 75 cm focal distance lens, along with a black and white analog camera for which the infrared filter has been removed (the optical path also uses a 45 º mirror). White light or 1310 nm light from an LED (Marubeni Corp. part: SMT1300) can then be shined from the top, and since the optical fiber ferrule is made of borosilicate glass, the back illumination is also conserved while the cover is placed on the packaging. Figure 3-18 is a screenshot of the real-time video stream during an alignment where the inset shows the case where a 1310 nm laser is shined at the other end of the single-mode 1.5 m fiber.

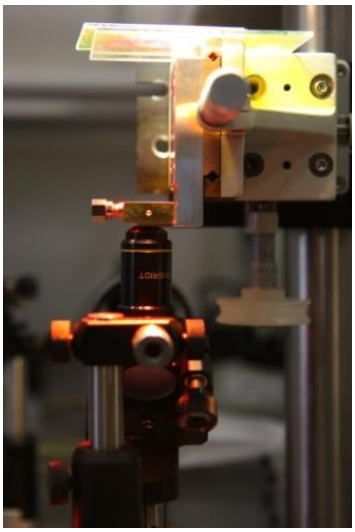

Figure 3-17 Opened SNSPD package held on a XYZ micromanipulator on top of a x10 microscope objective aligned under the observation holes in order to observe the active area and align the cover with the optical fiber ferrule.

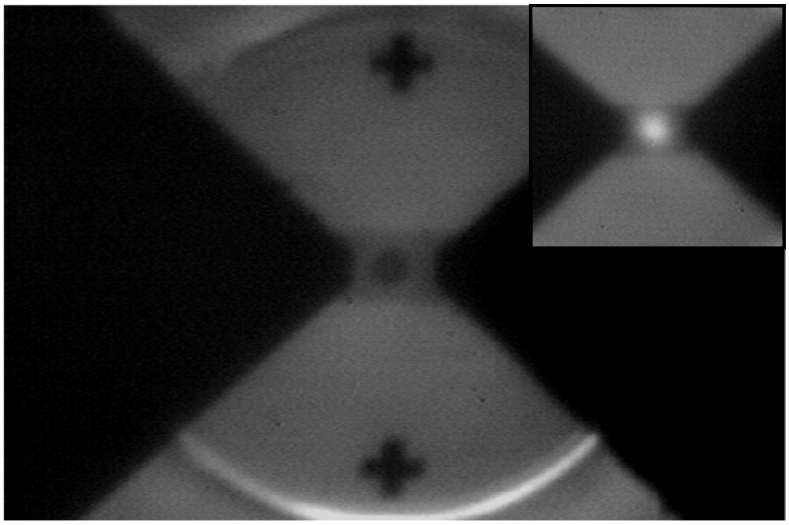

Figure 3-18 Screen capture of the video stream while observing the device from below while aligning the optical fiber core (black dot in the center due to different numerical aperture of the core) on top of the active area. The inset shows the case where a 1310 nm laser is shined in the fiber. The height of the field of view is 125 µm. and the two black triangles are the tapered gold contact. The shaded rectangle area in the center is the NbN patch (about 20 µm x30 µm)

It is interesting to notice in Figure 3-19 the relative variation of shades of the active area and the unpatterned film corresponding to a 0.6 filling factor. A more detailed analysis using a calibrated

camera and source could reveal the transmittance of the 4 nm NbN film. However this image was acquired using incoherent white light with an analog camera.

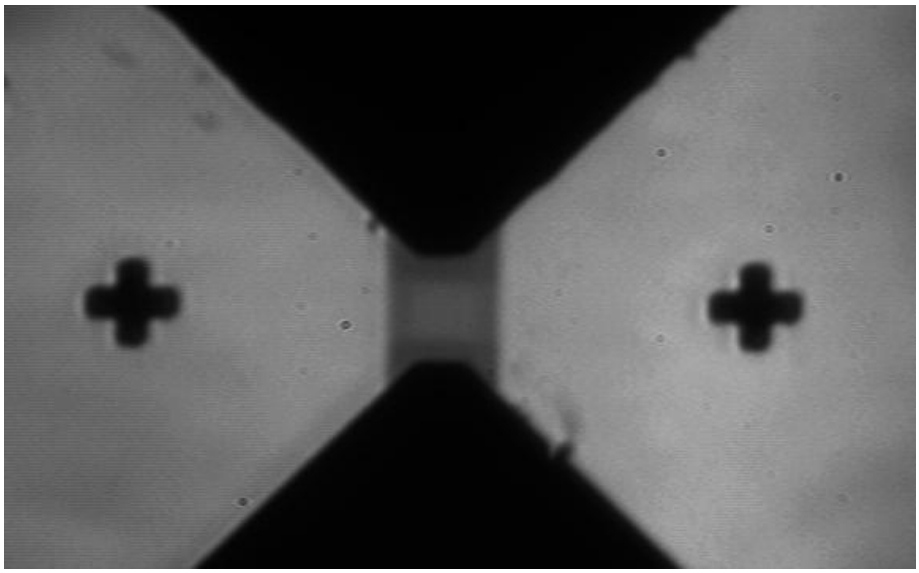

Figure 3-19 Device active area observed with the built optical magnification system showing clearly the alignment marks used during the fabrication process the NbN patch in the center for which can be perceived the relative variation of shades for the patterned structure with a filling factor of 60 %.

The SEM image of the device depicted in Figure 2-3 serves as a reference for the precise location of the approximately 10 µm x 10 µm meander structure. We carefully adjust the height of the fiber until the device's focal plane and the ferrule's plane both come into focus. One can also estimate the distance between the two by reading the relative displacement on the Z-axis micrometer while focusing on one or the other. The lateral displacement is done by hand while the cover screws are in place but not tightened. After a few alignments we discovered that we could safely lower the ferrule until contacting the device since the gold pads are much thicker than the 4 nm to 5 nm thick NbN film. The locking ring and cover screws were then tightened and the device package was mounted in the dipper probe tight enclosure.

Gluing a fiber ferrule directly onto the SNSPD using UV curing adhesive compatible with operation down to 77 K (NOA61) was considered to avoid any further alignment after the first one and tests were made on glass slides and cooled down successfully. However, as only two working devices were available for this work, the risk of damaging one was not taken.

In order to facilitate the manual alignment procedure, a piece of software was developed with LabVIEW ® to reconstruct an imaginary 3D map of the SNSPD using the grayscale video flux from the camera during observation as shown in Figure 3-20. Like in Figure 3-18, the black dot in the center is the unilluminated silica core of the SMF fiber placed on top of the active area.

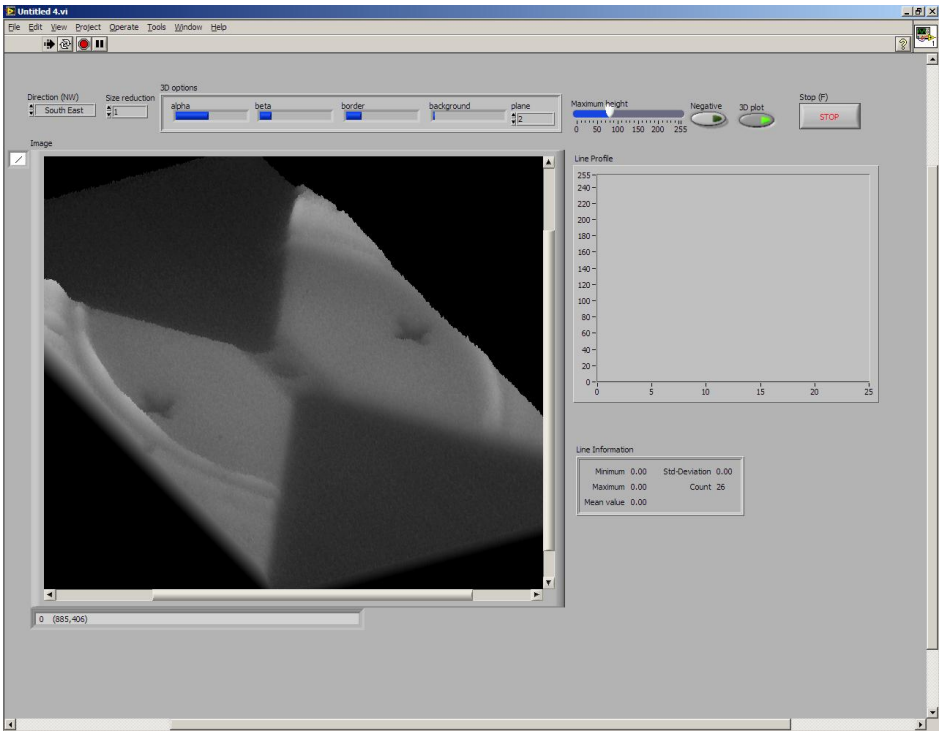

Figure 3-20 Screen capture of a NI LabVIEW ® VI developed to observe in real-time the optical alignment. A Sequence of filters is applied on the video stream in order to plot in reconstructed 3D the image using the image shades for the volume information. Image can be rotated in all axes and a profile cut view can be plotted on the right from any location in the image to observe the step in height produced by the laser spot versus the NbN film reference level.

Overall this passive alignment approach proved to be successful and cost effective compared to system with nanopositioners but those prototypes could be further improved using precision industrial machining method.

3.3 Electrical Setup and DC measurements

Detecting single photons requires of course a system that is as noise free as possible. The electromagnetic radiation being reduced to a minimum with the design of a proper cryostat and packaging as described before allowing minimization of this contribution to levels where the

blackbody radiation emitted by surfaces at 4.2 K surrounding the device is predominant. Infrared photons emitted and guided within the "hot" optical fibers for which a large portion resides at room temperature contribute to the background noise as well but can be minimized using filters. The electrical noise from the measurement apparatus connected to the device must be minimized in order to operate the SNSPD at higher critical current ratio where the quantum efficiency is expected to be higher. Proper grounding techniques should be applied to the system and ground loops eliminated. The DC manganin leads for the thermal sensors running down the dipper probe were properly twisted in pairs and filtered with RF chokes with high impedance to minimize noise propagating down to the device enclosure. All the instrumentation presented in Figure 3-26 was properly grounded to one single power outlet. The microwave amplifier was powered from a 12 V lead acid battery. The SNSPD was DC biased through a bias tee (see Figure 2-15 for biasing circuit) with either a Keithley ® sourcemeter unit or the DC source which schematic is presented in Figure 3-21.

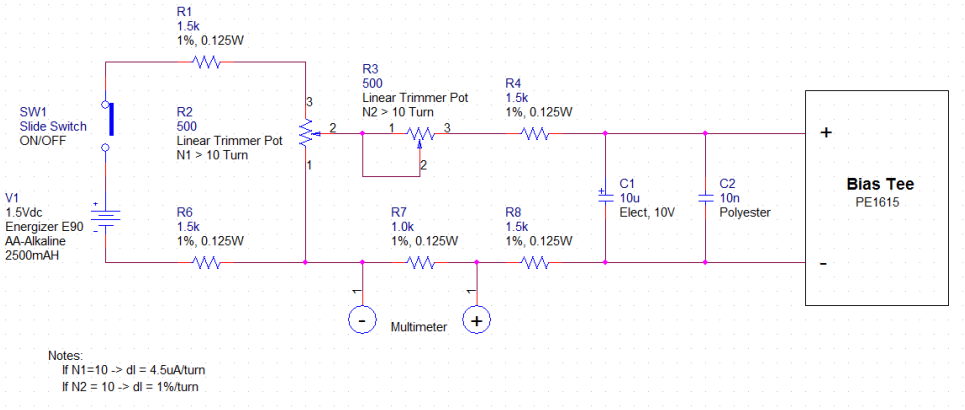

Figure 3-21 Electrical schematic of the battery powered DC source designed by M.K. Akhlaghi in [66] and implemented for this work. The 1.5 V alkaline battery was replaced by a lithium one due to its exceptional longevity and temperature stability (3000 mAh, Energizer ® L91-BP2).

The 110 V / 60 Hz powered sourcemeter unit (model Keithley ® 2400) used to perform the I-V sweeps presented in Figure 3-22 and Figure 3-23 added high frequency noise to the system which effectively reduce the critical current measured in this way and increased the dark- counts of the device when not exposed to any light pulses. The 1.5 V lithium battery powered current source showed to be very effective at operating the SNSPs thanks to the virtually electrical noise free source provided by the internal chemical reaction in such battery. Temperature dependency of the source was minimized by the use of high quality / low temperature drift discrete components. This source allowed operating the superconducting nanowire at 99 % of its critical current for unlimited amount of times without any spurious switch to a normal state resistor like it was observed with the

sourcemeter where the smallest amount of noise can overshoot the current ratio. Once I_c is reached the device locks itself in a mode where Joule heating keeps it in a normal state.

3.3.1 IV-measurements

Voltage or current sweeps were performed on all the devices. Figure 3-22 graphs the current measured while the sourcemeter sweeps the voltage from 0 V to a few millivolts for a particular device. A superconductor is expected to show no DC resistance to the flow of current (for $I < I_c$) however a resistive load line of 0.1 Ω is observed until I_c is reached. This is most likely due to the internal resistance of the voltage source and the DC resistance of the interconnection between the SMA RF cables, bias tee, device packaging and sliver epoxy wire bonds to the device. Once I_c is reached the device partially switch back to normal state (hot spots plateau).

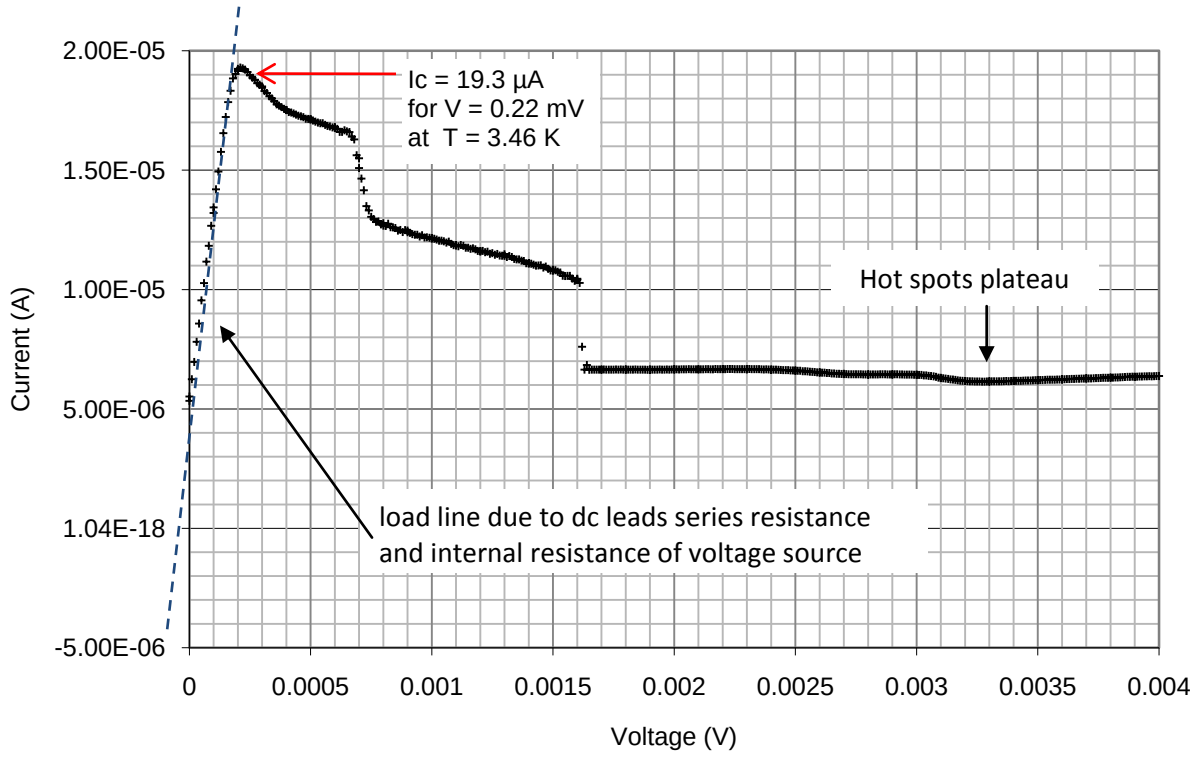

Figure 3-22 DC characterization of a SNSPD showing a critical current Ic = 19.3 µA a T ≈ 3.46 K

The voltage sweeps can be extended to a few volts until the entire device (all the individual nano-stripes) switches back to normal state due segment after segment to the self heating effect when the current ($I > I_c$) is high as shown in Figure 3-23. The maximum resistance measured with such high

voltage bias is similar to the normal state resistance measured at around 15 K from the resistance versus temperature curve before the resistance abruptly goes down below T_c.

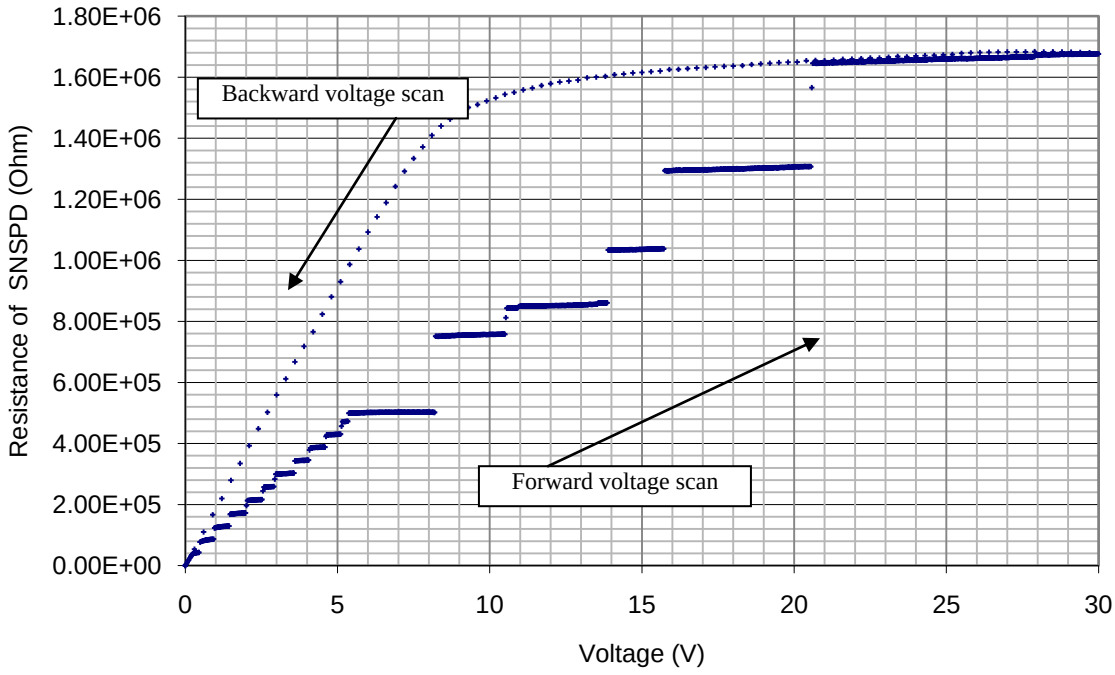

Figure 3-23 Resistance of a SNSPD versus bias voltage. A hysteresis is observed in the IV curve comparing the forward and backward scan as the device is maintained in a normal state due to joule heating in the nanowire segments of the NbN thin film.

The backward voltage scan started from the normal state reveal a hysteresis in the voltage resistance curve due to the fact that the device is kept in this normal state until the current falls below I_c. For the rest of this work, only the battery powered DC source was used for I_c determination, dark-count and optoelectronic characterization.

3.3.2 Temperature dependence of the critical current

Recalling the expression of the magnetic penetration depth of a superconductor (also called London penetration depth) at 0 Kelvin:

$$\lambda(0) = \sqrt{\frac{m^*}{\mu_0 . n^* . e^2}} \tag{3.45}$$

And its temperature dependency with respect to the critical temperature T_c of the superconductor:

$$\lambda(T) = \frac{\lambda(0)}{\sqrt{1 - \left(\frac{T}{T_c}\right)^4}} \tag{3.46}$$

Using the following critical magnetic field temperature dependency expression:

$$B_c(T) = B_c(0).\left[1 - \left(\frac{T}{T_c}\right)^2\right] \tag{3.47}$$

The temperature dependency of the critical current density of a superconductor can be expressed as follow:

$$J_c(T) = \frac{B_c(T)}{\mu_0.\lambda(T)} \tag{3.48}$$

$$J_c(T) = J_c(0).\left(1 - \left(\frac{T}{T_c}\right)^2\right).\left(\sqrt{1 - \left(\frac{T}{T_c}\right)^4}\right) \tag{3.49}$$

Using experimental data from device 2 obtained after the temperatures had stabilized at a plateau above the liquid phase of helium, the following temperature dependence of Ic was obtained. The theoretical model derived from the above equations for Ic is plotted using Ic(0) = 34.22869 µA (fitting parameter) and 9 K as the critical temperature T_c (measured from Figure 3-8) in Figure 3-24.

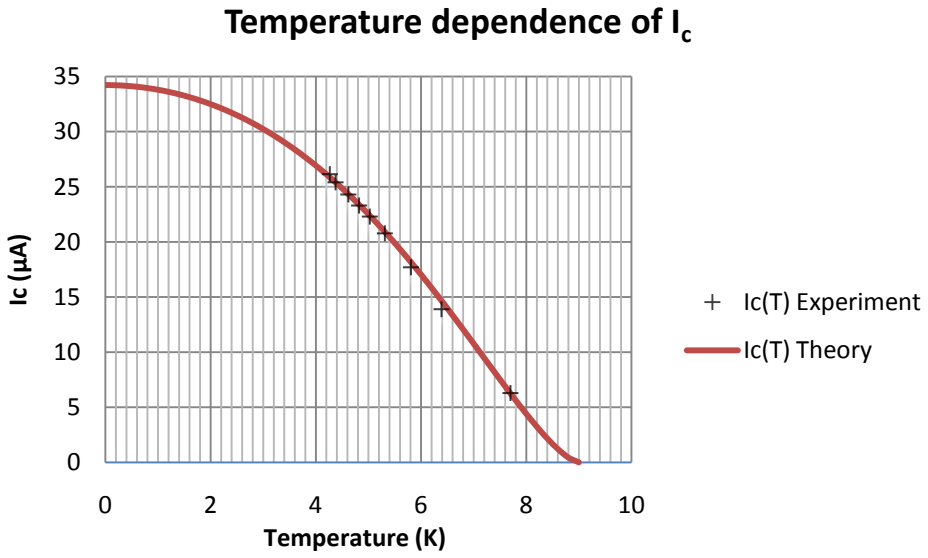

Figure 3-24 Temperature dependency of the critical current for device 2. In red the theoretical model for the temperature dependent critical current. Crosses represent experimental data for device 2.

Good agreement between the model and the experimental measurements is observed for this superconducting thin film. If the device was operated at 2 K, the critical current of device 2 would be increased from about 27 µA to 33 µA. It is expected that the quantum efficiency of the device would scale up as well. However lowering the temperature of the liquid helium bath to this temperature would require pumping on it which would increase the consumption rate to a few liters per hour. The system developed in this work does not allow this mode of operation but could me modified in the future for this purpose. Operation of SNSPD at this temperature in a cryogen free system would provide a better approach to increase the device's performance and operate it on the long term, as the initial cost of such system will be recovered considering the always increasing price and scarcity of liquid helium.

3.4 Overall setup, LabVIEW ® control, automation

Figure 3-26 presents a typical experimental setup developed in this project with all the measurements apparatus fitting in a standard rack. The amplified microwave pulses generated by the SNSPD were sent to the oscilloscope, the photon counter SR400, or both at the same time using a microwave power splitter. Various LabVIEW ® virtual instrumentations environments were developed to perform DC analysis and optoelectronic characterizations. Figure 3-27 presents an automated scan of the pulse counts versus the discriminator level of the electrical pulses photon counter for a given bias current. This allowed finding the optimum threshold level in order to capture all the counts and avoid missing the pulses which peak amplitude might have been modulated with the added noise from the amplifier, had the discriminator been set too high.

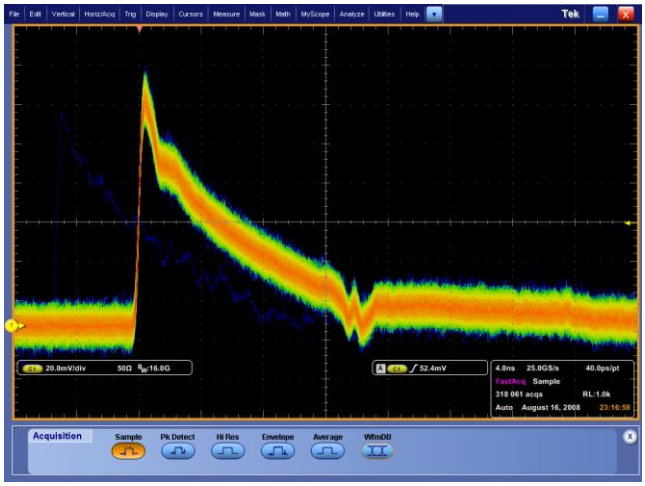

Figure 3-25 SNSPD pulse with persistence display revealing the noise amplitude due to the amplifier.

The width of the falling step gives us an idea of the statistical distribution of the voltage pulses' peak. It would be interesting to modify the setup in the future to use a low noise cryogenic amplifier placed in the liquid helium as well. Measuring the statistical distribution of the pulses peak voltage in this system might reveal part of the internal mechanism and quantum fluctuations that lead to the formation of the so called hot spots on the nanowire.

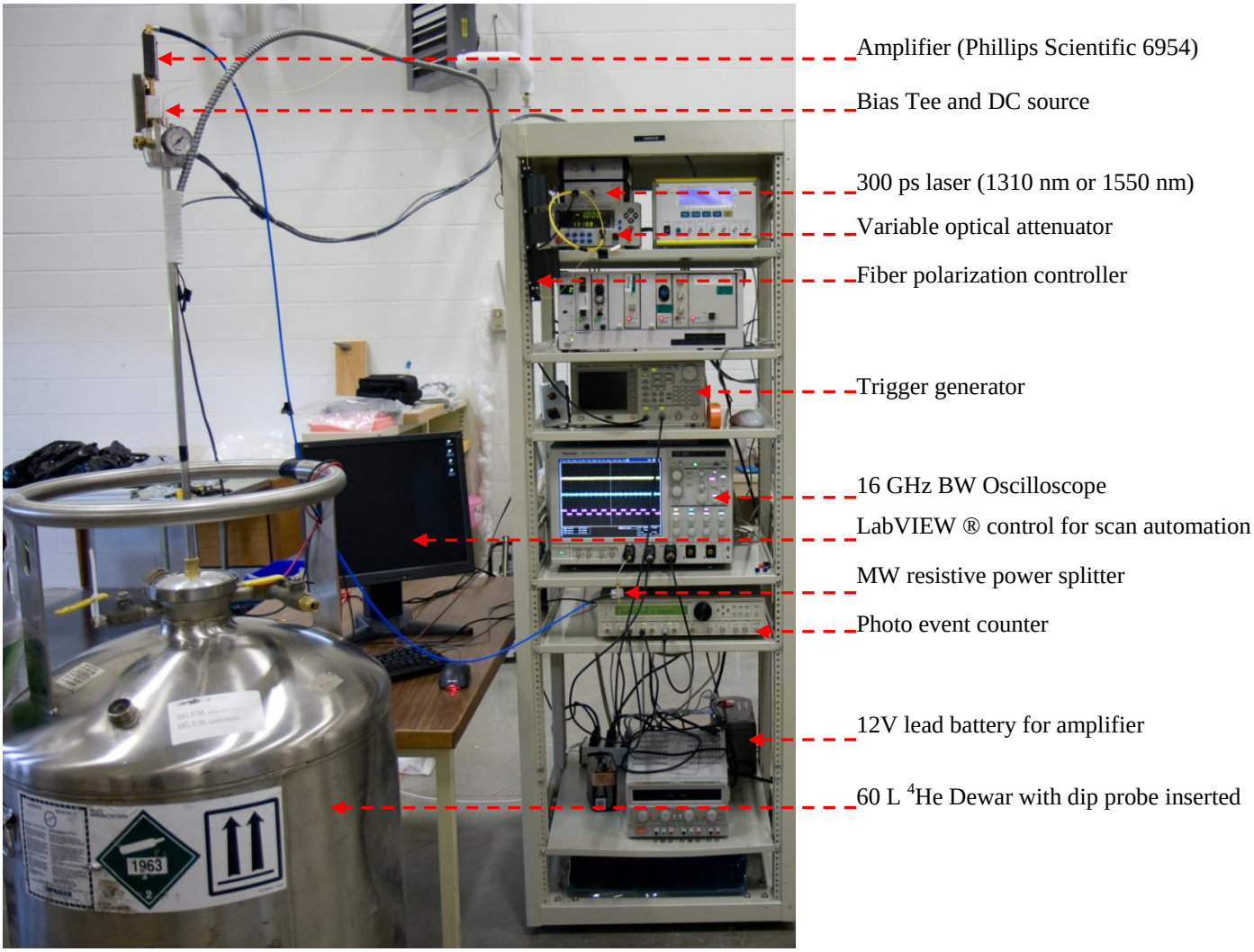

Figure 3-26 Picture of the overall setup developed in this work used to characterize SNSPD at IQOL. All the instrumentation hold in one rack and the device and dipper probe are inserted into a commercial 60L liquid helium Dewar.

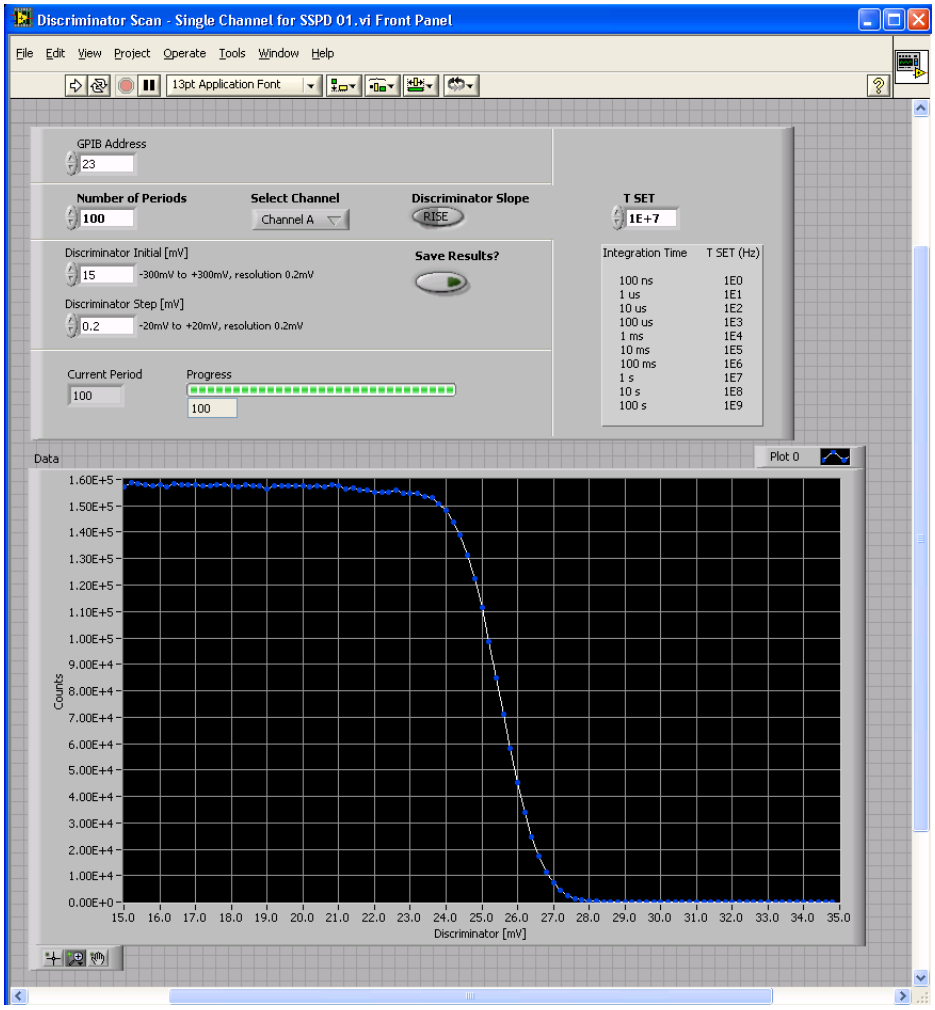

Figure 3-27 Screen capture of a NI LabVIEW ® VI developed to automatically scan the level of the discriminator of the Stanford Research photon counter SR400 before performing the optoelectronic characterization. The curve represents the number of counts versus the internal discriminator level of the counter.

Using this previously describe scan, the discriminator level is properly adjusted is the subsequent LabVIEW ® VI that perform the optical input scans as presented in chapter 4.

Chapter 4 Optoelectronic characterization

Two devices were packaged, aligned and tested in the same way using the experimental setup developed and presented previously. After the temperature had reached a stable level and transition to superconducting state was observed, a DC characterization was performed in order to identify the critical current at the lowest temperature achievable in the setup which is the liquid helium temperature at atmospheric pressure. The optical input connecting on the top fiber adaptor of the dipper probe was characterized with a calibrated power meter and an estimated loss of 0.3 dB was attributed to the extra fiber to fiber connection. The following presents some initial tests that revealed a flaw in the design related which was then corrected and the optoelectronic characterization at telecommunication wavelengths from which the system quantum efficiency of the devices can be extracted. Finally some initial speed and jitter measurements are performed on one device at a wavelength of 800 nm.

4.1 Light condition, yellow fibers, black fibers, dark-counts.

Figure 4-1 presents some initial scans performed with the automated virtual instrumentations setups developed for different light environment. The output of the laser was attenuated in 1 dB steps from -100 dB to 0 dB while being triggered at 1 MHz. The sampling period was set to 1 second in the three cases and data was averaged over multiple acquisitions for each point. All the optical fibers used up to now are the standard 900 µm or 3mm diameter yellow plastic jacketed SMF28 fibers with FC/PC connectors. We hypothesize from the number of counts measured with high optical attenuation for the background light conditions that somehow lights from the fluorescent tubes on the ceiling in the lab or daylight must leak into the fiber and is guided to the SNSPD.

In order to verify this possibility, a light tight enclosure was built with an aluminum frame and black cloth around the liquid helium Dewar and optical equipments. The level of dark-counts for the same bias current was even lower than the no light evening condition, for which there were still some emergency lights present far away from the setup and the light from the LCD screen and front panel of the instruments showed in Figure 3-26. The front panels of the instruments placed under the light tight enclosure were covered with black masking tape. Further verification of this issue was accomplished by gradually exposing 5 meters of yellow jacketed fiber to the light of the environment while observing the dark-count increase as well.

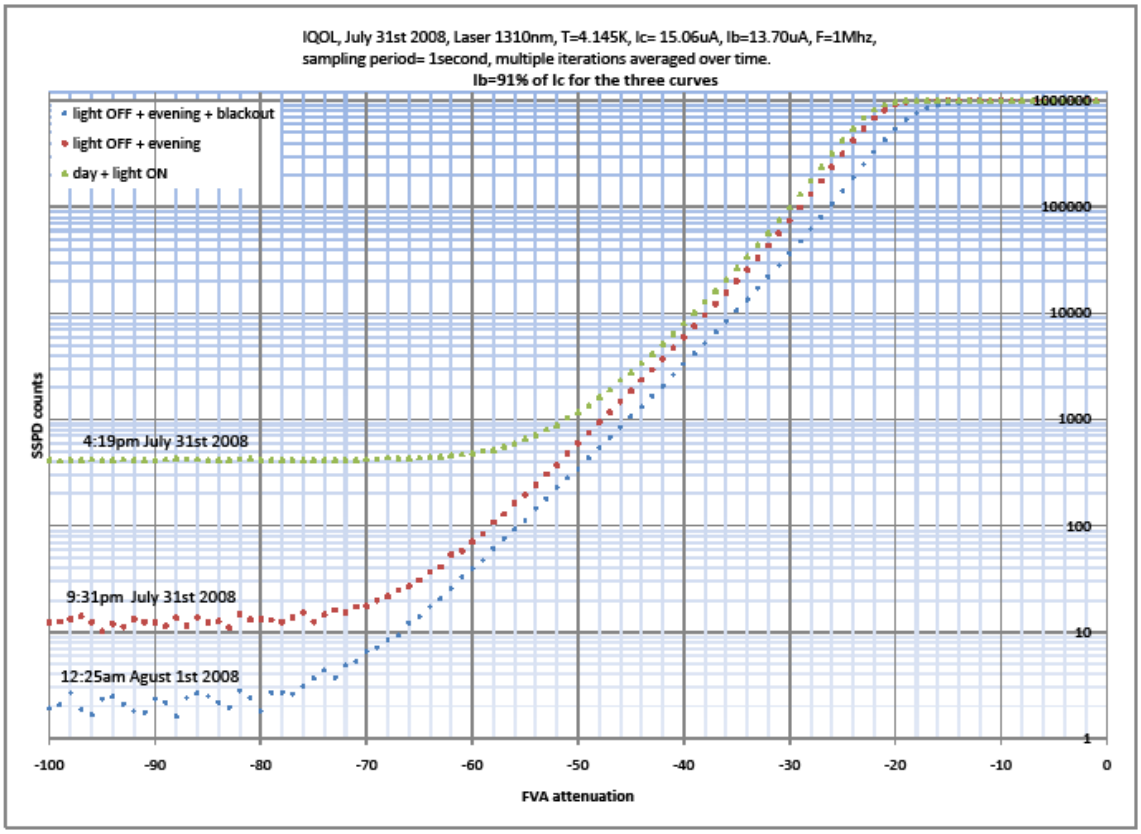

Figure 4-1 Photon counts versus optical fiber attenuator attenuation in dB for three light condition using yellow jacketed corning SMF28 optical fibers. The ceiling lights were either on or off. The natural light from outside was either present or dimmed at night. A blackout enclosure was surrounding the fibers for the measurements on August 1st 2008. From -60 dB to 0, the photo events curves are slightly offset compared to each others as the fiber had been moved affecting the polarization hence the quantum efficiency of the device.

To remedy to this problem, some customized black jacketed optical fibers were ordered from OM-6 Technologies and all the yellow fibers were replaced in the setup. The subsequent scans performed with those fibers gave low levels of dark-counts, similar to using the black enclosure, in any light condition.

In order to characterize the temperature stability at the device level and its current source, some long scans were performed on device 2 with no optical input with a time window of 15 min per point for a duration of 18 hours, as presented in Figure 4-2. It is important to note that the device was inserted in the liquid helium from a height in the Dewar where the temperature was about 60 K at time 22:00 and that the DC bias was slightly readjusted 40min later. A slight decrease in the dark-

counts is observed from 11:00 pm to 4:00 pm the next day which can be attributed to the slow temperature stabilization of the stainless steel structure, overall packaging and cable system.

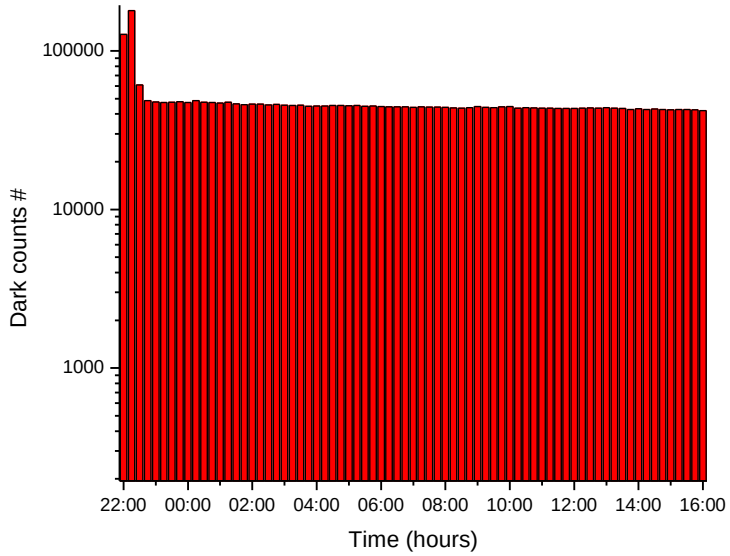

Figure 4-2 18 hours measurements of the dark-counts for device 2. The current source was slightly adjusted at the beginning of this test and was measured to be constant from 11:00 pm to 4:00 pm the day after. We note a slight decrease of the counts due to the very slow thermal stabilization after the dipper probe was inserted in the liquid helium from a 60 K state at the beginning of the test. Fiber input was blocked at all time with a metal cap.

Indeed, the current source was measured a different intervals and found to be constant, within the measurement accuracy of the voltmeter used (Fluke 189: 500 µA range, 0.01 µA resolution, 0.25 % DC accuracy). Stability of the temperature (after a certain period of time), stability of the current source (after some minutes after having rotated one of the adjusting potentiometers) and stability of the calibrated laser input to the device (after some warm-up period) was asserted and the optoelectronic characterization of the SSPDs was then performed as presented in the following sections.

4.2 Optical scans at 1310 nm and device System Quantum Efficiency (SQE) extraction

Before presenting the results obtained it is necessary to understand the expected relationship between the laser power, the count rate of a true single-photon detector and the average number of photon per pulse N. Using the parameters introduced in section 3.2.2 the following can be derived:

$$count\ rate = p(n).R \tag{4.1}$$

$$laser\ power = N.R.E_{photon} \tag{4.2}$$

When the count rate is plotted on a log scale versus the laser power in dB we can express the above equations as follow [59]:

$$log\ (count\ rate) = log(p(n).R)) \tag{4.3}$$

$$log\ (count\ rate) = log(p(n)) + log(R) \tag{4.4}$$

$$log\ (count\ rate) = log(Np) + log(R) \tag{4.5}$$

$$log(count\ rate) = log(N) + log(p) + log(R) \tag{4.6}$$

$$\therefore \boldsymbol{log(count\ rate) = log(N) + constante} \tag{4.7}$$

$$log(laser\ power) = log(N.R.E_{photon}) \tag{4.8}$$

$$log(laser\ power) = log(N) + log(R) + log(E_{photon}) \tag{4.9}$$

$$\therefore \boldsymbol{log(laser\ power) = log(N) + constante} \tag{4.10}$$

Both entities are linearly related to the logarithm of the average number of photons per pulse N, plus some constant related to the quantum efficiency of the device and the repetition rate of the laser pulses. If the laser is prepared to contain less than 1 photon per pulse on average as presented in chapter 3.2.2, the count rate plotted versus the laser power (in our case the attenuation added to a fixed average laser power) will be linearly related as well with a slope of unity.

Figure 4-3 and Figure 4-4 present the set of scans that were performed for a wavelength of 1310 nm for device 1 and 2 respectively. Each set of points is a scan performed at a particular bias ratio at 4.2 K after proper alignment. The fluctuations observed in counts when the laser attenuation is high are due to the fact that there were fewer counts averaged in those low regimes, for the time windows used. Increasing this time window to many minutes or hours would have provided a better statistics but showed to be impractical at this stage as a single bias ratio curve already took on average 45 minutes to 1 hour. This variation in time is due to the fact that some simple algorithm was developed in the automation software to adapt the number of measurements to take per attenuation point depending on the count rate. Indeed, with count rates in the 10^4 to 10^6 range, less data is necessary to obtain a good fidelity.

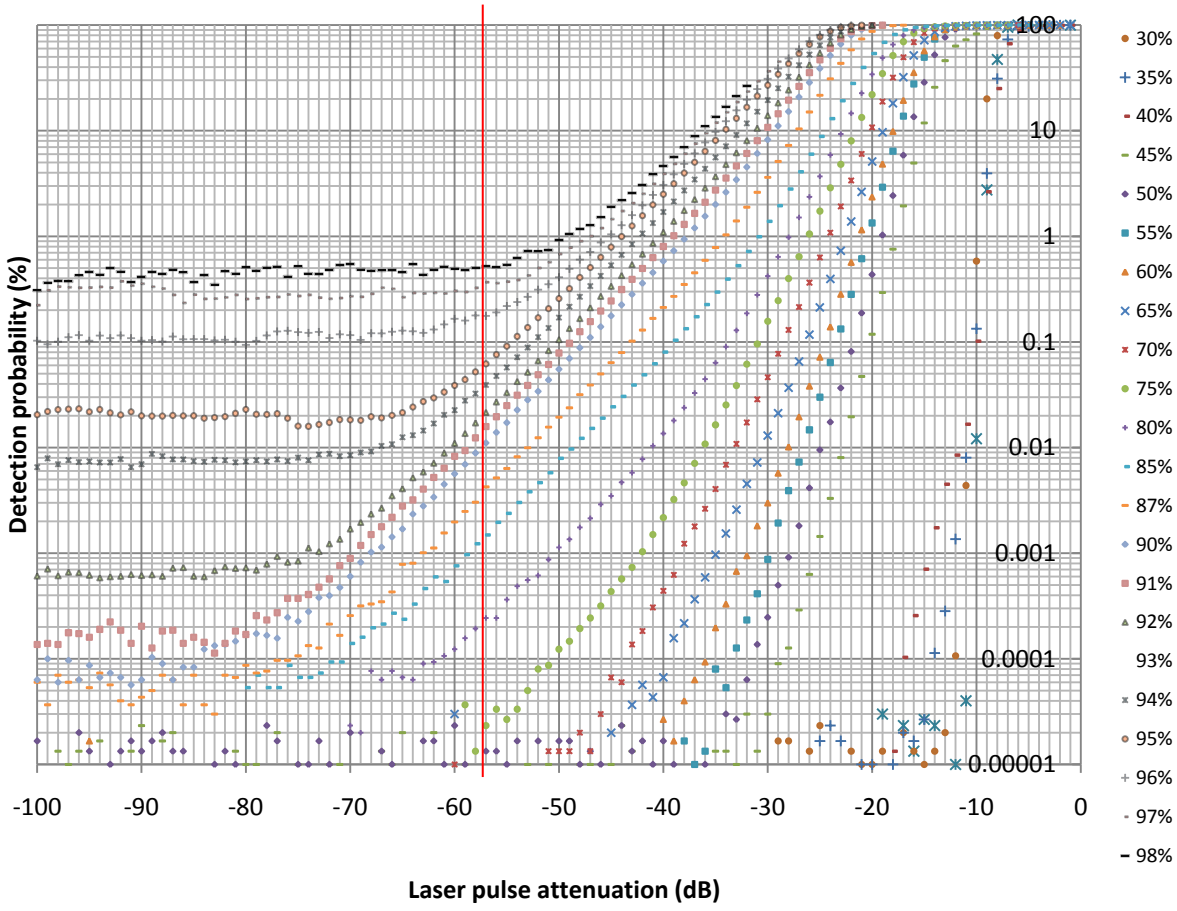

Figure 4-3 Detection probability as a function of laser pulse attenuation for device 1 for various bias current ratios (Ic = 15.06 µA, Temperature = 4.2 K, wavelength = 1310 nm, repetition rate = 1 MHz). Pulses contain 1 photon on average when attenuation is set at -57.4 dB (red vertical bar), polarization optimized for maximum count.

It is interesting to observe on Figure 4-4 that the device showed photo response even when biased at a very low level (4 to 5 µA). Pulses contain one or less photon per pulse below an attenuation of 57.4 dB. At a bias ratio of 98 % for example, no noticeable change can be observed as the dark-counts are already at a high level. The graphs plot the detection probability which is identical to the count rate introduced here after scaling with respect to the number of pulses per second and expressed as a percentage. Figure 4-4 shows the results of the characterization of device 2 for various bias current ratios. Similar to device 1, the detection probability increases when the bias current is closer to I_c at the cost of an increased dark-count rate as shown by the horizontal asymptotes on the 95 %, 90 % and 82 % curves. The 99 % bias ratio data was interrupted when attenuation reached -37 dB and the SNSPD latched into normal state. Also, for the high bias ratios and for attenuation smaller than

40 dB the number of counts exceeds the number of optical pulses. Indeed the photon counter registers all the detected optical pulses in addition to the dark-count events occurring randomly in between the laser triggers. Time domain traces acquired at high optical power and high current showed that the SNSPD can sometimes emit a train of two or three pulses in response to a single optical pulse.

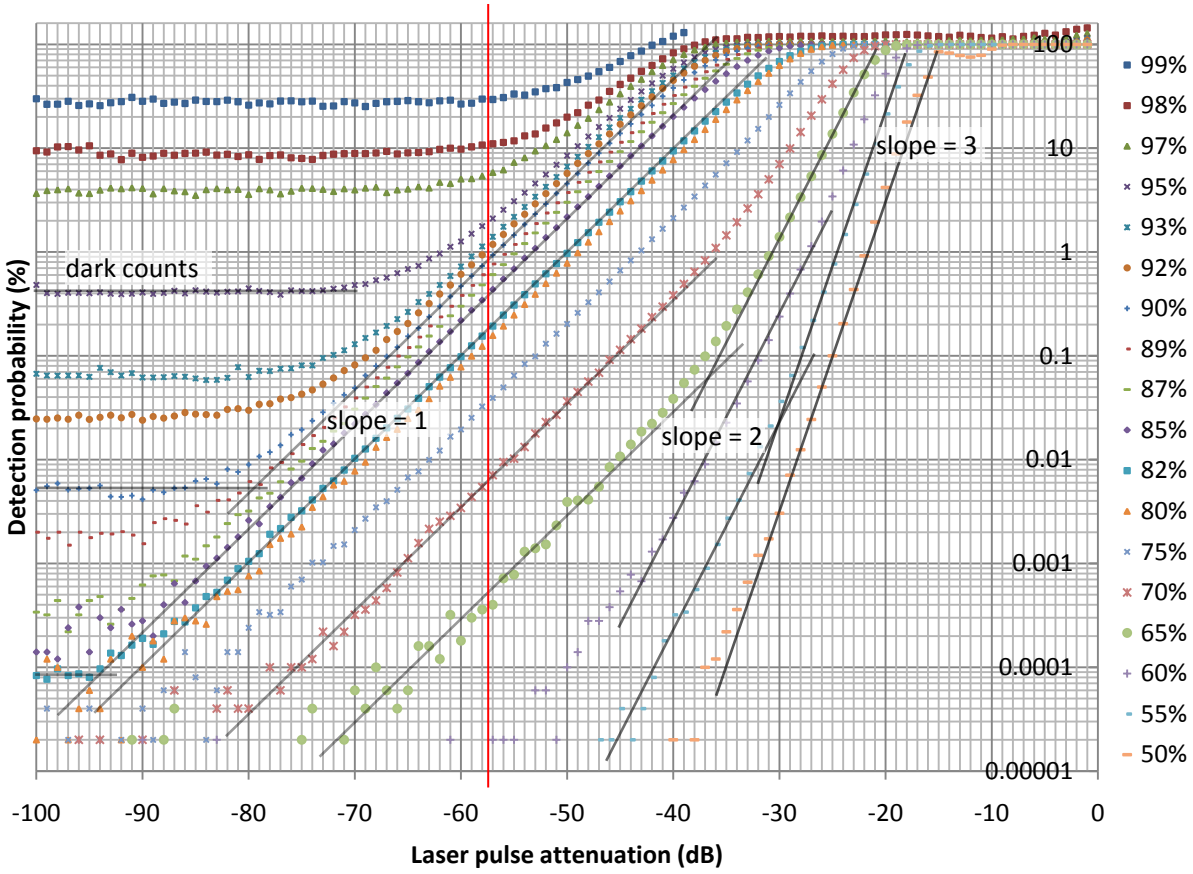

Figure 4-4 Detection probability as a function of laser pulse attenuation for device 2 for various bias current ratios (Ic = 27 µA, Temperature = 4.2 K, wavelength = 1310 nm, repetition rate = 1 MHz). Pulses contain 1 photon on average when attenuation is set at -57.4 dB (red vertical bar), polarization optimized for maximum count.

As shown in the various scans at 1310 nm, a linear relationship is observed when the count rate and the laser power are plotted on a log scale which shows that the SNSPD is detecting single photons. However this quantum detection regime also occurs for pulses containing more than one photon (to the right of -57.4 dB) for bias ratios higher than 65 % (and with a slope of 1). Indeed the sensitivity of the device is proportional to the bias ratio and the SNSPD fires at the first photon detected in a given optical pulse that may contain more than one.

We observe a slope of 2 when N is high and the bias current ratio is low. This is associated with a two photons detection mode of operation where two-photons events dominates the single-photon events. Similarly a slope of 3 is observed for even lower bias current ratio and high optical power as in [69] [17].

The system quantum efficiency can be extracted from those previous graphs when the input pulses contain 1 photon on average. Device 1 showed to have a SQE of about 0.01 % at 90 % bias ratio (Figure 4-5), whereas device 2 showed to have a SQE of about 1 % at 90 % bias ratio (Figure 4-6).

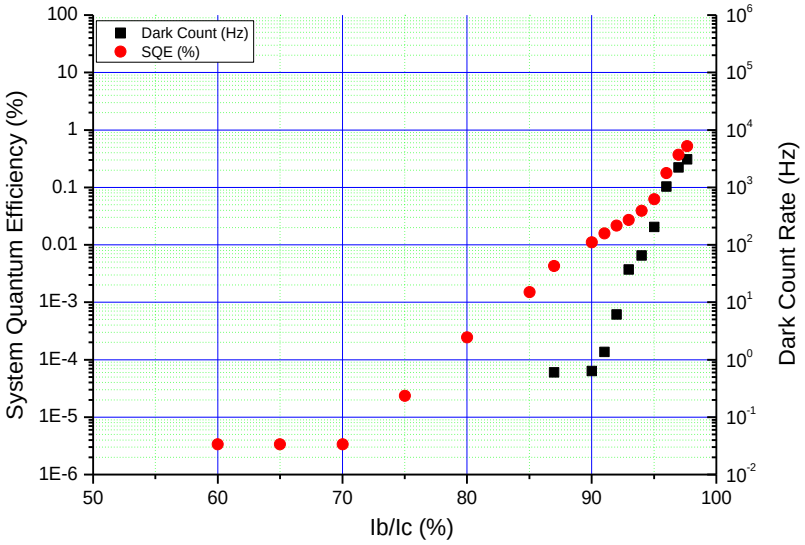

Figure 4-5 System quantum efficiency of device 1 versus bias current ratio (I_c = 15.06 µA, Temperature = 4.2 K, wavelength = 1310 nm, repetition rate = 1 MHz)

The dark-count rate seems to increase exponentially as the bias increases starting from a level of about 80 %. Below this bias level, spurious counts are very rare. However, it was observed that the measurement system developed was not completely free of electrical noise as some thousands of counts could suddenly be registered within a second (while de dark-count rate was less than $1.s^{-1}$) when a particular autonomous air pressure pump for the optical tables went on and off in the lab. This can be attributed to some back EMF spikes transmitted through the 110 V electrical grid.

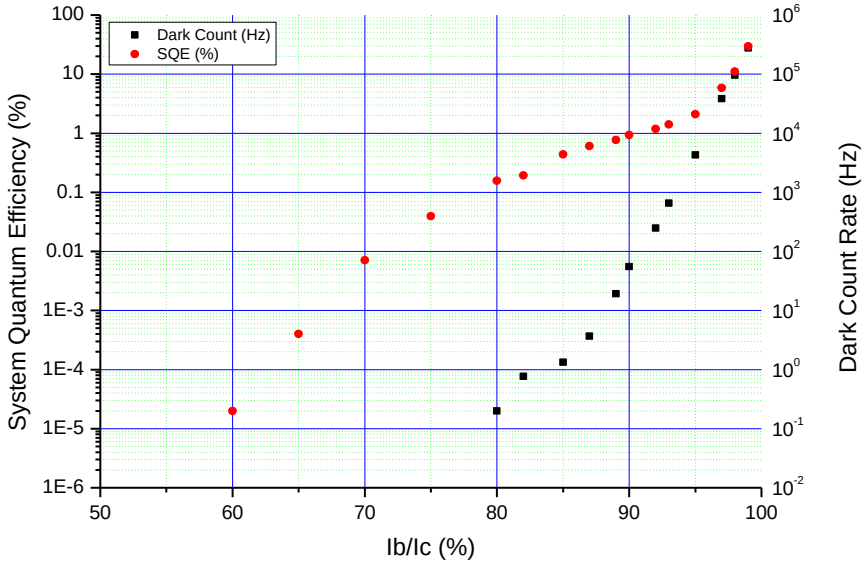

Figure 4-6 System quantum efficiency of device 2 versus bias current ratio (I_c = 27.00 µA, Temperature = 4.2 K, wavelength = 1310 nm, repetition rate = 1 MHz)

Finding the optimum point at which to operate the device depends on the dark-count budget that is tolerable in a particular system. If the SNSPD is used in a QKD system for example, increasing the bias current to 95 % or beyond does not provide a net advantage as the effective key rate would not significantly increase compared to the case where the current would be set to 90 %. This SQE and dark-count plots provide a relevant "identity card" for a SNSPD at a given temperature.

Comparing the SQE measurements obtained (Figure 4-6) to the original QE measurements provided by the supplier for that particular device and at the same temperature of 4.2 K (Figure 4-7) reveals that the coupling efficiency obtained was close to unity as the QE provided and SQE measured are almost identical. However the wavelength of the laser used by the provider is 1260 nm and it is possible that the measurement techniques and experimental setups may affect the extrapolated data. However great care was given to accuracy and exactness of the results in this work and it is fair to assume that the optical coupling model used by the manufacturer to extract the quantum efficiency is similar to the one developed in section 3.2.3.1.

It is therefore fair to expect that device 2 packaged using the robust methodology presented in this thesis would reach a system quantum efficiency close to 5 % at 90 % bias current like presented in the curve obtained at 1.78 K (Figure 4-7), if we had the capability to cool it down further than 4.2 K.

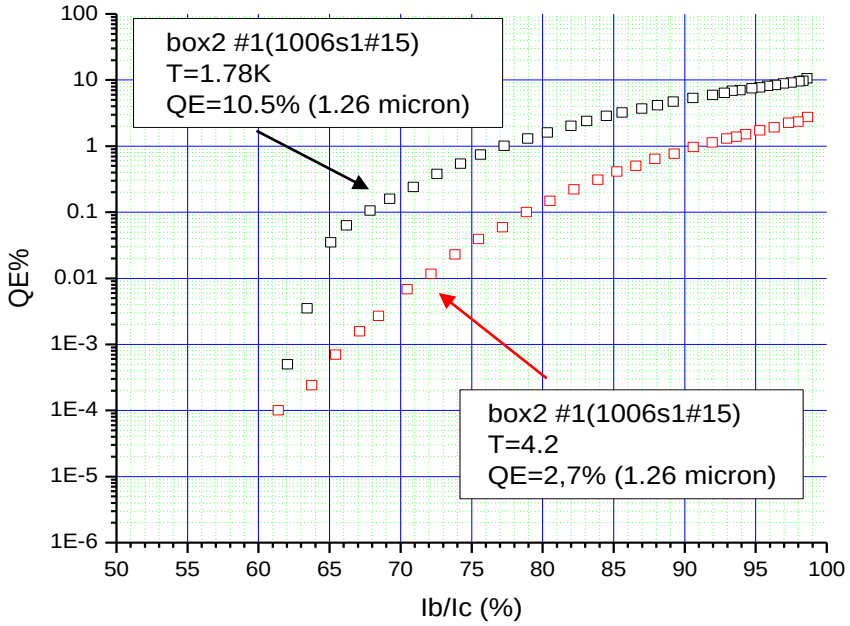

Figure 4-7 Quantum efficiency measurements of device 2 versus bias current ratio ((I_c = 29.8 µA at 4.2 K and 36.1 µA at 1.78 K, as measured by manufacturer before oxidation slightly degraded the quality of the device by reducing its critical current after 2 years of storage in ambient air., Temperature = 4.2 K, wavelength = 1260 nm)

4.3 Wavelength dependency of photo-detection

The two pulsed DFB lasers at 1310 nm and 1550 nm wavelength allowed performing a comparative test on device 2 given the same alignment. The height z of the anti reflection coated ferrule for 1310 nm was set at about 570 µm from the surface of the SNSPD and aligned as best as possible despite the large very fade spot that could be observed in the observation setup presented in section 3.2.3.2. The polarization was optimized in both cases for maximum count at a particular attenuation setting. The optical input was calibrated in both cases as well. The result of this experiment is presented in Figure 4-8. A lower pulse detection probability is observed for the 1550 nm laser.

The lower energy of the photon associated with the lower probability of creating a hotspot is a possible reason to explain the lower count. However the theoretical model for the optical coupling also predicts a reduced coupling factor over the same area given a particular alignment in XYZ. A third factor that contributes to this lower detection probability is that, as mentioned above, the optical fiber ferrule is anti reflection coated for 1310 nm and the silica-air interface will have a higher

reflectivity at 1550 nm than at 1310 nm for which it was designed. The appropriate ferrule with AR coating for 1550 nm available from the same manufacturer could be used of course, but it would be hard to reproduce the exact same alignment at this height. The choice of AR coating will therefore be adapted given the particular system in which the SNSPD device will be used in order to optimize the SQE.

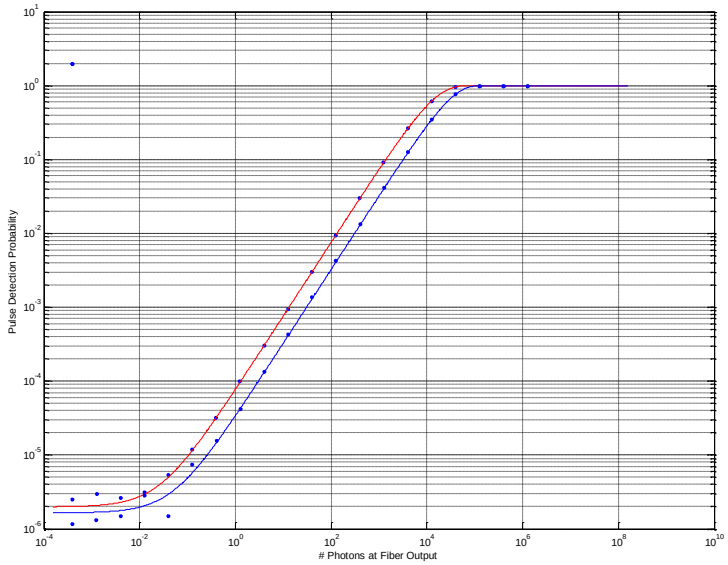

Figure 4-8 SNSPD pulse detection probability for device 2 with 1310 nm (red) and 1550 nm (blue) laser pulses after proper calibration of the optical paths and taking into account the coupling factor for the two wavelengths using the optical coupling model developed in 3.2.3. (I_b = 22.7 µA, polarization optimized for maximum counting, distance of fiber from device z = 570 µm, coupling efficiency = 2.35 % @1310 nm, 2.14 % @1550 nm)

Lastly, optical characterization of thin film NbN using ellipsometry or far infrared transmission spectroscopy [57] confirms this wavelength dependency as the reflectivity of the metallic film increases with the wavelength [70].

4.4 Speed and Jitter measurements

Characterization of the jitter of the device was performed using a different setup as previously described. Indeed, it was thought that the potential jitter of the 300 ps FWHM laser pulses triggered by a 5 V TTL square pulse using a non ideal source generator was in itself a source of potential error. A setup was built around a Coherent Mira 900 modelocked Ti:Sapphire femtosecond laser set to

output pulses of less than 2.5 ps duration at 800 nm (Figure 4-9 left) and 76.25 MHz repetition rate. The internal jitter of the modelocked laser is known to be in the order of a few femtoseconds.

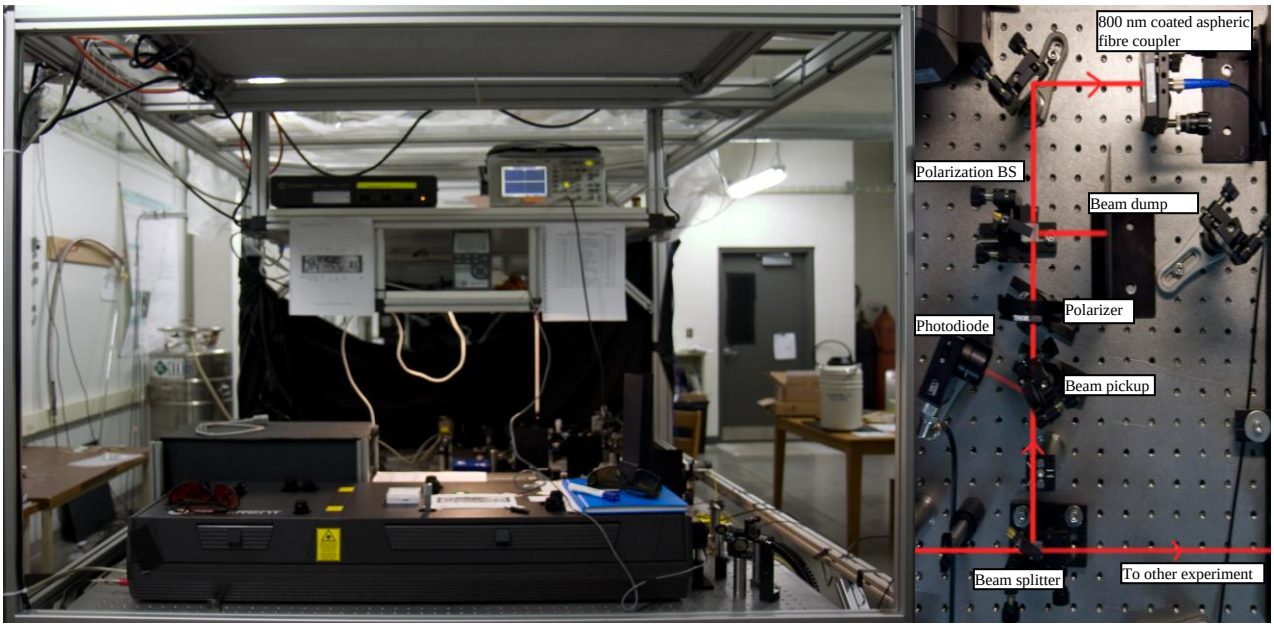

Figure 4-9 (Left) Coherent Mira 900 laser setup emitting laser pulses at 800 nm with pulse duration of about 2.5 ps at 76.25 MHz repetition rate. (Right) Optical setup with false-color representation of the laser path showing the approach to obtain continuously variable attenuation of the output and couple into a fiber connected to the dipper probe. Rotating the polarizer in front of the polarizing beam splitter modify the received power at the fiber coupler. Power is then calibrated with an optical power meter for various angle of the polarizer.

The laser beam was split and directed to an optical arrangement showed on the right of Figure 4-9. A beam pickup mirror samples a small portion of the light and sends it to a fast photodiode to monitor the pulse rate. This electrical signal will be used in our setup as the reference pulse for jitter measurements. The jitter of the signal measured by this DET10a diode is found to be less than 11 ps (2 standard deviations) as shown in Figure 4-10. The laser beam passes through a rotatable polarizer and sent to a polarization beam splitter. The deflected beam is sent to a beam dump, a black coated surface and the transmitted beam is sent to a fiber coupler and into a single mode fiber for 800 nm. This arrangement allows controlling the amount of power coupled to the fiber by controlling the angle of the polarizer with respect to the fix polarization beam splitter. The other end of the fiber is properly calibrated at this wavelength after the adjunction of another SMF28 patch cable in order to take into account the mode mismatch between those two families of fibers with different core diameters. The cutoff wavelength for single mode operation of SMF28 fiber is 1260 nm. Wavelengths below this

cutoff will be launched into the fiber in multi modes and will experience higher loss and dispersion. Since the overall length of fiber through which it is propagating is about 3 meters, the dispersion of the pulse can be neglected and the loss accounted for.

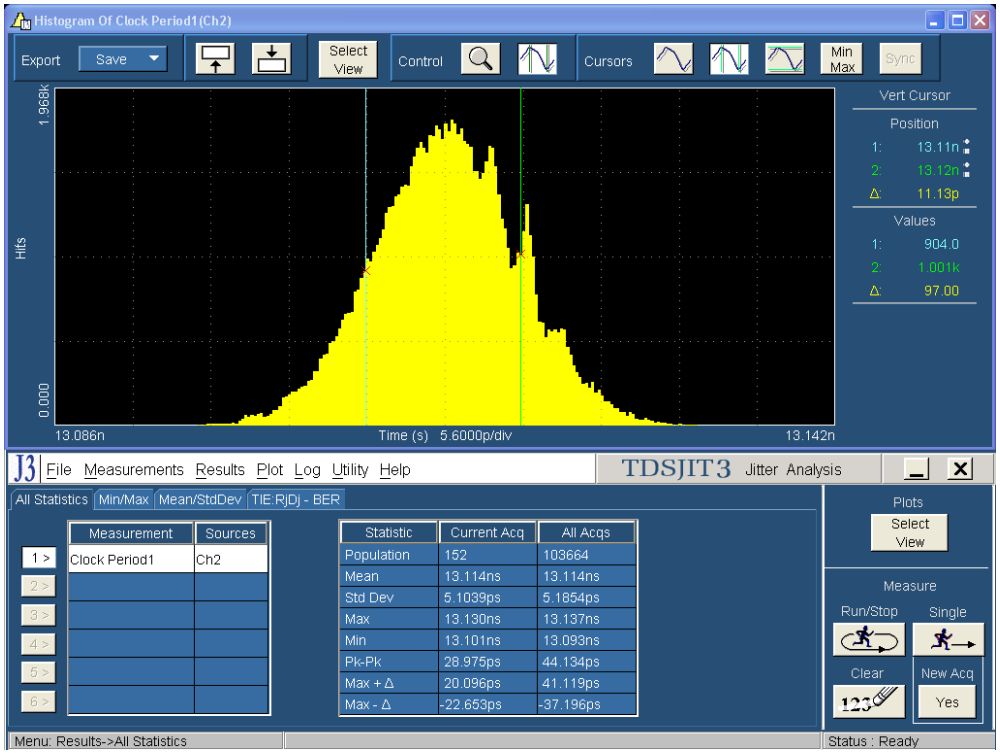

Figure 4-10 DET10A photo diode period jitter measurement. Jitter = 2. Std. Dev. ≈ 11 ps. Mean period = 13.114 ns → mean repetition rate ≈ 76.25438 MHz.

The optical output of the system described above is set to send to the SNSPD pulses containing few photons or less and the jitter measurements of device 2 is performed and presented in Figure 4-11. When detecting in single-photon mode, the jitter of the device is found to be about 60 ps, or twice the standard deviation of the histogram plotted in this figure. The measured jitter is the jitter of the delay between the DET10a pulse and the SNSPD photo response pulse set to trigger at a level of 50 % of the photo diode pulse amplitude. Since this jitter is measured with respected to the rising edge of the DET10a, the diode intrinsic jitter would need to be deconvolved from the measured SNSPD jitter in order to truly characterize the device's property.

In order to understand the possible influence of the bias tee and microwave amplifier on the jitter, the output of the photo diode was first attenuated by 20 dB, connected to the RF+DC port of the bias

tee and fed in the amplifier. The jitter of this signal was measured and no significant difference was found from the previously measured 11 ps.

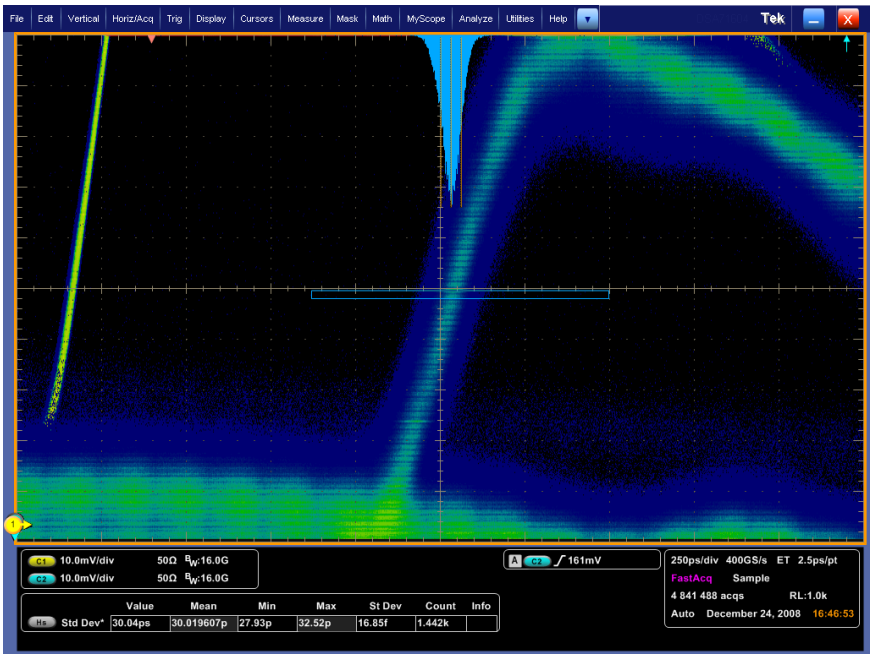

Figure 4-11 SNSPD device 2 jitter measurement in single photon detection regime (laser power = -61.8 dBm , wavelength = 800 nm, distance of fiber from device z ≈ 300 µm)

The speed of a typical 500 µm long superconducting wire with kinetic inductance of about 350 to 400 nH should be defined as the inverse of the relaxation time. Looking back at Figure 2-14 on page 19, the time it takes to the voltage to fall back to its reset state is about 30 ns corresponding to a frequency of 33.33 MHz. Although the device was operated in this test at a repetition rate of 76.25 MHz, the chance of a photon to get detected in the next period after a photon event is lower as the device has not fully recovered. Figure 4-12 shows a capture of the rare occurrence of an event were three consecutive SNSPD pulses were recorded. The peak voltages decrease on the second and third pulse of the sequence and the device does not go back to the ground level in between.

Figure 4-13 shows the record of four consecutive photon detection events occurring at about half the repetition rate. Two or more events separated by 28 to 30 ns were very frequent and the peak voltage of the pulses did not follow any particular pattern. Similar speed evaluation tests were performed using the electrically triggered 1310 nm laser and similar conclusions were drawn from the measurements.

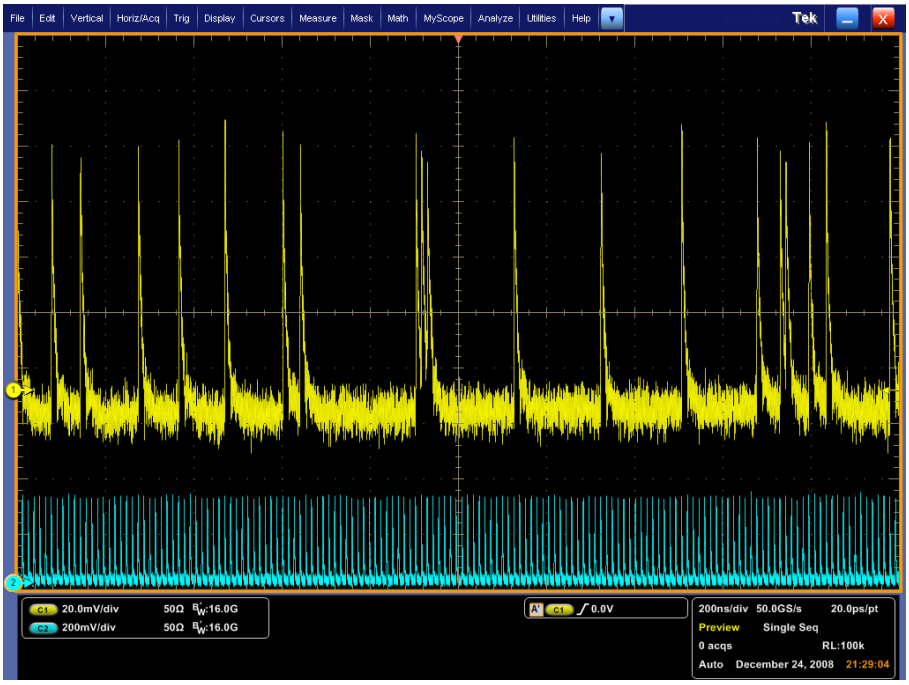

Figure 4-12 SNSPD response at f = 76.25 MHz. In blue, the photodiode pulses. In yellow, the SNSPD pulses.

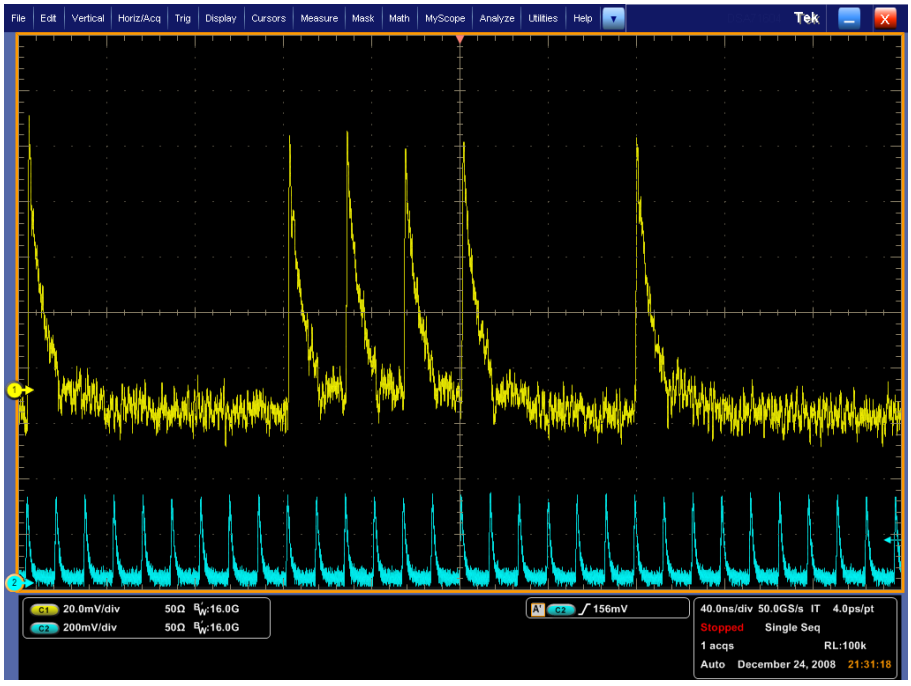

Figure 4-13 Zoomed view of SNSPD response at f = 76.25 MHz. In blue, the photodiode pulses. In yellow, the SNSPD pulses.

The tests conducted provide a preliminary understanding of the device's speed behavior and intrinsic jitter. Further tests could investigate on the relation between detection probability and speed as well as the effect of bias current ratio and jitter. The number of photons per pulse is also thought to have effects on the growth and dynamic of hot spots formation and gaining more understanding of these phenomena could help designing more efficient devices.

It is clear from our analysis that to improve the speed of the device, the impedance seen by the kinetic inductance must be adapted to reduce the fall time. This can be implemented using a series resistor in the future as in [71]. The 3 mm long coplanar waveguide in the packaging presented earlier can support the addition of a surface mount resistor and was designed with this objective in mind. Figure 4-14 simulates the electrical model previously presented in section 2.3.1 but with the addition of a resistor in series with the same inductor modeling the kinetic inductance of the SNSPD.

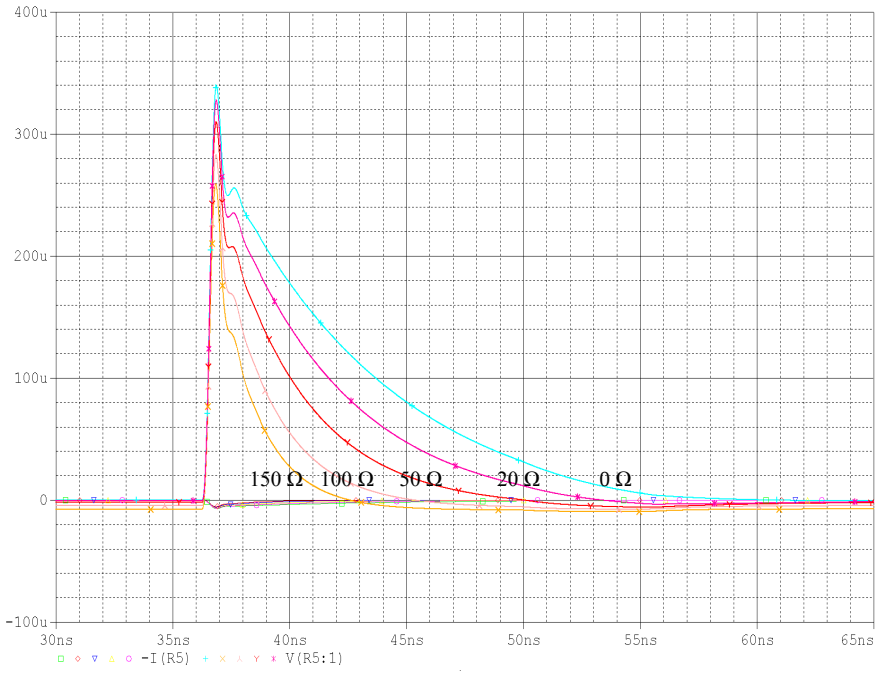

Figure 4-14 SPICE simulation of circuit of section 2.3.1 with the addition of a resistor is series with the inductor L_1 = 350 nH. Speed improvement due to reduced fall time is observed for a few values of the resistance.

We observe a reduced fall time as the resistance is increased and such scheme will be implemented in our system in the future. The peak voltage is reduced when the resistance increases but it would not be an issue with the adjustable discriminator used to count the pulses. For a value of 150 Ω, operation

at a repetition rate of 125MHz is expected with our current devices. This analysis shows that the device's speed is not intrinsically related to the size of the device only but is highly dependent on the measuring scheme and can be modified with proper electrical and microwave design. The design of a proper impedance matching circuit and the use of a cryogenic amplifier would further improve the performance.

Other groups have taken another approach to reduce the overall kinetic inductance and improve the speed, by segmenting the detectors in multiple parallel sections. [72] [73] [74] [75]. Indeed the total kinetic inductance is the parallel combination of the inductances of each stripe. With the appropriate fabrication facilities, this scheme is also a way that should be investigated.

Chapter 5
Conclusions and Future Work

Part of the experiments were performed over 5 weeks with a single 60 L liquid helium Dewar, where the devices were kept at cryogenic temperature and experienced about 30 thermal cycles but showed very stable and reproducible results over time. While the devices were maintained in a superconducting state, we observed temperature fluctuations of only 20 mK over the span of a few days, showing the stability and reliability of the system we built, not to mention its cost effectiveness due to low helium consumption. We found that the measured SQE was very close to the intrinsic QE of the devices, proof of a good optical coupling, and the measured dark-counts below 80 % bias ratio were below 10^{-4} Hz. We successfully verified our design methodology for robust packaging of superconducting detectors with the prototypes we made and gained a good understanding of the limiting speed factor of current devices with large area by simulation and theoretical analysis.

One of the current issues associated with those devices is that the quantum efficiency, tuned by the bias current ratio, is proportional to the dark-count rate thus reducing the attractiveness of the device if pushed to 98 % bias ratio for example. Cryogenic operation might still be a limiting factor for wide adoption of such detector systems in remote locations, but cryogen-free refrigerators requiring only an electrical supply are becoming more affordable. The small form factor of the robust fiber pigtailed packaged developed in this work is well suited for maintenance-free operation in such a system.

We propose and exemplify a method to design a QKD system where the information would be encoded in pulses containing one photon on average at the source at 1310 nm wavelength. From Figure 4-4, we extract an optimally chosen bias point for device 2 that provides a reasonably low dark-count (less than 4 per second). Figure 5-1 shows, to the left of the single photon regime represented by the red vertical line, a tuning triangle where each channel loss in this communication scheme has a corresponding system quantum efficiency. In this figure a 20dB loss is simulated with its corresponding 0.005 % chance of detecting the photon that has travelled approximately 100 km if we assume an optical loss 0.2 dB/km. Assuming the device's speed could be tuned with an appropriate series resistor as presented in section 4.4 to a speed of 100MHz, a 5 KHz raw key rate is expected (32.5 KHz expected rate at 1.75 K). In this way, given a channel loss and dark-counts budget, one can optimize the system and the biasing scheme of the detector.

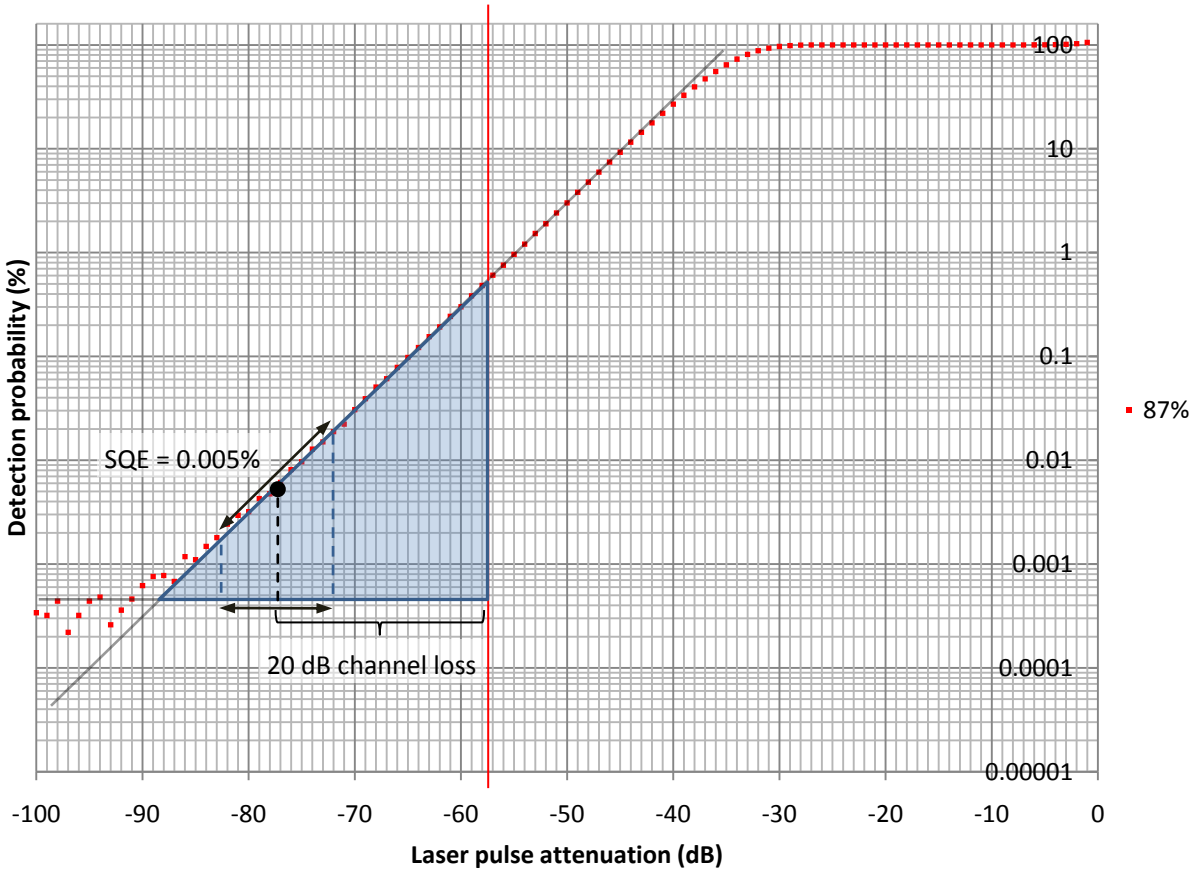

Figure 5-1 Proposed document for the design of a QKD link using SNSPDs characterization curves. The detection probability curve is plotted for a chosen bias ratio of 87 % for device 2 at 1310 nm and 4.2 K. From Figure 4-6, the dark-count is less than 4 per second. A 20dB channel loss is simulated along the overlaid blue triangle assuming the source pulses contain one photon. The corresponding SQE is obtained from projecting the relative attenuation value on the hypotenuse.

The field of superconducting single photon detectors has made a lot of progress in the past few years but more theoretical studies are necessary to fully understand the underlying physics of photon detection mechanism. From this improved understanding, novel device structures will be conceived, increasing the device detection efficiency and speed. Present studies investigate the photon energy resolution and photon number resolving capabilities of those superconducting structures [76] [50] [77] [78] [79]. The polarization dependency of the device is better understood and taken into account for the design of new devices [70] [80] [81]. Those two additional features would allow new schemes for quantum optical communication and quantum optics experiments. The high speed operation and single photon detection capabilities of SNSPDs make it a prospective candidate for high speed free space communication system as well as other astronomical and space projects [82] [83] [84].

Bibliography

[1] R. H. Hadfield, M. J. Stevens, S. S. Gruber, A. J. Miller, R. E. Schwall, R. P. Mirin, and S. W. Nam, "Single photon source characterization with a superconducting single photon detector," *Opt. Express*, vol. 13, no. 26, pp. 10846–10853, Dec. 2005. [Online]. Available: http://www.opticsexpress.org/abstract.cfm?URI=oe-13-26-10846

[2] R. Hadfield, M. Stevens, R. Mirin, and S. W. Nam, "Single-photon source characterization with twin infrared-sensitive superconducting single-photon detectors," *Journal of Applied Physics*, vol. 101, no. 10, pp. 103104 – 1, 2007. [Online]. Available: http://dx.doi.org/10.1063/1.2717582

[3] C. Liang, K. F. Lee, M. Medic, P. Kumar, R. H. Hadfield, and S. W. Nam, "Characterization of fiber-generated entangled photon pairs with superconducting single-photon detectors," *Opt. Express*, vol. 15, no. 3, pp. 1322–1327, Feb. 2007. [Online]. Available: http://www.opticsexpress.org/abstract.cfm?URI=oe-15-3-1322

[4] C. Zinoni, B. Alloing, L. Li, F. Marsili, A. Fiore, L. Lunghi, A. Gerardino, Y. Vakhtomin, K. Smirnov, and G. Gol'tsman, "Single-photon experiments at telecommunication wavelengths using nanowire superconducting detectors," *Applied Physics Letters*, vol. 91, no. 3, pp. 31106 – 1, 2007. [Online]. Available: http://dx.doi.org/10.1063/1.2752108

[5] F. Stellari and P. Song, "Testing of ultra low voltage cmos microprocessors using the superconducting single-photon detector (sspd)," in *Proc. 12th International Symposium on the Physical and Failure Analysis of Integrated Circuits IPFA 2005*, 27 June–1 July 2005, p. 2.

[6] J. Zhang, N. Boiadjieva, G. Chulkova, H. Deslandes, G. N. Gol'tsman, A. Korneev, P. Kouminov, M. Leibowitz, W. Lo, R. Malinsky, O. Okunev, A. Pearlman, W. Slysz, K. Smirnov, C. Tsao, A. Verevkin, B. Voronov, K. Wilsher, and R. Sobolewski, "Noninvasive cmos circuit testing with NbN superconducting single-photon detectors," *Electronics Letters*, vol. 39, no. 14, pp. 1086–1088, 10 July 2003.

[7] J. Zhang, A. Pearlman, W. Slysz, A. Verevkin, R. Sobolewski, O. Okunev, A. Korneev, P. Kouminov, K. Smirnov, G. Chulkova, G. N. Gol'tsman, W. Lo, and K. Wilsher, "Infrared picosecond superconducting single-photon detectors for cmos-tircuit testing," in *Proc. Conference on Lasers and Electro-Optics CLEO '03*, 1–6 June 2003, pp. 328–329.

[8] C. Gobby, Z. L. Yuan, and A. J. Shields, "Quantum key distribution over 122 km of standard telecom fiber," *Applied Physics Letters*, vol. 84, no. 19, pp. 3762–3764, 2004. [Online]. Available: http://link.aip.org/link/?APL/84/3762/1

[9] R. Collins, R. Hadfield, V. Fernandez, S. Nam, and G. Buller, "Low timing jitter detector for gigahertz quantum key distribution," *Electronics Letters*, vol. 43, no. 3, pp. 180 – 2, 2007. [Online]. Available: http://dx.doi.org/10.1049/el:20073748

[10] G. Gol'tsman, O. Minaeva, A. Korneev, M. Tarkhov, I. Rubtsova, A. Divochiy, I. Milostnaya, G. Chulkova, N. Kaurova, B. Voronov, D. Pan, J. Kitaygorsky, A. Cross, A. Pearlman, I. Komissarov, W. Slysz, M. Wegrzecki, P. Grabiec, and R. Sobolewski, "Middle-infrared to visible-light ultrafast superconducting single-photon detectors," *IEEE Transactions on Applied Superconductivity*, vol. 17, no. 2, pp. 246–251, June 2007.

[11] R. Hadfield, J. Habif, J. Schlafer, R. Schwall, and S. W. Nam, "Quantum key distribution at 1550 nm with twin superconducting single-photon detectors," *Applied Physics Letters*, vol. 89, no. 24, pp. 241129 – 1, 2006. [Online]. Available: http://dx.doi.org/10.1063/1.2405870

[12] T. Honjo, S. W. Nam, H. Takesue, Q. Zhang, H. Kamada, Y. Nishida, O. Tadanaga, M. Asobe, B. Baek, R. Hadfield, S. Miki, M. Fujiwara, M. Sasaki, Z. Wang, K. Inoue, and Y. Yamamoto, "Entanglement-based bbm92 qkd experiment using superconducting single photon detectors," in *Proc. and 2008 Conference on Quantum Electronics and Laser Science Lasers and Electro-Optics CLEO/QELS 2008. Conference on*, 4–9 May 2008, pp. 1–2.

[13] D. Rosenberg, C. Peterson, J. Harrington, P. Rice, N. Dallmann, K. Tyagi, K. McCabe, R. Hughes, J. Nordholt, R. Hadfield, B. Baek, and S. Nam, "Long distance quantum key distribution in optical fiber," Piscataway, NJ, USA, 2008, pp. 2911 – 13.

[14] H. Takesue, T. Honjo, K. Tamaki, and Y. Tokura, "Differential phase shift quantum key distribution," in *Proc. First ITU-T Kaleidoscope Academic Conference Innovations in NGN: Future Network and Services K-INGN 2008*, 2008, pp. 229–236.

[15] E. Dauler, B. Robinson, A. Kerman, V. Anant, R. Barron, K. Berggren, D. Caplan, J. Carney, S. Hamilton, K. Rosfjord, M. Stevens, and J. Yang, "1.25-gbit/s photon-counting optical communications using a two-element superconducting nanowire single photon detector," vol. 6372, USA, 2006, pp. 637212 – 1. [Online]. Available: http://dx.doi.org/10.1117/12.690627

[16] B. Robinson, A. Kerman, E. Dauler, R. Barron, D. Caplan, M. Stevens, J. Carney, S. Hamilton, J. Yang, and K. Berggren, "781 mbit/s photon-counting optical communications using a superconducting nanowire detector," *Optics Letters*, vol. 31, no. 4, pp. 444 – 6, 2006. [Online]. Available: http://dx.doi.org/10.1364/OL.31.000444

[17] R. Sobolewski, A. Verevkin, G. N. Gol'tsman, A. Lipatov, and K. Wilsher, "Ultrafast superconducting single-photon optical detectors and their applications," *IEEE Transactions on Applied Superconductivity*, vol. 13, no. 2, pp. 1151–1157, June 2003.

[18] B. Saleh and M. Teich, *Fundamentals of Photonics*. John Wiley & Sons, 1991. pp 463,464, 753.

[19] R. Romestain, B. Delaet, P. Renaud-Goud, I. Wang, C. Jorel, J.-C. Villegier, and J.-P. Poizat, "Fabrication of a superconducting niobium nitride hot electron bolometer for single-photon counting," *New Journal of Physics*, vol. 6, pp. 129–129, 2004.

[20] J. Kim, S. Takeuchi, Y. Yamamoto, and H. H. Hogue, "Multiphoton detection using visible light photon counter," *Appl. Phys. Lett.*, vol. 74, no. 7, pp. 902–904, Feb. 1999. [Online]. Available: http://link.aip.org/link/?APL/74/902/1

[21] E. Waks, K. Inoue, W. Oliver, E. Diamanti, and Y. Yamamoto, "High-efficiency photon-number detection for quantum information processing," *Selected Topics in Quantum Electronics, IEEE Journal of*, vol. 9, no. 6, pp. 1502–1511, Nov.-Dec. 2003.

[22] A. Peacock, P. Verhoeve, N. Rando, A. van Dordrecht, B. G. Taylor, C. Erd, M. A. C. Perryman, R. Venn, J. Howlett, D. J. Goldie, J. Lumley, and M. Wallis, "Single optical photon detection with a superconducting tunnel junction," *Nature*, vol. 381, no. 6578, pp. 135–137, May 1996. [Online]. Available: http://dx.doi.org/10.1038/381135a0

[23] A. G. Kozorezov, R. D. Hartog, J. K. Wigmore, G. B. Brammertz, A. Peacock, D. Martin, and N. Verhoeve, P. Rando, "The effect of quasiparticle self-generation on the performance of small gap multiple tunnelling stjs," *Nuclear Instruments and Methods in Physics Research Section A: Accelerators, Spectrometers, Detectors and Associated Equipment*, vol. Volume 520, Issues 1-3, pp. 227–230, 2004.

[24] H. M. Shimizu, "International progress on advanced optics and sensors," in *International Progress on Advanced Optics and Sensors*, H. Ohmori and H. M. Shimizu, Eds. Universal Academy

Press, Inc., 2003, pp. 15–22, iSBN 4-946443-76-2. [Online]. Available: http://www.uap.co.jp/uap/Publication/SERIES/DATA/00080/index.html

[25] J.-C. Villegier, P. Feautrier, C. Jorel, B. Delaet, and J.-L. Thomassin, "International progress on advanced optics and sensors," in *International Progress on Advanced Optics and Sensors*, H. Ohmori and H. M. Shimizu, Eds. Universal Academy Press, Inc., 2003, pp. 367–73. [Online]. Available: http://www.uap.co.jp/uap/Publication/SERIES/DATA/00080/index.html

[26] P. K. Day, H. G. LeDuc, B. A. Mazin, A. Vayonakis, and J. Zmuidzinas, "A broadband superconducting detector suitable for use in large arrays," *Nature*, vol. 425, no. 6960, pp. 817–821, Oct. 2003. [Online]. Available: http://dx.doi.org/10.1038/nature02037

[27] P. A. J. de Korte, J. Beyer, S. Deiker, G. C. Hilton, K. D. Irwin, M. MacIntosh, S. W. Nam, C. D. Reintsema, L. R. Vale, and M. E. Huber, "Time-division superconducting quantum interference device multiplexer for transition-edge sensors," *Rev. Sci. Instrum.*, vol. 74, no. 8, pp. 3807–3815, Aug. 2003. [Online]. Available: http://link.aip.org/link/?RSI/74/3807/1

[28] A. D. Semenov, G. N. Gol'tsman, and A. Korneev, "Quantum detection by current carrying superconducting film," *Physica C: Superconductivity*, vol. 351, pp. 349–356, april 2001.

[29] A. Verevkin, J. Zhang, R. Sobolewski, A. Lipatov, O. Okunev, G. Chulkova, A. Korneev, K. Smirnov, G. N. Gol'tsman, and A. Semenov, "Detection efficiency of large-active-area NbN single-photon superconducting detectors in the ultraviolet to near-infrared range," *Applied Physics Letters*, vol. 80, no. 25, pp. 4687–4689, 2002. [Online]. Available: http://link.aip.org/link/?APL/80/4687/1

[30] A. Korneev, P. Kouminov, V. Matvienko, G. Chulkova, K. Smirnov, B. Voronov, G. N. Gol'tsman, M. Currie, W. Lo, K. Wilsher, J. Zhang, W. Slysz, A. Pearlman, A. Verevkin, and R. Sobolewski, "Sensitivity and gigahertz counting performance of NbN superconducting single-photon detectors," *Applied Physics Letters*, vol. 84, no. 26, pp. 5338–5340, 2004. [Online]. Available: http://link.aip.org/link/?APL/84/5338/1

[31] P. L. Richards, "Bolometers for infrared and millimeter waves," *J. Appl. Phys.*, vol. 76, no. 1, pp. 1–24, Jul. 1994. [Online]. Available: http://link.aip.org/link/?JAP/76/1/1

[32] E. Reiger, S. Dorenbos, V. Zwiller, A. Korneev, G. Chulkova, I. Milostnaya, O. Minaeva, G. Gol'tsman, J. Kitaygorsky, D. Pan, W. Sysz, A. Jukna, and R. Sobolewski, "Spectroscopy with

nanostructured superconducting single photon detectors," *IEEE Journal of Selected Topics in Quantum Electronics*, vol. 13, no. 4, pp. 934–943, July–aug. 2007.

[33] *SPCM-AQR-16-FC Si APD single photon counting module with less than 25 dark-count/second (2007)*. [Online]. Available: http://optoelectronics.perkinelmer.com

[34] *id201 Single photon detection module - Near infrared range*. [Online]. Available: http://www.idquantique.com/products/id200.htm

[35] A. Korneev, V. Matvienko, O. Minaeva, I. Milostnaya, I. Rubtsova, G. Chulkova, K. Smirnov, V. Voronov, G. Gol'tsman, W. Slysz, A. Pearlman, A. Verevkin, and R. Sobolewski, "Quantum efficiency and noise equivalent power of nanostructured, NbN, single-photon detectors in the wavelength range from visible to infrared," *IEEE Transactions on Applied Superconductivity*, vol. 15, no. 2, pp. 571–574, June 2005. [Online]. Available: http://dx.doi.org/10.1109/TASC.2005.849923

[36] D. Rosenberg, A. E. Lita, A. J. Miller, and S. W. Nam, "Noise-free high-efficiency photon-number-resolving detectors," *Phys. Rev. A*, vol. 71, no. 6, pp. 061803–, Jun. 2005. [Online]. Available: http://link.aps.org/abstract/PRA/v71/e061803

[37] A. J. . Miller, S. W. . Nam, J. M. . Martinis, and A. V. . Sergienko, "Demonstration of a low-noise near-infrared photon counter with multiphoton discrimination," *Applied Physics Letters*, vol. 83, no. 4, pp. 791–793, 20030728 2003, nR: 23; CD: APPLA; NU: 37018157.

[38] D. D. E. Martin, P. Verhoeve, R. H. den Hartog, J. H. de Bruijne, A. P. Reynolds, A. van Dordrecht, J. Verveer, and A. J. Peacock, "12x10 pixels superconducting tunnel junction array based spectro-photometer for optical astronomy," in *Proc. SPIE*, vol. 4841, no. 1. Waikoloa, HI, USA: SPIE, Mar. 2003, pp. 805–814. [Online]. Available: http://link.aip.org/link/?PSI/4841/805/1

[39] K. Rosfjord, J. Yang, E. Dauler, A. Kerman, V. Anant, B. Voronov, G. Gol'tsman, and K. Berggren, "Nanowire single-photon detector with an integrated optical cavity and anti-reflection coating," *Optics Express*, vol. 14, no. 2, 2006.

[40] A. E. Lita, A. J. Miller, and S. W. Nam, "Counting near-infrared single-photons with 95% efficiency," *Opt. Express*, vol. 16, no. 5, pp. 3032–3040, Mar. 2008. [Online]. Available: http://www.opticsexpress.org/abstract.cfm?URI=oe-16-5-3032

[41] R. E. de Lamaestre, P. Odier, E. Bellet-Amalric, P. Cavalier, S. Pouget, and J.-C. Villegier, "High quality ultrathin NbN layers on sapphire for superconducting single photon detectors," *Journal of Physics: Conference Series*, vol. 97, p. 012046 (6pp), 2008. [Online]. Available: http://stacks.iop.org/1742-6596/97/012046

[42] J. Yang, E. Dauler, A. Ferri, A. Pearlman, A. Verevkin, G. Gol'tsman, B. Voronov, R. Sobolewski, W. Keicher, and K. Berggren, "Fabrication development for nanowire ghz-counting-rate single-photon detectors," *IEEE Transactions on Applied Superconductivity*, vol. 15, no. 2, pp. 626 – 30, 2005. [Online]. Available: http://dx.doi.org/10.1109/TASC.2005.849971

[43] F. Marsili, D. Bitauld, A. Fiore, A. Gaggero, F. Mattioli, R. Leoni, M. Benkahoul, and F. Lévy, "High efficiency NbN nanowire superconducting single photon detectors fabricated on mgo substrates from a low temperature process," *Opt. Express*, vol. 16, no. 5, pp. 3191–3196, 2008. [Online]. Available: http://www.opticsexpress.org/abstract.cfm?URI=oe-16-5-3191

[44] H. Takesue, S. W. Nam, Q. Zhang, R. H. Hadfield, T. Honjo, K. Tamaki, and Y. Yamamoto, "Quantum key distribution over a 40-db channel loss using superconducting single-photon detectors," *Nature Photonics*, vol. 1, pp. 343–348, jun 2007.

[45] W. Slysz, M. Wegrzecki, J. Bar, P. Grabiec, M. Gorska, E. Rieger, S. Dorenbos, V. Zwiller, I. Milostnaya, O. Minaeva, A. Antipov, O. Okunev, A. Korneev, K. Smirnov, B. Voronov, N. Kaurova, G. N. Gol'tsman, J. Kitaygorsky, D. Pan, A. Pearlman, A. Cross, I. Komissarov, and R. Sobolewski, "Fiber-coupled NbN superconducting single-photon detectors for quantum correlation measurements," I. Prochazka, A. L. Migdall, A. Pauchard, M. Dusek, M. S. Hillery, and W. P. Schleich, Eds., vol. 6583, no. 1. SPIE, 2007, p. 65830J. [Online]. Available: http://link.aip.org/link/?PSI/6583/65830J/1

[46] S. Miki, M. Fujiwara, M. Sasaki, and Z. Wang, "Nbn superconducting single-photon detectors prepared on single-crystal mgo substrates," *IEEE Transactions on Applied Superconductivity*, vol. 17, no. 2, pp. 285–288, June 2007.

[47] J. Zhang, W. Slysz, A. Pearlman, A. Verevkin, R. Sobolewski, O. Okunev, G. Chulkova, and G. N. Gol'tsman, "Time delay of resistive-state formation in superconducting stripes excited by single optical photons," *Phys. Rev. B*, vol. 67, no. 13, pp. 132508–, Apr. 2003. [Online]. Available: http://link.aps.org/abstract/PRB/v67/e132508

[48] G. N. Gol'tsman, O. Okunev, G. Chulkova, A. Lipatov, A. Semenov, K. Smirnov, B. Voronov, A. Dzardanov, C. Williams, and R. Sobolewski, "Picosecond superconducting single-photon optical detector," *Appl. Phys. Lett.*, vol. 79, no. 6, pp. 705–707, Aug. 2001. [Online]. Available: http://link.aip.org/link/?APL/79/705/1

[49] M. Bell, N. Kaurova, A. Divochiy, G. Gol'tsman, J. Bird, A. Sergeev, and A. Verevkin, "On the nature of resistive transition in disordered superconducting nanowires," *IEEE Transactions on Applied Superconductivity*, vol. 17, no. 2, pp. 267 – 70, 2007. [Online]. Available: http://dx.doi.org/10.1109/TASC.2007.898619

[50] P. Haas, A. Semenov, H. W. Hubers, P. J. Beyer, A. Kirste, T. Schurig, K. Il'in, M. Siegel, A. Engel, and A. Smirnov, "Spectral sensitivity and spectral resolution of superconducting single-photon detectors," *IEEE Transactions on Applied Superconductivity*, vol. 17, no. 2, pp. 298–301, 2007.

[51] K. Il'in, M. Siegel, A. Engel, H. Bartolf, A. Schilling, A. Semenov, and H.-W. Huebers, "Current-induced critical state in NbN thin-film structures," *Journal of Low Temperature Physics*, vol. 151, no. 1, pp. 585–590, April 2008. [Online]. Available: http://dx.doi.org/10.1007/s10909-007-9690-5

[52] A. Semenov, P. Haas, H.-W. Hubers, K. Ilin, M. Siegel, A. Kirste, T. Schurig, and A. Engel, "Vortex-based single-photon response in nanostructured superconducting detectors," *Physica C*, vol. 468, no. 7-10, pp. 627 – 30, 2008. [Online]. Available: http://dx.doi.org/10.1016/j.physc.2007.11.028

[53] A. Jukna, J. Kitaygorsky, D. Pan, A. Cross, A. Perlman, I. Komissarov, R. Sobolewski, O. Okunev, K. Smirnov, A. Korneev, G. Chulkova, I. Milostnaya, B. Voronov, and G. N. Gol'Tsman, "Dynamics of hotspot formation in nanostructured superconducting stripes excited with single photons," *Acta Physica Polonica A*, vol. vol. 113, Issue 3, p. p.955, 2008. [Online]. Available: http://adsabs.harvard.edu/abs/2008AcPPA.113..955J

[54] K. S. Il'in, M. Lindgren, M. Currie, A. D. Semenov, G. N. Gol'tsman, R. Sobolewski, S. I. Cherednichenko, and E. M. Gershenzon, "Picosecond hot-electron energy relaxation in NbN superconducting photodetectors," *Appl. Phys. Lett.*, vol. 76, no. 19, pp. 2752–2754, May 2000. [Online]. Available: http://link.aip.org/link/?APL/76/2752/1

[55] F. Marsili, "Single-photon and photon-number-resolving detectors based on superconducting nanowires," Ph.D. dissertation, EPF Lausanne, 2009.

[56] M. Benkahoul, “Niobium nitride based thin films deposited by dc reactive magnetron sputtering : Nbn, nbsin and nbain,” Ph.D. dissertation, EPF Lausanne, 2005.

[57] J.-C. Villegier, B. Delaet, P. Feautrier, L. Frey, C. Delacour, and V. Bouchiat, “Fabrication of high-speed single photon detectors in NbN for quantum information processing,” *Journal of Physics: Conference Series*, vol. 43, pp. 1373–1376, 2006.

[58] A. Kerman, E. Dauler, J. Yang, K. Rosfjord, V. Anant, K. Berggren, G. Gol’tsman, and B. Voronov, “Constriction-limited detection efficiency of superconducting nanowire single-photon detectors,” *Applied Physics Letters*, vol. 90, no. 10, pp. 101110 – 1, 2007. [Online]. Available: http://dx.doi.org/10.1063/1.2696926

[59] J. K. Yang, “Fabrication of superconducting nanowire single proton detectors,” Master’s thesis, Massachusetts Institute of Technology. Dept. of Electrical Engineering and Computer Science., 2005.

[60] F. A. Hegmann and J. S. Preston, “Origin of the fast photoresponse of epitaxial yba2cu3o7-delta thin films,” *Phys. Rev. B*, vol. 48, no. 21, pp. 16023–, Dec. 1993. [Online]. Available: http://link.aps.org/abstract/PRB/v48/p16023

[61] A. J. Kerman, E. A. Dauler, W. E. Keicher, J. K. W. Yang, K. K. Berggren, G. Gol’tsman, and B. Voronov, “Kinetic-inductance-limited reset time of superconducting nanowire photon counters,” *Applied Physics Letters*, vol. 88, no. 11, p. 111116, 2006. [Online]. Available: http://link.aip.org/link/?APL/88/111116/1

[62] J. Ekin, *Experimental Techniques Cryostat Design, Material Properties and Superconductor Critical-Current Testing*. Oxford University Press, 2006. pp 73, 235, 236, 514, 465, 519.

[63] Z. Yan, M. K. Akhlaghi, J. L. Orgiazzi, and A. Hamed Majedi, “Optoelectronic characterization of a fiber-coupled NbN superconducting nanowire single photon detector,” *Journal of Modern Optics*, vol. 56, no. 2, pp. 380–384, 2009. [Online]. Available: http://www.informaworld.com/10.1080/09500340802339818

[64] H. S. Enss, Christian, *Low-Temperature Physics*. Springer, 2005. p 465

[65] *id300 Short-pulse laser source*. [Online]. Available: http://www.idquantique.com/products/id300.htm

[66] M. Akhlaghi, “Iqol sspd experiment k1.0,” University of Waterloo, Tech. Rep., 2007.

[67] Z. Yan, A. Majedi, and S. Safavi-Naeini, “Physical modeling of hot-electron superconducting single-photon detectors,” *IEEE Transactions on Applied Superconductivity*, vol. 17, no. 3, pp. 3789 – 94, 2007. [Online]. Available: http://dx.doi.org/10.1109/TASC.2007.906001

[68] W. Slysz, M. Wegrzecki, J. Bar, P. Grabiec, M. Gorska, C. Latta, V. Zwiller, A. Pearlman, A. Cross, A. Korneev, P. Kouminov, K. Smirnov, B. Voronov, G. Gol’tsman, A. Verevkin, M. Currie, and R. Sobolewski, “Fiber-coupled quantum-communications receiver based on two NbN superconducting single-photon detectors,” A. Rogalski, E. L. Dereniak, and F. F. Sizov, Eds., vol. 5957, no. 1. SPIE, 2005, p. 59571K. [Online]. Available: http://link.aip.org/link/?PSI/5957/59571K/1

[69] G. Gol’tsman, O. Okunev, G. Chulkova, A. Lipatov, A. Dzardanov, K. Smirnov, A. Semenov, B. Voronov, C. Williams, and R. Sobolewski, “Fabrication and properties of an ultrafast NbN hot-electron single-photon detector,” *IEEE Transactions on Applied Superconductivity*, vol. 11, no. 1, pp. 574–577, March 2001.

[70] V. Anant, A. J. Kerman, E. A. Dauler, J. K. W. Yang, K. M. Rosfjord, and K. K. Berggren, “Optical properties of superconducting nanowire single-photon detectors,” *Opt. Express*, vol. 16, no. 14, pp. 10750–10761, 2008. [Online]. Available: http://www.opticsexpress.org/abstract.cfm?URI=oe-16-14-10750

[71] J. Yang, A. Kerman, E. Dauler, V. Anant, K. Rosfjord, and K. Berggren, “Modeling the electrical and thermal response of superconducting nanowire single-photon detectors,” *IEEE Transactions on Applied Superconductivity*, vol. 17, no. 2, pp. 581 – 5, 2007. [Online]. Available: http://dx.doi.org/10.1109/TASC.2007.898660

[72] F. Marsili, D. Bitauld, A. Fiore, A. Gaggero, R. Leoni, F. Mattioli, A. Divochiy, A. Korneev, V. Seleznev, N. Kaurova, O. Minaeva, and G. Goltsman, “Superconducting parallel nanowire detector with photon number resolving functionality,” *Journal of Modern Optics*, vol. 56, no. 2, pp. 334–344, 2009. [Online]. Available: http://www.informaworld.com/10.1080/09500340802220729

[73] M. Ejrnaes, A. Casaburi, R. Cristiano, O. Quaranta, S. Marchetti, and S. Pagano, “Maximum count rate of large area superconducting single photon detectors,” *Journal of Modern Optics*, vol. 56, no. 2, pp. 390–394, 2009. [Online]. Available: http://www.informaworld.com/10.1080/09500340802673182

[74] M. Ejrnaes, A. Casaburi, O. Quaranta, S. Marchetti, A. Gaggero, F. Mattioli, R. Leoni, S. Pagano, and R. Cristiano, “Characterization of parallel superconducting nanowire single photon

detectors," *Superconductor Science and Technology*, vol. 22, no. 5, p. 055006 (7pp), 2009. [Online]. Available: http://stacks.iop.org/0953-2048/22/055006

[75] E. A. Dauler, A. J. Kerman, B. S. Robinson, J. K. W. Yang, B. Voronov, G. Goltsman, S. A. Hamilton, and K. K. Berggren, "Photon-number-resolution with sub-30-ps timing using multi-element superconducting nanowire single photon detectors," *Journal of Modern Optics*, vol. 56, no. 2, pp. 364–373, 2009. [Online]. Available: http://www.informaworld.com/10.1080/09500340802411989

[76] A. Semenov, A. Engel, K. Il'in, G. Gol'tsman, M. Siegel, and H.-W. Hubers, "Ultimate performance of a superconducting quantum detector," *European Physical Journal, Applied Physics*, vol. 21, no. 3, pp. 171 – 8, 2003. [Online]. Available: http://dx.doi.org/10.1051/epjap:2003009

[77] A. Semenov, P. Haas, B. Gunther, H.-W. Hubers, K. Il'in, and M. Siegel, "Energy resolution of a superconducting nanowire single-photon detector," *Journal of Low Temperature Physics*, vol. 151, no. 1, pp. 564–569, Apr. 2008. [Online]. Available: http://dx.doi.org/10.1007/s10909-007-9693-2

[78] A. Korneev, A. Divochiy, M. Tarkhov, O. Minaeva, V. Seleznev, N. Kaurova, B. Voronov, O. Okunev, G. Chulkova, I. Milostnaya, K. Smirnov, and G. Gol'tsman, "New advanced generation of superconducting NbN-nanowire single-photon detectors capable of photon number resolving," *Journal of Physics: Conference Series*, vol. 97, p. 012307 (6pp), 2008. [Online]. Available: http://stacks.iop.org/1742-6596/97/012307

[79] G. Goltsman, "Ultrafast nanowire superconducting single-photon detector with photon number resolving capability," vol. 7236, USA, 2009, pp. 72360D (11 pp.) –. [Online]. Available: http://dx.doi.org/10.1117/12.808313

[80] S. Dorenbos, E. Reiger, N. Akopian, U. Perinetti, V. Zwiller, T. Zijlstra, and T. Klapwijk, "Superconducting single photon detectors with minimized polarization dependence," *Applied Physics Letters*, vol. 93, no. 16, pp. 161102 (3 pp.) –, 2008. [Online]. Available: http://dx.doi.org/10.1063/1.3003579

[81] E. F. Driessen, F. Braakman, E. M. Reiger, V. Zwiller, and M. J. de Dood, "Polarization dependence of superconducting single photon detectors," in *Proc. and 2008 Conference on Quantum Electronics and Laser Science Lasers and Electro-Optics CLEO/QELS 2008. Conference on*, 4–9 May 2008, pp. 1–2.

[82] A. A. Verevkin, J. Zhang, W. Slysz, R. Sobolewski, A. P. Lipatov, O. Okunev, G. Chulkova, A. Korneev, and G. N. Gol'tsman, "Superconducting single-photon detectors for ghz-rate free-space quantum communications," J. C. Ricklin and D. G. Voelz, Eds., vol. 4821, no. 1. SPIE, 2002, pp. 447–454. [Online]. Available: http://link.aip.org/link/?PSI/4821/447/1

[83] B. S. Robinson, A. J. Kerman, E. A. Dauler, D. M. Boroson, S. A. Hamilton, J. K. W. Yang, V. Anant, and K. K. Berggren, "Demonstration of gigabit-per-second and higher data rates at extremely high efficiency using superconducting nanowire single photon detectors," A. K. Majumdar and C. C. Davis, Eds., vol. 6709, no. 1. SPIE, 2007, p. 67090Z. [Online]. Available: http://link.aip.org/link/?PSI/6709/67090Z/1

[84] P. Feautrier, E. le Coarer, R. E. de Lamaestre, P. Cavalier, L. Maingault, J.-C. Villegier, L. Frey, J. Claudon, N. Bergeard, M. Tarkhov, and J.-P. Poizat, "High-speed superconducting single photon detectors for innovative astronomical applications," *Journal of Physics: Conference Series*, vol. 97, p. 012087 (9pp), 2008. [Online]. Available: http://stacks.iop.org/1742-6596/97/012087